NASA Contractor Report 4139

Fully-Coupled Analysis of Jet Mixing Problems

Three-Dimensional PNS Model, SCIP3D

D. E. Wolf, N. Sinha,
and S. M. Dash

CONTRACT NAS1-16535
APRIL 1988

NASA

NASA Contractor Report 4139

Fully-Coupled Analysis of Jet Mixing Problems

Three-Dimensional PNS Model, SCIP3D

D. E. Wolf, N. Sinha,
and S. M. Dash
Science Applications International Corporation
Princeton, New Jersey

Prepared for
Langley Research Center
under Contract NAS1-16535

National Aeronautics
and Space Administration

**Scientific and Technical
Information Division**

1988

TABLE OF CONTENTS

NOMENCLATURE. viii
ABSTRACT. x

1. INTRODUCTION 1

1.1 Program Overview. 1
1.2 Utilization of SCIPVIS and SPLITP in Other Programs 1
1.3 3D Jet Mixing Code, SCIP3D. 3

2. GOVERNING EQUATIONS. 5

2.1 The 3D PNS Equations. 5
2.2 Thermodynamics. 5
2.3 Parabolized Stress and Transport Terms. 7
2.4 Two-Equation Turbulence Models. 9
2.5 Mapped Vectorized Equations 11

3. NUMERICAL PROCEDURES FOR ANALYZING SUPERSONIC MIXING PROBLEMS AND NUMERICAL STUDIES 16

3.1 Interior Point Algorithm. 16
3.2 Grid Distribution and Step-Size Control 17
3.3 Boundary Point Procedures 21
3.4 Corner Problem Test Cases 25
3.5 Square Converging-Diverging Nozzle Problem. 29
3.6 Balanced Pressure Square Jet Problem. 29
3.7 Underexpanded Square Jet Problem. 37
3.7.1 Rectangular Coordinate Solution. 37
3.7.2 Cylindrical Coordinate Solution. 49
3.8 Balanced Pressure 4/1 Aspect Ratio Rectangular Jet Problem 49
3.9 Underexpanded 4/1 Aspect Ratio Rectangular Jet Problem 59
3.10 Multiple Underexpanded Square Jet Problem 74

4. NUMERICAL PROCEDURES FOR ANALYZING SUBSONIC MIXING PROBLEMS AND NUMERICAL STUDIES 80

4.1 Overview of Pressure-Split PNS Subsonic Marching Approach 80
4.2 Parabolic Marching Procedure. 82
4.3 Cross-Flow Equations. 83
4.4 Cross-Flow Integration Procedure. 86
4.5 Pressure-Split PNS Subsonic Square Jet Calculation. 87
4.6 Pressure-Split PNS 4/1 Aspect Ratio 90
4.7 Parabolic Marching Approach (P = P(x) Only) 94
4.8 Parabolic Rectangular Jet Analysis in Adaptive Cylindrical Coordinates 100

4.9 Comparison of Parabolic and Supersonic PNS Predictions for 3/1 Aspect Ratio Rectangular Jet Using Hybrid Adaptive Grid. 100

5. NUMERICAL PROCEDURE FOR ANALYZING SUPERSONIC JETS EXHAUSTING INTO SUBSONIC EXTERNAL STREAMS AND NUMERICAL STUDIES 109

5.1 Review of 2D Numerics for Supersonic/Subsonic Jet Mixing Problem. 109
5.2 Nonadaptive Rectangular Matching Boundary Approach. 112
5.3 Variable Rectangular Grid Matching Boundary Approach. . . . 116
5.4 Fully Adaptive Matching Boundary Approach 116

6. SUMMARY. 130

7. REFERENCES 131

LIST OF FIGURES

1. Utilization of SCIPVIS and SPLITP Models for Zonal PNS Analysis of Rocket Plume Flowfields in JANNAF SPF/3 Standard Plume Flowfield Model 2

2. Coordinate System Nomenclature for Cartesian and Cylindrical Systems. 6

3. Mapped Computational Domain for Supersonic Rectangular Jet Exhausting into Supersonic Stream. 13

4. Hybrid Rectangular/Circular Mapping in Cross-Flow Plane for Generalized Rectangular Jet Problems 15

5. Initial Hybrid Grid for Analysis of Rectangular Jet Mixing Problem 18

6. Cylindrical/Cartesian Grid Coupling Using Overlap Cartesian Planes 20

7. Schematic of Wave-Correction Procedure Used to Couple Jet and Linearized Supersonic Flow Solution at Jet Boundary. 22

8. Pressure Contours for Double Compression Corner. 27

9. Streamwise Variation of Corner Pressure for Double Compression Case 28

10. Square Converging-Diverging Nozzle 30

11. Temperature Contours on Symmetry Plane for Square CD Nozzle Problem 31

12. Streamwise Variation of Mach Number Along the Axis for Square Nozzle Problem. 32

13. Streamwise Variation of Pressure Along the Axis for Square Nozzle Problem. 33

14. Streamwise Variation of Pressure Along Wall/Axis Juncture for Square Nozzle Problem 34

15. Streamwise Variation of Pressure Along the Corner for Square Nozzle Problem. 35

16. Jet Boundary Contours for Balanced Pressure Square Jet Problem, $k\varepsilon$ Turbulence Model Utilized. 36

17. ϕ Contours at $x/r_j = 80$ for Balanced Pressure Square Jet Problem, $k\varepsilon$ Turbulence Model Utilized. 38

LIST OF FIGURES - CONTINUED

18. Turbulent Kinetic Energy Contours at $x/r_j = 20$ for Balanced Pressure Square Jet Problem, $k\varepsilon$ Turbulence Model Utilized 39

19. Variation of Turbulent Kinetic Energy (XK) and Species Parameter (PHI) Along Axis of Symmetry for Square (SCIP3D) and Circular (SCIPVIS) Jets - kW Turbulent Model Utilized. . . . 40

20. Comparison of $k\varepsilon$ and kW Turbulence Model Results for Species Centerline Decay for Square Jet Problem. 41

21. Predicted Species (PHI) and Temperature (T) Contours in Plane of Symmetry for Square Jet Problem - $k\varepsilon$ Model Results. 42

22. Pressure Contours in y,z = 0 Symmetry Planes for Underexpanded Square Jet Problem, Rectangular Coordinate Solution 43

23. Cross-Flow Pressure Contours for Square Underexpanded Jet Problem, Rectangular Coordinate Solution 45

24. Cross-Flow ϕ Contours for Square Underexpanded Jet Problem, Rectangular Coordinate Solution 46

25. Outer Jet Contours (ϕ = .1) for Underexpanded Square Jet Calculation. 47

26. Comparison of SCIP3D Predicted Centerline Pressure Variation for Underexpanded Square Jet Problem with SCIPVIS Predictions for Analogous Planar (2D) and Axisymmetric Jet Problems. 48

27. Adaptive Cylindrical Grid; Grid Distribution at x = 0 and 10 for Underexpanded Square Jet Problem 50

28. Pressure Contours in Symmetry Planes for Underexpanded Square Jet Problem, Cylindrical Solution 51

29. Comparison of Centerline Pressure Variation and Jet Outer Boundary Variations for Cartesian Grid and Cylindrical Grid Solutions 52

30. Comparison of Cartesian Grid and Cylindrical Grid ϕ Contours at $x/r_j = 10$. 53

31A. Cross-Flow Velocity Vectors at $x/r_j = 2$. 54

31B. Cross-Flow Velocity Vectors at $x/r_j = 4$. 55

31C. Cross-Flow Velocity Vectors at $x/r_j = 6$. 56

LIST OF FIGURES - CONTINUED

31D. Cross-Flow Velocity Vectors at $x/r_j = 8$. 57

31E. Cross-Flow Velocity Vectors at $x/r_j = 10$ 58

32. U Contours for 4/1 Balanced Pressure Mixing Problem in Symmetry Planes. 60

33. ϕ Contours for 4/1 Balanced Pressure Mixing Problem in Symmetry Planes. 61

34. T Contours for 4/1 Balanced Pressure Mixing Problem in Symmetry Planes. 62

35. K Contours for 4/1 Balanced Pressure Mixing Problem in Symmetry Planes. 63

36. Cross-Flow Contours of ϕ for 4/1 Balanced Pressure Rectangular Jet Case 64

37. Cross-Flow Contours of K for 4/1 Balanced Pressure Rectangular Jet Case 65

38. Overall Jet Structure in Symmetry Planes as Exhibited by ϕ Contours for 4/1 Balanced Pressure Case. 66

39. ϕ Contours in Cross-Flow Plane at x=60, 80 and 100 for 4/1 Balanced Pressure Case 67

40. Centerline Variation of ϕ; 4/1 Balanced Pressure Case. 68

41. Centerline Variation of T; 4/1 Balanced Pressure Case. 69

42. Centerline Variation of K; 4/1 Balanced Pressure Case. 70

43. Pressure Contours in Symmetry Planes for 4/1 Underexpanded Case. 71

44. Jet Cross-Flow Contours for Rectangular Underexpanded Jet ($P_J/P_E = 2$). 72

45. Pressure Variation Along Jet Axis; Underexpanded Rectangular Jet. 73

46. Schematic of Multiple Square Jet Problem and Shock/Shear Layer Pattern in z = 0 Symmetry Plane. 75

47. ϕ and P Contours in z = 0 Symmetry Plane for Multiple Square Jet Problem 76

48. ϕ Cross-Flow Contours for Multiple Square Jet Problem. 77

LIST OF FIGURES - CONTINUED

49. Axial Velocity and Turbulent Kinetic Energy Profiles for Multiple Jet Problem 79

50. V and W Grids and Diagonal Coupling Nomenclature for Subsonic Cross-Flow Solution 88

51. Square Subsonic Jet Calculations; Cross-Flow Contours at x = 20 89

52. Square Jet Calculation; Streamwise Vorticies Generated By Corner Region at x = 20 91

53. Subsonic Square Jet Calculation; ϕ = 0.1 Contours Superimposed on Cross-Flow Vectors Map at x = 40-100 92

54. Subsonic Square Jet Predictions for ϕ and k Variations Along Axis. 93

55. Rectangular Subsonic Jet Calc., Contours at x = 20 95

56. Rectangular Subsonic Jet Calculation, Contours at x = 40, 60, 80 and 100 96

57. Rectangular Jet, ϕ Contours on y, x = 0 Symmetry Planes. 97

58. Subsonic Rectangular Jet, ϕ and k Profiles at x = 100, 200 and 300. 98

59. Subsonic Rectangular Jets, U and k-axis Variations 99

60. ϕ Contours for 2/1 Rectangular Jet, Parabolic Run Option 101

61. T Contours for 2/1 Rectangular Jet, Parabolic Run Option 102

62. ϕ Cross-Flow Contours for 2/1 Rectangular Jet Problem. 103

63. T Cross-Flow Contours for 2/1 Rectangular Jet Problem. 104

64. ϕ and T Cross-Flow Contours at x = 50 for 2/1 Rectangular Jet Problem. 105

65. ϕ Cross-Flow Contours for 3/1 Rectangular Jet Problem, Supersonic PNS vs. Parabolic Solutions 106

66. Cross-Flow Velocity Vector Field at x = 20 for 3/1 Rectangular Jet Problem, Parabolic Run Option. 107

67. Evolution of Jet Boundary Contours from Rectangular to Circular for 3/1 Rectangular Jet Problem 108

LIST OF FIGURES - CONTINUED

68. SCIPVIS Prediction of Mach 2 Jet Into Still Air and Comparisons with Data of Seiner (from Ref. 1). 110

69. 2D Supersonic/Subsonic Coupling at Jet Sonic Line. 111

70. Rectangular Matching Boundary for Mixed Supersonic/Subsonic Problem. 113

71. Species (ϕ) Contours and Cross-Flow Velocity Vectors for Underexpanded Square Jet into Subsonic External Stream Using Version I Supersonic/Subsonic Coupling (Embedded Rectangle). . . 114

72. Variable Rectangular Grid Matching Boundary. 117

73. Species (ϕ) Contours and Cross-Flow Velocity Vectors for Underexpanded Square Jet into Subsonic External Stream Using Version II Supersonic/Subsonic Coupling (Variable Grid Point) 118

74. ϕ Contours in Symmetry Plane for Balanced Pressure Subsonic/Supersonic Square Jet Problem 119

75. T Contours in Symmetry Plane for Balanced Pressure Subsonic/Supersonic Square Jet Problem 120

76. ϕ Contours at x = 25 for Balanced Pressure Subsonic/ Supersonic Square Jet Problem. 121

77. T Contours at x = 25 for Balanced Pressure Subsonic/ Supersonic Square Jet Problem. 122

78. Adaptive Cylindrical Grid in Cross-Flow Plane at x = 25 for Balanced Pressure Square Jet Problem 123

79. Perturbation Pressure Contours in Cross-Flow Plane at x = 25 for Balanced Pressure, Square Jet Problem 124

80. Contours of ϕ and P for Underexpanded Subsonic/Supersonic Square Jet Problem 126

81. Pressure Variation Along Jet Axis for Underexpanded Subsonic/ Supersonic Square Jet Problem. 127

82. Comparison of SCIP3D and SCIPVIS Predictions of Shear Layer Boundaries for Underexpanded Axisymmetric Subsonic/ Supersonic Jet Problem 128

83. Comparison of SCIP3D and SCIPVIS Predictions of Jet Center-line Pressure Variations for Underexpanded Axisymmetric Subsonic/Supersonic Jet Problem. 129

NOMENCLATURE

a, b	mapping parameters
C_p	specific heat
C_μ, C_D, C_1, C_2, C_3	turbulence model coefficients
e_y, e_z	convective terms alternating difference parameters
$\bar{E}$, $\bar{F}$, $\bar{G}$, $\bar{H}$	conservation variable vector arrays
h	static enthalpy
H	total enthalpy ($= h + \frac{1}{2} Q^2$)
J	planar ($J=0$)/axisymmetric ($J=1$) flag
k, ε, W	turbulence model variables
M	Mach number
P	static pressure
$\underline{P}$	production rate of turbulent kinetic energy
Pr	Prandtl number
Q	total velocity
R_o	universal gas constant
T	static enthalpy
U, V, W	velocity components
$\tilde{V}$, $\tilde{W}$	mapped velocities in η and ζ directions
$\bar{V}_f$	stress/transport terms
$W(\phi)$	mixture molecular weight
x, y, z	cartesian coordinates
x, ϕ, r	cylindrical coordinates
α	subsonic ($\alpha=0$)/supersonic ($\alpha=1$) parameter
α_i	mass fraction of ith species
β	flux parameter ($\beta = \rho U^2$)
ξ, η, ζ	mapped coordinates

NOMENCLATURE - CONTINUED

γ	specific heat ratio
$\tilde{\gamma}$	specific heat ratio parameter (= $[\gamma-1]/\gamma$)
ρ	gas mixture density
σ_f	effective Prandtl number
$\tilde{\phi}$	species mass fraction parameter
μ	effective viscosity (= $\mu_l + \mu_t$)
$\tilde{\mu}$	effective transport parameter for scalar diffusion
ω	vorticity

ABSTRACT

This final technical report describes numerical procedures formulated for the analysis of three-dimensional (3D) jet mixing problems, as incorporated in the computer model, SCIP3D. The overall methodology closely parallels that developed in the earlier 2D/axisymmetric jet mixing model, SCIPVIS. SCIP3D integrates the 3D parabolized Navier-Stokes (PNS) jet mixing equations, cast in mapped cartesian or cylindrical coordinates, employing the explicit MacCormack Algorithm. A pressure-split variant of this algorithm is employed in subsonic regions with a sublayer approximation utilized for treating the streamwise pressure component. SCIP3D contains both the $k\varepsilon$ and $k\omega$ turbulence models, and employs a two-component mixture approach to treat jet exhausts of arbitrary composition. Specialized grid procedures are used to adjust the grid growth in accordance with the growth of the jet, including a hybrid cartesian/cylindrical grid procedure for rectangular jets which moves the hybrid coordinate origin towards the flow origin as the jet transitions from a rectangular to circular shape. Numerous calculations are presented for rectangular mixing problems, as well as for a variety of basic unit problems exhibiting overall capabilities of SCIP3D.

1. INTRODUCTION

1.1 Program Overview

This final technical report describes computational methodology developed to analyze 3D jet mixing problems using spatial matching parabolized Navier-Stokes (PNS) methodology. The program was initiated in 1981 with preliminary work focused on developing methodology for analyzing 2D supersonic free jet interaction problems. The SCIPVIS shock-capturing model, initially developed to analyze such supersonic problems, was then extended to analyze supersonic jets exhausting into subsonic external streams. The SCIPVIS methodology was documented in an interim technical report,[1] and a number of journal articles were published which describe its application to analyzing the detailed multiple-cell shock structure in turbulent jets (see refs. 2-5).

The SCIPVIS model employed explicit numerics and thus could not readily analyze wall-bounded jet flows which resolve the details of the near-wall boundary layer. To address this problem area, the 2D SPLITP model was developed which employs implicit, pressure-split numerics. A number of earlier papers and journal articles describe various aspects of the numerics in SPLITP (see refs. 6-9). The extension of SCIPVIS and SPLITP based numerics to analyze 3D jet mixing problems is the subject of this final technical report.

1.2 Utilization Of SCIPVIS and SPLITP Models In Other Programs

The SCIPVIS and SPLITP 2D research models developed under this NASA program have been extended to analyze a broad spectrum of problem areas under other government sponsored programs. Under Army (MICOM) and Air Force (AFWAL) support, SCIPVIS and SPLITP have been extended to analyze multi-component/multi-phase flows with nonequilibrium chemistry and gas/particle interactions. They serve as components of the latest JANNAF Standard Plume Flowfield Model (SPF/3) as schematized in Figure 1, and described in refs. 10 and 11, and in several papers presented at the JANNAF 15th and 16th Plume Technology Meetings. Analogous pairing of SCIPVIS and SPLITP PNS numerics has been utilized to analyze hypersonic wake flowfields

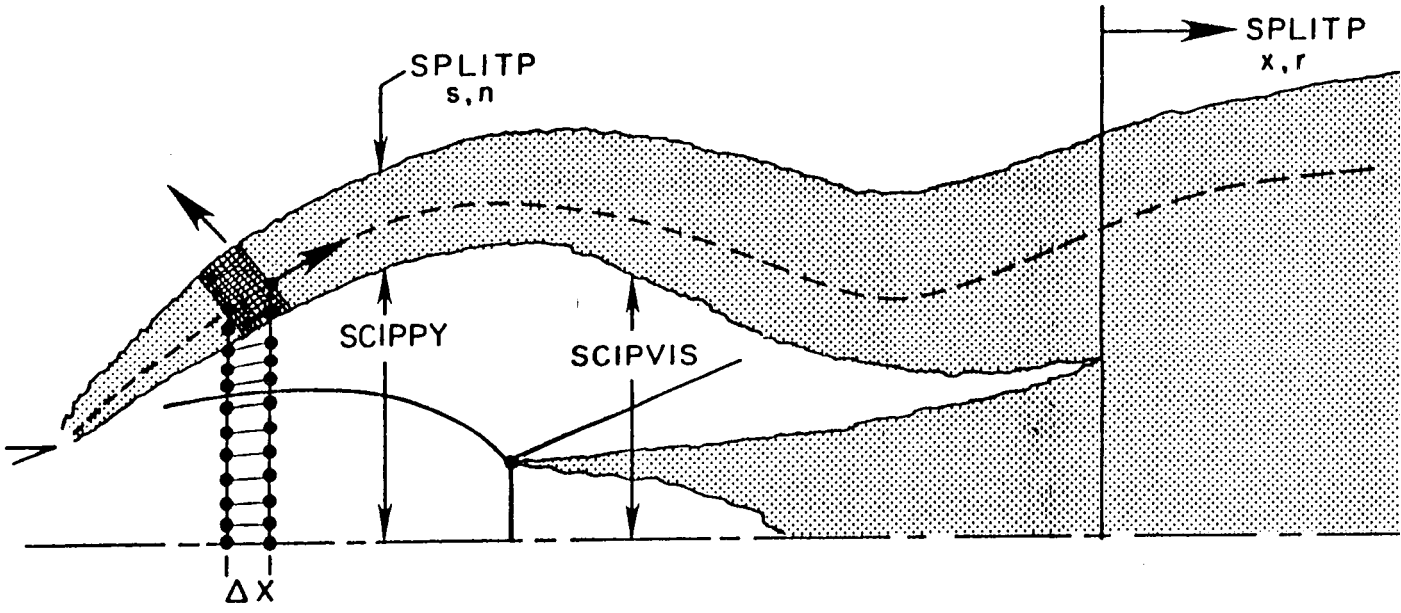

FIGURE 1. Utilization Of SCIPVIS and SPLITP Models For Zonal PNS Analysis Of Rocket Plume Flowfields In JANNAF SPF/3 Standard Plume Flowfield Model.

as described in refs. 11-13. In both the plume and wake models above, SCIPVIS and SPLITP are also utilized to analyze the base region employing Chapman-Korst type assumptions to achieve closure (see refs. 10 and 14 for details). A wall jet version of SPLITP is a major component of the circulation-control airfoil code[15-17] developed jointly by SAIC and AMI under NASA/Ames support.

The most recent extensions of SPLITP and SCIPVIS numerics were made under DARPA/Air Force Support to analyze scramjet propulsive flowfields in support of the National AeroSpace Plane (NASP) program. The NASP version of SPLITP, entitled SCORCH, is utilized to analyze scramjet supersonic combustor flowfields with tangential or moderately inclined fuel injection (refs. 18 and 19). The NASP version of SCIPVIS, entitled SCHNOZ, is utilized to analyze scramjet nozzle flowfields including the plume-like interaction of the nozzle exhaust flow with the vehicle aerodynamic flow at supersonic flight conditions (refs. 20 and 21). These codes have enhanced numerical capabilities to deal with strongly combusting flows in comparison with the earlier plume/wake versions. SCORCH and SCHNOZ comprise components of a complete design-oriented scramjet propulsive flowfield model[22,23] which has seen widespread usage by the NASP community. Current efforts are focused on unifying SCORCH/SCHNOZ numerics for the multi-zone analysis of generalized 2D jet mixing problems with chemistry, utilizing SCORCH implicit numerics in near-wall regions, and SCHNOZ explicit numerics in central regions.

1.3 3D Jet Mixing Code, SCIP3D

The SCIP3D code represents extensions of the 2D methodology in the SCIPVIS and SPLITP models to analyze 3D jet mixing problems. SCIP3D is based upon the numerics in the SCIPVIS code and employs the explicit MacCormack algorithm to spatially integrate the 3D PNS jet mixing equations in supersonic flow regions utilizing mapped rectangular or cylindrical coordinates. Both the $k\varepsilon$ and kW two-equation turbulence models are incorporated into SCIP3D. For subsonic jet mixing problems, a pressure-split approach is employed whereby the streamwise pressure gradient is imposed and the cross-flow velocity field is determined via a coupled noniterative approach which parallels that employed in SPLITP for highly

curved jets.[8] For mixed problems (supersonic jet into subsonic stream), it has been found necessary to adapt the grid to the shape of jet sonic line to deal with supersonic/subsonic coupling methodology in an 'organized' manner. For rectangular jets with large aspect ratios, this has required the utilization of hybrid rectangular/cylindrical mapped grids with a moving cylindrical origin which ultimately coincides with the jet axis far downstream when the jet takes on a circular shape. Numerous test cases are described in this report which were performed to check-out the varied run options included in SCIP3D. Various aspects of SCIP3D methodology have been given in earlier papers and journal articles (see refs. 24-27). This report will attempt to synthesize the work already documented, expand upon it where necessary, and provide details of recent work not yet reported upon.

2. GOVERNING EQUATIONS

2.1 The 3D PNS Equations

The conservative form of the 3D PNS 'straight-back' jet mixing equations in cartesian (J=0) or cylindrical (J=1) coordinates is listed below:

$$\frac{\partial \bar{E}}{\partial x_1} + \frac{1}{r^J}\frac{\partial \bar{F}}{\partial x_2} + \frac{\partial \bar{G}}{\partial x_3} + \bar{H} = \bar{V}_F \qquad (1)$$

In eq. (1), x_1 corresponds to the axial (marching) direction, x_2 is the cross-flow direction, and x_3 is the vertical or radial direction. The coordinate system nomenclature for the two systems is summarized in Figure 2. The vector arrays comprising $\bar{E}$, $\bar{F}$, $\bar{G}$ and $\bar{H}$ are as follows:

$$\bar{E} = \begin{bmatrix} \rho U \\ \alpha P + \rho U^2 \\ \rho UV \\ \rho UW \\ \rho UH \\ \rho U\tilde{\phi} \end{bmatrix} \qquad \bar{F} = \begin{bmatrix} \rho V \\ \rho UV \\ P + \rho V^2 \\ \rho VW \\ \rho VH \\ \rho V\tilde{\phi} \end{bmatrix} \qquad \bar{G} = \begin{bmatrix} \rho W \\ \rho UW \\ \rho VW \\ P + \rho W^2 \\ \rho WH \\ \rho W\tilde{\phi} \end{bmatrix}$$

$$\bar{H} = \frac{1}{r^J}\begin{bmatrix} J\rho W \\ r^J(1-\alpha)\partial P/\partial x_1 + J\rho UW \\ 2J\rho VW \\ J(W^2 - V^2) \\ J\rho WH \\ J\rho W\tilde{\phi} \end{bmatrix} \qquad \bar{V}_F = \begin{bmatrix} 0 \\ V_U \\ V_V \\ V_W \\ V_H \\ V_{\tilde{\phi}} \end{bmatrix}$$

The vector $\bar{V}_F$, represents the parabolized stress and transport terms. In the above equations, U, V, and W are the axial, crossflow and radial velocity components, ρ is the density, P is the pressure, H is the total enthalpy, and $\tilde{\phi}$ is the species parameter to be described below. The parameter, α, is a pressure-split parameter used to distinguish between supersonic (α=1) and subsonic (α=0) run modes.

2.2 Thermodynamics

The jet mixing problems considered assume that the jet and external streams are each of uniform composition. For nonreacting (chemically frozen) situations, the species parameter, $\tilde{\phi}$, describes the local mixture

CARTESIAN SYSTEM (J=0)

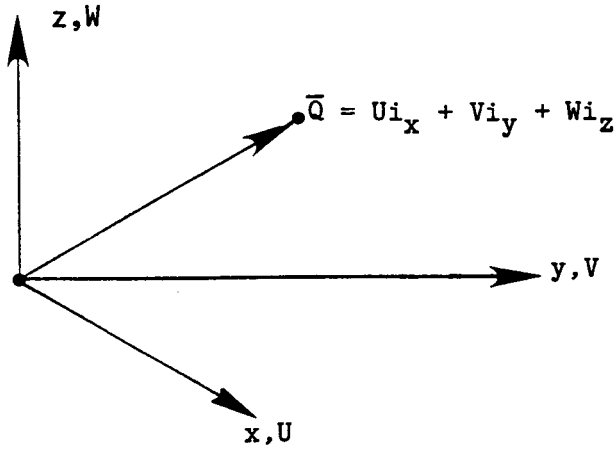

CYLINDRICAL SYSTEM (J=1)

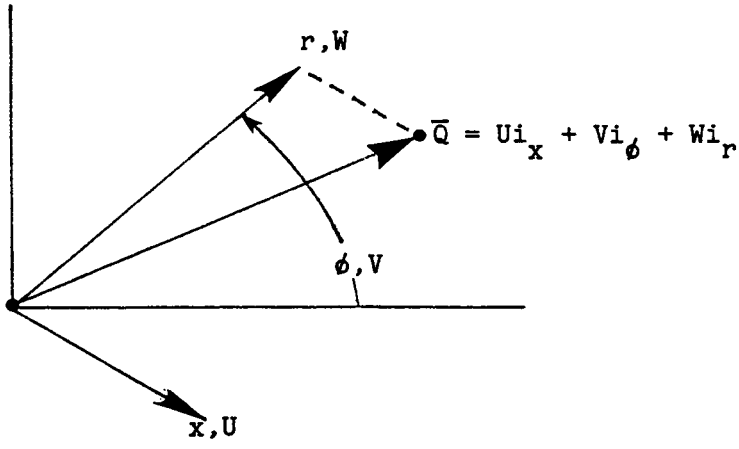

System	x_1	x_2	x_3
Cartesian	x	y	z
Cylindrical	x	ϕ	r

FIGURE 2. Coordinate System Nomenclature For Cartesian and Cylindrical Systems.

composition; viz.,

$$\tilde{\phi} = \frac{\alpha_i - \alpha_{i_E}}{\alpha_{i_J} - \alpha_{i_E}} \tag{2}$$

where α_i is the mass fraction of the ith species and J and E represent the constant values of α_i in the unmixed jet and external streams. The static enthalpy is given by:

$$h(\tilde{\phi},T) = \{h_J(T) - h_E(T)\}\tilde{\phi} + h_E(T) \tag{3}$$

where:

$$h_{J,E} = \sum_i \{\alpha_i h_i(T)\}_{J,E}$$

Then the specific heat ratio, $\gamma(\tilde{\phi},T)$ is given by:

$$\gamma(\tilde{\phi},T) = \frac{C_p(\phi,T)W(\phi)/R_o}{C_p(\phi,T)W(\phi)/R_o - 1} \tag{4}$$

where the specific heat, C_p, is given by:

$$C_p(\tilde{\phi},T) = \frac{\partial h}{\partial T} \tag{5}$$

and the molecular weight, W, is given by:

$$W(\phi) = \left[\left(\frac{1}{W_J} - \frac{1}{W_E} \right) \tilde{\phi} + \frac{1}{W_E} \right]^{-1} \tag{6}$$

2.3 Parabolized Stress and Transport Terms

Eliminating all terms containing streamwise derivatives and using the Boussinesq-type approximation, the parabolized stress terms in the cartesian and cylindrical systems are written as follows:

Cartesian Coordinates ($x_1 = x$, $x_2 = y$, $x_3 = z$)

$$V_U = \frac{\partial}{\partial y}\left(\mu \frac{\partial U}{\partial y}\right) + \frac{\partial}{\partial z}\left(\mu \frac{\partial U}{\partial z}\right) \tag{7a}$$

$$V_V = \frac{\partial}{\partial y}\left(\frac{4}{3}\mu \frac{\partial V}{\partial y}\right) + \frac{\partial}{\partial z}\left(\mu \frac{\partial V}{\partial z}\right) - \frac{\partial}{\partial y}\left(\frac{2}{3}\mu \frac{\partial W}{\partial z}\right) + \frac{\partial}{\partial z}\left(\mu \frac{\partial W}{\partial y}\right) \tag{7b}$$

$$V_W = \frac{\partial}{\partial z}\left(\frac{4}{3}\mu \frac{\partial W}{\partial z}\right) + \frac{\partial}{\partial y}\left(\mu \frac{\partial W}{\partial y}\right) - \frac{\partial}{\partial z}\left(\frac{2}{3}\mu \frac{\partial V}{\partial y}\right) + \frac{\partial}{\partial y}\left(\mu \frac{\partial V}{\partial z}\right) \tag{7c}$$

$$V_H = \frac{\partial}{\partial y}\left(\tilde{\mu} \frac{\partial H}{\partial y}\right) + \frac{\partial}{\partial z}\left(\tilde{\mu} \frac{\partial H}{\partial z}\right) \tag{7d}$$

$$V_\phi = \frac{\partial}{\partial y}\left(\tilde{\mu} \frac{\partial \tilde{\phi}}{\partial y}\right) + \frac{\partial}{\partial z}\left(\tilde{\mu} \frac{\partial \tilde{\phi}}{\partial z}\right) \tag{7e}$$

Cylindrical Coordinates ($x_1 = x$, $x_2 = \phi$, $x_3 = r$)

$$V_U = \frac{1}{r}\frac{\partial}{\partial \phi}\left(\mu \frac{1}{r}\frac{\partial U}{\partial \phi}\right) + \frac{\partial}{\partial r}\left(\mu \frac{\partial U}{\partial r}\right) \tag{8a}$$

$$V_V = \frac{1}{r^2}\frac{\partial}{\partial r}\left[r^2\mu\left(\frac{\partial V}{\partial r} + \frac{1}{r}\frac{\partial W}{\partial \phi} - \frac{V}{r}\right)\right] + \frac{1}{r}\frac{\partial}{\partial \phi}\left[\mu\left(\frac{4}{3}\frac{1}{r}\frac{\partial V}{\partial \phi} - \frac{2}{3}\frac{1}{r}\frac{\partial}{\partial r}[rW]\right) + 2\mu\frac{W}{r}\right] \tag{8b}$$

$$V_W = \frac{1}{r}\frac{\partial}{\partial r}\left[\frac{4}{3}\mu\frac{\partial}{\partial r}(rW) - \frac{2}{3}\mu\frac{\partial V}{\partial \phi} - 2\mu W\right] + \frac{1}{r}\frac{\partial}{\partial \phi}\left[\mu\left(\frac{\partial V}{\partial r} + \frac{1}{r}\frac{\partial W}{\partial \phi}\right) - \mu\frac{V}{r}\right] - \frac{1}{r}\mu\left[\frac{4}{3}\frac{1}{r}\frac{\partial V}{\partial \phi} - \frac{2}{3}\frac{1}{r}\frac{\partial}{\partial r}(rW) + 2W/r\right] \tag{8c}$$

$$V_H = \frac{1}{r} \frac{\partial}{\partial \phi} \left(\tilde{\mu} \frac{1}{r} \frac{\partial H}{\partial \phi}\right) + \frac{\partial}{\partial r} \left(\tilde{\mu} \frac{\partial H}{\partial r}\right) \tag{8d}$$

$$V_{\phi} = \frac{1}{r} \frac{\partial}{\partial \phi} \left(\tilde{\mu} \frac{1}{r} \frac{\partial \tilde{\phi}}{\partial \phi}\right) + \frac{\partial}{\partial r} \left(\tilde{\mu} \frac{\partial \tilde{\phi}}{\partial r}\right) \tag{8e}$$

In the above stress/transport term expressions, μ represents the 'effective viscosity' ($= \mu_l + \mu_t$) and $\tilde{\mu}$ is the effective transport parameter for scalar diffusion ($= \mu_l/Pr + \mu_t/Pr_t$) based on the assumption that heat and mass diffuse at the same rate (viz., Lewis number of unity assumed).

2.4 Two-Equation Turbulence Models

Both the kε[28] and kW[29] two-equation turbulence models are utilized in SCIP3D. The standard coefficients and constants are employed as described in the earlier SCIPVIS report.[1] Using tensor notation (repeated subscripts indicating summation), the kε model solves the following equations for k and ε:

$$\frac{\partial}{\partial x_j} (\rho V_j k) = \frac{\partial}{\partial x_j} \left(\frac{\mu_t}{\sigma_k} \frac{\partial k}{\partial x_j} \right) + \underline{P} - \varepsilon \tag{9a}$$

$$\frac{\partial}{\partial x_j} (\rho V_j \varepsilon) = \frac{\partial}{\partial x_j} \left(\frac{\mu_t}{\sigma_\varepsilon} \frac{\partial \varepsilon}{\partial x_j} \right) + C_1 \frac{\varepsilon}{k} \underline{P} - C_2 \rho \varepsilon^2/k \tag{9b}$$

where:

$$\underline{P} = \mu_t \left(\frac{\partial U_j}{\partial x_i} + \frac{\partial U_i}{\partial x_j} \right) \frac{\partial U_i}{\partial x_j} = \mu_t \omega \tag{10}$$

The dominant cartesian parabolized terms in the vorticity, ω, for flows where U >> V, W are given by:

$$\omega = \mu_t \left(\frac{\partial U}{\partial y}\right)^2 + \left(\frac{\partial U}{\partial z}\right)^2 + 0 \left\{ \left[\frac{\partial [V,W]}{\partial [y,z]} \right] \right\}^2 \tag{11}$$

The dominant cylindrical parabolized terms in the vorticity, ω, are given by:

$$\omega = \mu_t \left[\left(\frac{1}{2} \frac{\partial U}{\partial \phi} \right)^2 \right] + \left(\frac{\partial U}{\partial r} \right)^2 + 0 \left\{ \left[\frac{\partial [V,W]}{\partial [\phi,r]} \right]^2 \right\}$$

The turbulent viscosity, μ_t, is defined by:

$$\mu_t = C_\mu \rho k^2 / \varepsilon \tag{12}$$

The kW model solves the following equations for k and W:

$$\frac{\partial}{\partial x_j} (\rho V_j k) = \frac{\partial}{\partial x_j} \left(\frac{\mu_t}{\sigma_k} \frac{\partial k}{\partial x_j} \right) + \underline{P} - \rho C_D k W^{1/2} \tag{13a}$$

$$\frac{\partial}{\partial x_j} (\rho V_j W) = \frac{\partial}{\partial x_j} \left(\frac{\mu_t}{\sigma_W} \frac{\partial W}{\partial x_j} \right) + \frac{C_1 W \underline{P}}{k} - C_2 \rho W^{3/2} + C_3 \mu_t (\nabla \omega)^2 \tag{13b}$$

The dominant cartesian parabolized terms in the vorticity expression, $(\nabla\omega)^2$, are enumerated below:

$$(\nabla\omega)^2 = \frac{1}{\omega^2} \left[\left(\frac{\partial U}{\partial y} \frac{\partial^2 U}{\partial y^2} \right)^2 + 2 \frac{\partial U}{\partial y} \frac{\partial U}{\partial z} \frac{\partial^2 U}{\partial y^2} \frac{\partial^2 U}{\partial y \partial z} + \left(\frac{\partial U}{\partial z} \frac{\partial^2 U}{\partial y \partial z} \right)^2 + \left(\frac{\partial U}{\partial y} \frac{\partial^2 U}{\partial z \partial y} \right)^2 + 2 \frac{\partial U}{\partial y} \frac{\partial U}{\partial z} \frac{\partial^2 U}{\partial z^2} \frac{\partial^2 U}{\partial z \partial y} + \left(\frac{\partial U}{\partial z} \frac{\partial^2 U}{\partial z^2} \right)^2 \right] \tag{14}$$

The dominant cylindrical parabolized terms in the vorticity expression, $(\nabla\omega)^2$, are given by:

$$(\nabla\omega)^2 = \frac{\omega^2}{r^2} + \frac{2}{r}\left[\left(\frac{\partial U}{\partial r}\right)\frac{\partial^2 U}{\partial r^2} + \left(\frac{1}{r}\frac{\partial U}{\partial \phi}\right)\frac{\partial}{\partial r}\left(\frac{1}{r}\frac{\partial U}{\partial \phi}\right)\right] \tag{15}$$

$$+ \frac{1}{\omega^2}\left[\left(\frac{\partial U}{\partial r}\right)\frac{\partial^2 U}{\partial r^2} + \frac{1}{r}\frac{\partial U}{\partial \phi}\frac{\partial}{\partial r}\left(\frac{1}{r}\frac{\partial U}{\partial \phi}\right)\right]^2$$

$$+ \frac{1}{\omega^2}\left[\frac{\partial U}{\partial r}\frac{1}{r}\frac{\partial}{\partial \phi}\left(\frac{\partial U}{\partial r}\right) + \frac{1}{r}\frac{\partial U}{\partial \phi}\frac{1}{r}\frac{\partial}{\partial \phi}\left(\frac{1}{r}\frac{\partial U}{\partial \phi}\right)\right]^2$$

The turbulent viscosity, μ_t, is defined by:

$$\mu_t = \rho k/W^{1/2} \tag{16}$$

2.5 Mapped Vectorized Equations

The mean flow and turbulence model equations are solved in a mapped computational domain defined by the geometric transformation:

$$\xi = x_1 \tag{17}$$
$$\eta = x_2/x_{2,U}$$
$$\zeta = (x_3 - x_{3,L})/(x_{3,U} - x_{3,L})$$

In this transformation, L and U designate bounding surfaces of the computation. In the present application of this mapping for rectangular problems, the bounding computational surfaces are assumed to have no cross curvature i.e. $y_U = y_U(x)$, $Z_{L,U} = Z_{L,U}(x)$. With this assumption, the cartesian equations can be cast in the following form:

$$\frac{\partial E}{\partial \xi} + \frac{\partial F}{\partial \eta} + \frac{\partial G}{\partial \zeta} + H = V_F \tag{18}$$

where:

$$E = \bar{E}$$

$$F = b_y\bar{F} - a_y\bar{E}$$

$$G = b_z\bar{G} - a_z\bar{E}$$

$$H = \bar{H} + ([a_y]_\eta + [a_z]_\zeta)\bar{E}$$

and the transformation parameters a_y, a_z, b_y and b_z are defined by:

$$a_y = \eta(y_U)_x/y_U$$

$$a_z = [(1-\zeta)[z_L]_x + \zeta[z_U]_x]/(z_U - z_L)$$

$$b_y = 1/y_U$$

$$b_z = 1/(z_U - z_L)$$

For free jet problems, y_U and $z_{L,U}$ must fully encompass the viscous jet. This is accomplished using growth rule formulations of the form:

$$\frac{dz_U}{dx} = \frac{(JMAX-1)}{(J^*-1)}\left(\frac{W}{U}\right)_{J^*} + \frac{z_U}{f_1}\left(\frac{\partial f}{\partial z}\right)_{JMAX} \qquad (19)$$

which parallel those utilized in SCIPVIS[1] for 2D underexpanded jets, applied on the two symmetry planes (y=0 and Z=0) as exhibited in Figure 3. In Figure 3, J* corresponds to the viscous dividing streamline position on the symmetry plane, y = 0, ascertained by monitoring the ϕ profile at each step ($\phi = \phi^*$, where $\phi^* = .5$ until the mixing reaches the axis); JMAX is the index of the upper boundary point; W/U is the streamline inclination at J*; and, $\partial f/\partial z$ is the outer edge gradient of the parameter f (taken to be the maximum of the streamwise velocity and species parameter). This boundary growth formulation provides for <u>exact</u> alignment of the viscous dividing streamline position with the mapped coordinate line, ζ = constant in the initial expansion region of the jet. Note that the viscous part of the growth relation (the $\partial f/\partial z$ term) is not activated until the jet shear layer reaches the upper boundary, and, that boundary growth is enforced to always be positive. Application of this boundary growth formulation on both symmetry

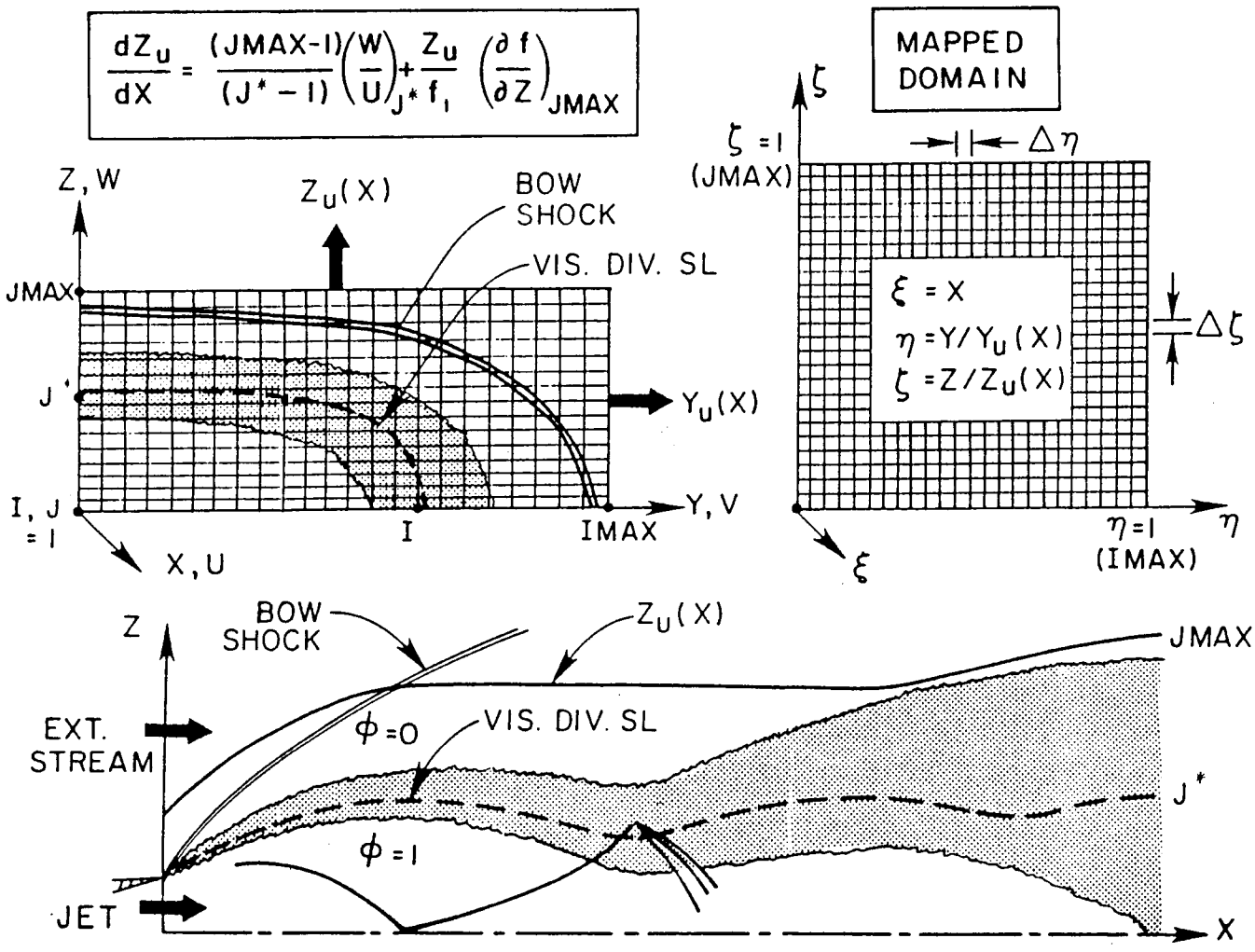

FIGURE 3. Mapped Computational Domain for Supersonic Rectangular Jet Exhausting Into Supersonic Stream.

planes to yield the variation of $z_U(x)$ and $y_U(x)$ yields a mapped grid network which initially captures the 3D jet induced bow shock, and encloses the viscous jet in a manner which automatically makes the transition from a rectangular to a square type of grid in accordance with the respective vertical and transverse gradients in the flow.

For cylindrical problems, the cross-flow boundaries are always constant (i.e. $x_{2,U} = \phi_U$ = constant) while the radial boundaries can have both axial and cross-curvature (i.e. $x_{3,L,U} = r_{L,U} = r_{L,U}(x,\phi)$. With these stipulations, the cylindrical equations can be cast in the same form as eq. (20) where now:

$$E = \bar{E} \tag{20}$$

$$F = b_\phi \bar{F}$$

$$G = r b_r \bar{G} - a_{r,\phi} \bar{F}$$

$$H = \bar{H} + (a_{r,\phi})\zeta\bar{F} - \bar{G} - (a_{r,x})\bar{E}/(b_r r) - a_{r,x} r(\bar{E}/r)\zeta$$

and the transformation parameters $a_{r,\phi}$, $a_{r,x}$, b_ϕ and b_r are defined by:

$$a_{r,\phi} = [(1-\zeta)r_{L_\phi} + \zeta r_{U_\phi}]/(r_U - r_L)$$

$$a_{r,x} = [(1-\zeta)r_{L_x} + \zeta r_{U_x}]/(r_U - r_L)$$

$$b_\phi = 1/(\phi_U - \phi_L)$$

$$b_r = 1/(r_U - r_L)$$

For rectangular jet problems with a large aspect ratio (> 2/1), a hybrid mapped rectangular/cylindrical grid (Figure 4) would be utilized. As the solution evolves and the jet becomes more circular, the cylindrical origin moves to the flow origin. The procedures entailed in this moving origin methodology will be described in a subsequent section of this report.

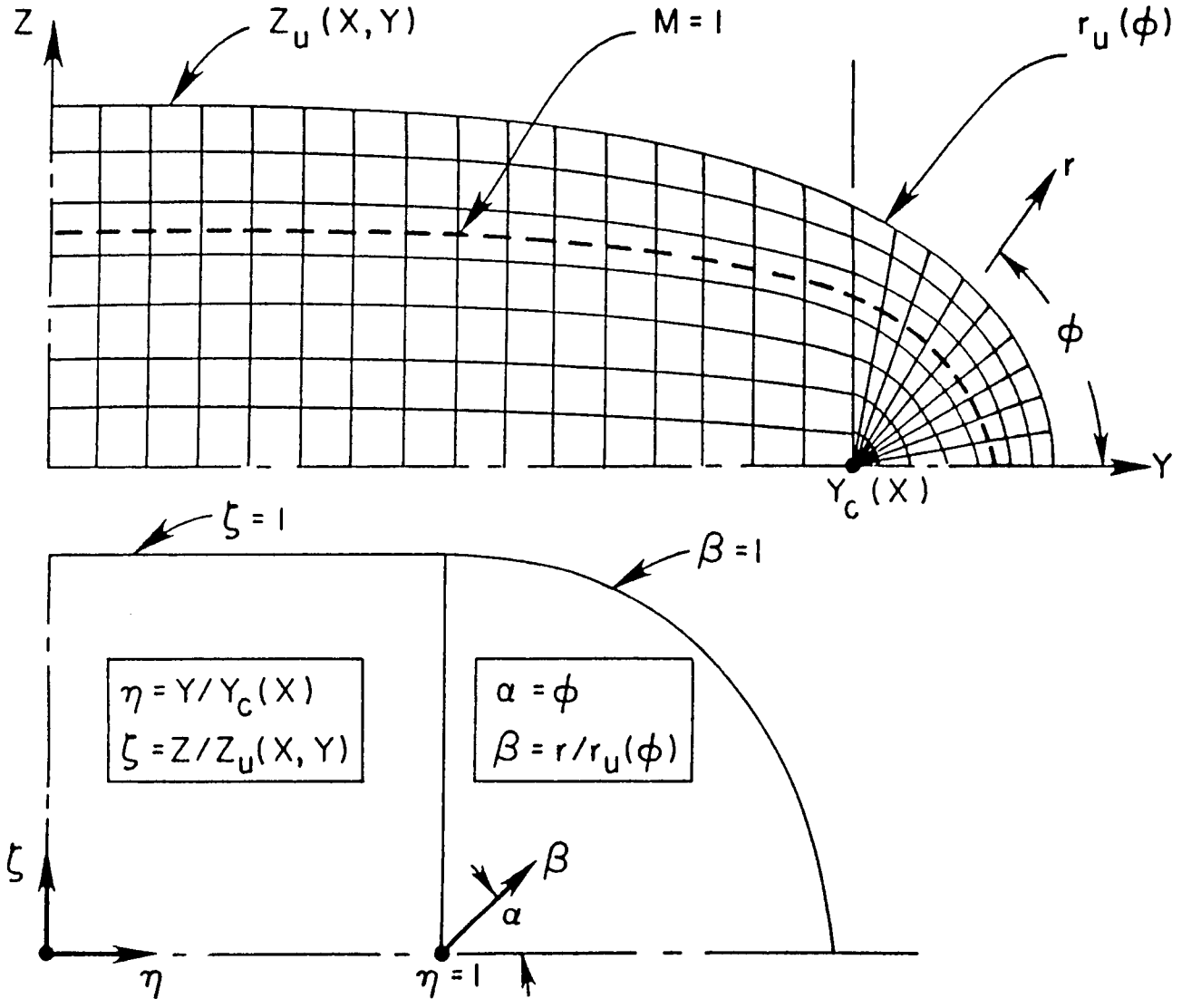

FIGURE 4. Hybrid Rectangular/Circular Mapping In Cross-Flow Plane For Generalized Rectangular Jet Problems.

3. NUMERICAL PROCEDURES FOR ANALYZING SUPERSONIC MIXING PROBLEMS AND NUMERICAL STUDIES

3.1 Interior Point Algorithm

In present versions of SCIP3D, the grid points are equally spaced in both the η and ζ directions. All convective terms are represented using one-sided (two point) difference expressions; diffusive terms are represented using central difference expressions. The solution at interior grid points is obtained using a spatial marching, rotating version of the MacCormack algorithm (see ref. 30). For the grid point, I, J (see Figure 3), this two-step algorithm takes the following form in advancing the solution from ξ to $\xi + \Delta\xi$ ($\sim$ denotes predictor level values; $-$ denotes corrector level values at $\xi + \Delta\xi$; and, ε_y and ε_z are alternated between 0 and 1 at odd/even steps to provide a nonpreferential (rotating) treatment of wave/convective processes).

Predictor Step

$$\begin{aligned}\tilde{E}(I,J) = E(I,J) &- \frac{\Delta\xi}{\Delta\zeta}\left[(1-\varepsilon_y)F_{I+1,J} - (1-2\varepsilon_y)F_{I,J} - \varepsilon_y F_{I-1,J}\right] \\ &- \frac{\Delta\xi}{\Delta\zeta}\left[(1-\varepsilon_z)G_{I,J+1} - (1-2\varepsilon_z)G_{I,J} - \varepsilon_z G_{I,J-1}\right] - H_{I,J}\Delta\xi \\ &+ V_F(I,J)\Delta\xi\end{aligned} \tag{20a}$$

Corrector Step

$$\begin{aligned}\bar{E}(I,J) = \frac{1}{2}\Bigg\{ & E(I,J) + \tilde{E}(I,J) - \frac{\Delta\xi}{\Delta\eta}\left[\varepsilon_y\tilde{F}_{I+1,J} + (1-2\varepsilon_y)\tilde{F}_{I,J}\right. \\ & \left. - (\varepsilon_y-1)\tilde{F}_{I-1,J}\right] - \frac{\Delta\xi}{\Delta\zeta}\left[\varepsilon_z\tilde{G}_{I,J+1} + (1-2\varepsilon_z)\tilde{G}_{I,J} + (\varepsilon_z-1)\tilde{G}_{I,J-1}\right] \\ & - \tilde{H}_{I,J}\Delta\xi + \tilde{V}_F(I,J)\Delta\xi\Bigg\}\end{aligned} \tag{20b}$$

where, for f = U, V_F takes the form:

$$V_F(I,J) = \frac{b^2_y}{\Delta\eta^2} \{ \mu_I^+[f(I+1,J) - f(I,J)] - \bar{\mu}_I[f(I,J) - f(I-1,J)] \}$$

$$+ \frac{b^2_z}{\Delta\zeta^2} \{ \mu_J^+[f(I,J+1) - f(I,J)] - \bar{\mu}_J[f(I,J) - f(I,J-1)] \} \qquad (21)$$

After both the predictor and corrector steps, the conservation array, $\bar{E}(I,J)$, is decoded using standard supersonic flow decode procedures (see ref. 1).

The algorithm utilized is fully explicit and the step-size is limited by both hyperbolic (CFL) and parabolic stability constraints. These are combined in a 'parallel-resistor' manner (viz., $\Delta\xi = (1/\Delta\xi_{HYP} + 1/\Delta\xi_{PAR})^{-1}$) with the CFL constraint satisfied using nonlinear reference plane characteristic intersections. For the fully supersonic jet mixing problems under consideration, the hyperbolic CFL constraint effectively controls the allowable step-size, with the parabolic criterion having little impact on the allowable step-size.

3.2 Grid Distribution and Step-Size Control

Consider the rectangular jet mixing problem with mild (e.g., 2/1) aspect ratio depicted in Figure 5. A simplistic hybrid grid (drawn with extremely crude grid definition) could be utilized to initiate the calculation. As the jet contour takes on an elliptical appearance, the origin would be moved to the left (e.g., rectangular planes are eliminated) until far downstream (when the cross-section is circular), the cylindrical origin coincides with the flow axis of symmetry. Examples illustrating this 'moving origin' methodology will be exhibited.

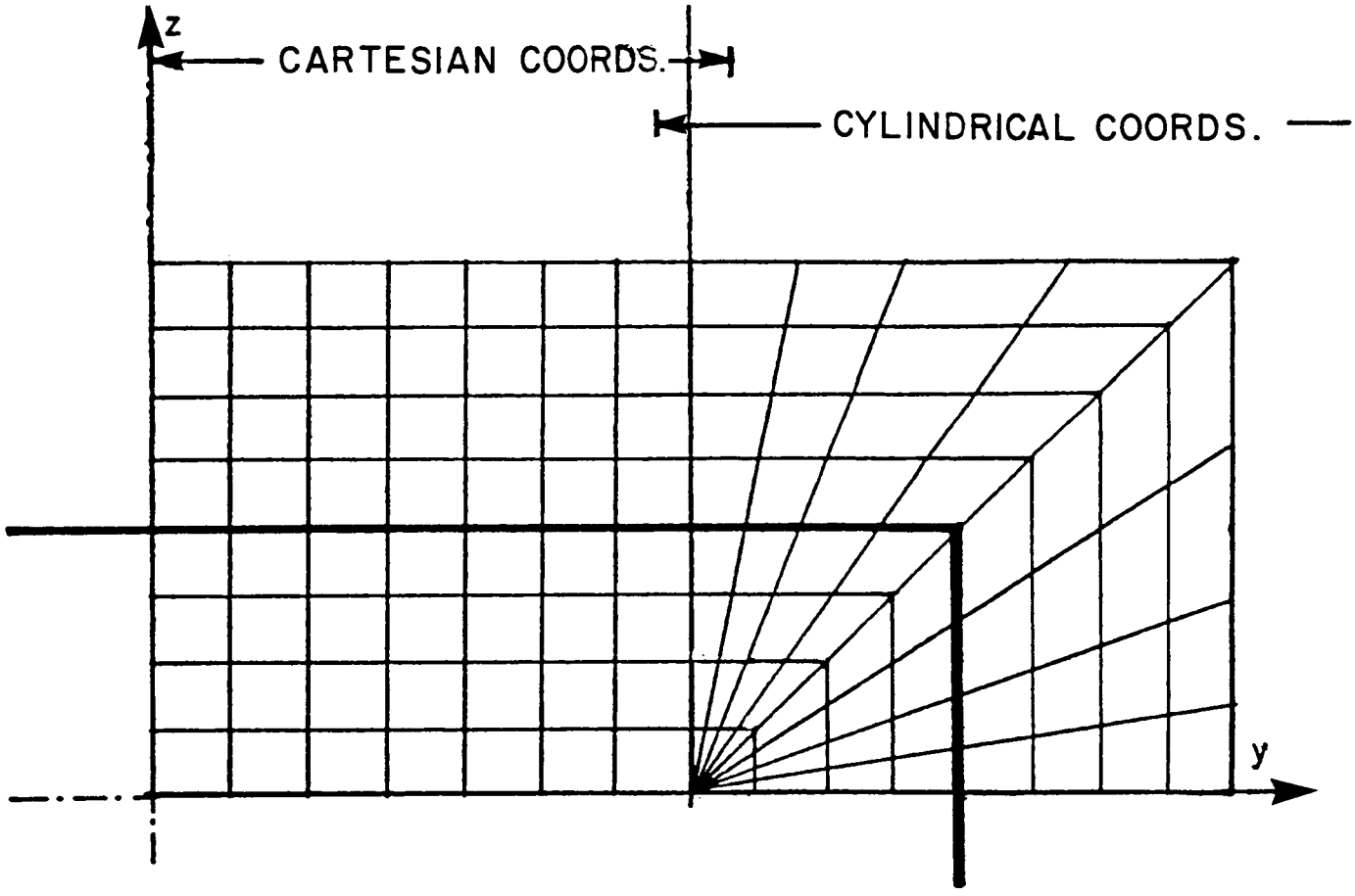

FIGURE 5. Initial Hybrid Grid For Analysis Of Rectangular Jet Mixing Problem.

The coupling of cartesian and cylindrical grids is relatively straightforward, but issues must be addressed in treating grid points near the cylindrical grid origin. Presently, a 'brute-force' approach is employed which utilizes a number of overlap cartesian planes (Figure 6), with properties interpolated from the cylindrical grid solution. Using these overlap planes, the rectangular portion of the flowfield is integrated first at the predictor level to establish boundary conditions for the cylindrical region, which is then integrated at the predictor level. The rectangular portion is then integrated for the corrector step, followed by the integration of the cylindrical region for the corrector step. Only one solution (rectangular or cylindrical) need be kept in core storage at a time. (Note that for very high aspect ratio problems, core storage can be minimized by utilizing several blocks of rectangular grids, each solved independently utilizing overlap planes for coupling). Note that at the hybrid origin, W (= 0) and V in the cartesian system are single valued but in cylindrical coordinates, $\tilde{V} = 0$ and $\tilde{W} = V \cos\phi$. Specialized procedures must be employed to avoid step-size limitations associated with cross-flow differentiation in cylindrical coordinates in the vicinity of the origin due to the small physical spacing between grid points. Again, the present approach is 'brute-force' (e.g., only selective grid points are calculated in accordance with the ratio of $r\Delta\phi$ to $r_u\Delta\phi$). The hybrid grid has only recently been incorporated into the code and further exploratory work appears warranted.

The 'shear layer' initialization for jet interaction problems utilized in SCIP3D is directly analogous to that employed in previous overlaid viscous/inviscid jet models.[31,32] The initialization entails:

(a) determining initial mean flow shear layer profiles centered about the jet slipstream location a small distance downstream of the nozzle exit plane (see refs. 31 and 32 for details); and,

(b) determining initial turbulence parameter ($k\varepsilon$ or kW) profiles based on an equilibrium turbulence hypothesis and the use of a mixing length turbulence model approximation.

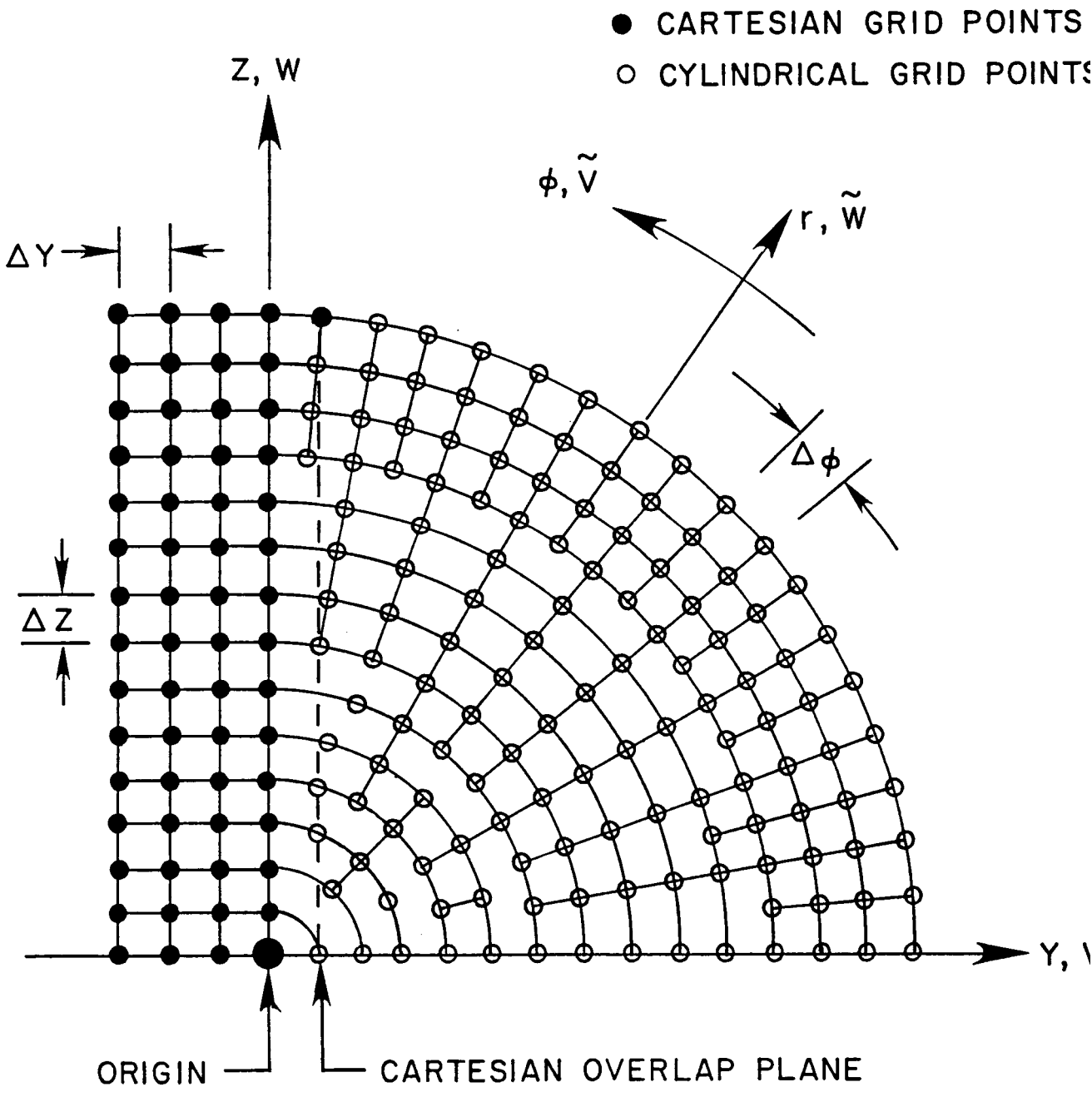

FIGURE 6. Cylindrical/Cartesian Grid Coupling Using Overlap Cartesian Planes.

3.3 Boundary Point Procedures

The following boundary surface types are analyzed in the supersonic version of the SCIP3D model:

(1) solid surfaces (PNS with slip [no BL] or Euler limit);
(2) symmetry planes; and,
(3) jet mixing layer outer edge.

The treatment of symmetry planes, using appropriate odd/even reflection conditions, employs standard techniques. Solid surfaces are treated using a variant of the Abbett wave-correction procedure[33] which incorporates the surface entropy approach and corner point methodology of Dash and Del-Guidice[30]. Jet computational boundaries are configured to fall outside the viscous jet boundary using the growth rate formulation of equation (19) as schematized in Figure 3. For nonuniform supersonic flow surrounding the jet, the external flow can be calculated concurrently using the present shock-capturing algorithm in the inviscid limit. This is accomplished by extending the numerical domain outward sufficiently to capture the bounding outer shock using an estimate of the shock growth with a safety factor. For uniform surrounding flow, the external flowfield can be approximated using a linearized pressure/flow-deflection relation. In applying this approach, the nearfield portion of the jet is solved with the grid encompassing the captured jet induced bow shock (Figure 3) as discussed previously. The jet boundary is calculated using the Abbett wave-correction procedure as will be summarized below.

The approach taken for jets exhausting into uniform supersonic streams assumes that the jet has quarter-plane symmetry and hence, the free stream velocity, U, is aligned with the x coordinate direction. Consider the calculation for upper jet boundary points on the surface $z_U(x)$ (Figure 7). The boundary points, J = JMAX, are first calculated using the interior point predictor/corrector algorithm with backward/backward predictor/corrector convective differences in the z direction and standard alternating predictor/corrector differences in the y direction. This yields properties U*, V*, P*, M*, etc. which do not satisfy the external flow solution. The external flow pressure, P_E, is given by the linearized relation:

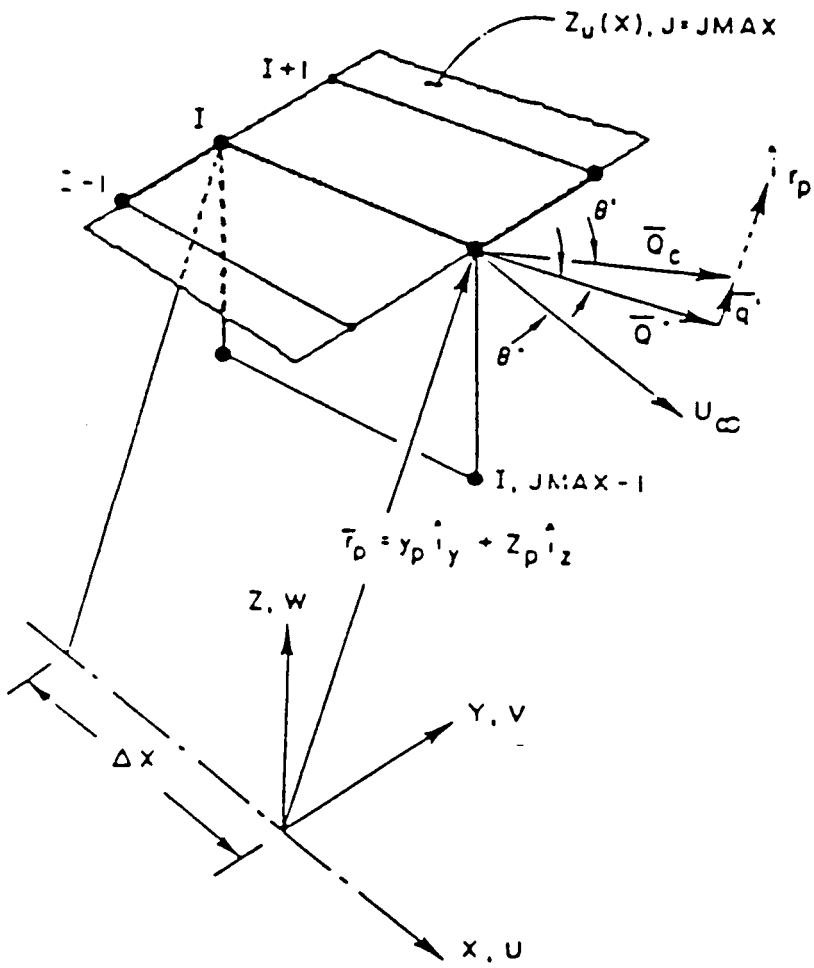

FIGURE 7. Schematic Of Wave-Correction Procedure Used To Couple Jet and Linearized Supersonic Flow Solution At Jet Boundary.

$$P_E = P_\infty \left[1 + \frac{\gamma M_\infty^2}{\sqrt{M_\infty^2 - 1}} \right] (\theta^* + \theta') \tag{22}$$

where θ^* is the flow angle based on the predictor/corrector solution, viz.:

$$\theta^* = S \cdot \tan^{-1} \frac{(V^{*2} + W^{*2})^{1/2}}{U^*} \tag{23}$$

($S = 1$ if $\bar{Q}^* \cdot r_p > 0$; $S = -1$ if $Q^* \cdot \bar{r}_p < 0$; r_p is the position vector to the boundary point in the plane $x = \text{const}$; Q^* is the velocity vector, $Q^* = U^* i + V^* i_y + W^* i_z$) and θ' is a correction to this angle (obtained via perturbing the velocity in the r_p direction only). The corrected boundary pressure is given by an isentropic simple wave rotation from P^*, θ^* conditions, viz.:

$$P_C = P^* \left[1 - \frac{\gamma M_*^2 \theta'}{\sqrt{M_*^2 - 1}} \right] \tag{24}$$

Solving eqs. (22) and (24) simultaneously with P_C set equal to P_E yields the corrected boundary pressure and flow angle. The total enthalpy remains invariant ($H_{T_C} = H_T{}^*$) and the density is expanded isentropically ($\rho_C = \rho^*(P_C/P^*)^{1/2}$). Hence, the magnitude of the corrected velocity is given by (for a perfect gas):

$$Q_C = \left(2H_{T_C} - \frac{2\gamma}{\gamma - 1} \frac{P_C}{\rho_C} \right)^{1/2} \tag{25}$$

and the corrected velocity vector can be written:

$$\bar{Q}_C = \bar{Q}^* + \bar{q}' = U^* i_x + (V^* + v') i_y + (W^* + w') i_z \tag{26}$$

where (since $\bar{q}' = q'i_{r_p}$):

$$v' = q' \left(\frac{y_p}{r_p} \right) \; ; \; w' = q' \left(\frac{z_p}{r_p} \right) \tag{27}$$

Substituting the expressions for v' and w' in eq. (27) into eq. (26), and setting the magnitude of $| \bar{Q}_c |$ to the value given by eq. 25 yields a quadratic expression for the magnitude of $\bar{q}'$; the sign corresponds to that of θ' (i.e., $\bar{q} = | \bar{q}' | i_{r_p}$ if $\theta' > 0$; $\bar{q}' = - | \bar{q}' | i_{r_p}$ if $\theta' < 0$).

In applying the Abbett wave-correction procedure at solid surfaces, the same predictor/corrector sequence discussed above is utilized. Thus, for an upper wall point, $z_u = F(x,y)$, the MacCormack algorithm would be employed with backward/backward differences in the z direction and alternating differences in the y. The resultant velocity vector will not satisfy the boundary condition $\bar{V} \cdot \hat{n} = 0$ and must be rotated through the angle θ' given by $\bar{Q}^* \cdot \hat{n} = | Q^* | \sin\theta'$ yielding

$$\theta' = \sin^{-1} \left\{ \frac{-U^*F_x - V^*F_y + W^*}{(1+F_x^2+F_y^2)^{1/2} Q^*} \right\} \tag{28}$$

with the corrected pressure, P_c, obtained via the relation

$$\ln (P_c/P^*) = \pm\gamma M_*^2 \theta' / (M_*^2 - 1)^{1/2} \tag{29}$$

The corrected density, ρ_c, is obtained from the isentropic relation

$$P_c/\rho_c^\gamma = P_*/\rho_*^\gamma \tag{30}$$

and the corrected velocity, Q_c, is obtained from

$$H^* = \frac{\gamma}{\gamma-1} \frac{P_c}{\rho_c} + \frac{1}{2} Q_c^2 \tag{31}$$

Then, the corrected velocity components are given by:

$$Q_c = Q_c \hat{t} = U_c \hat{t}_1 + V_c \hat{t}_2 + W_c \hat{t}_3 \tag{32}$$

where

$$\hat{t} = \frac{\bar{Q}_* - (\bar{Q}_* \cdot \hat{n})\,\hat{n}}{\bar{Q} - (\bar{Q}_* \cdot \hat{n})\,\hat{n}} \tag{33}$$

For corner points with no cross-curvature (i.e. $Z_u = F(x)$, $y_u = G(x)$), the concurrent satisfaction of $\bar{V} \cdot \hat{n} = 0$ on both surfaces is obtained by applying eq. (29) additively for rotations through the angles $\theta_1' + \theta_2'$ where:

$$\tan\theta_1' = F_x - \frac{W^*}{U^*} \tag{34a}$$

$$\tan\theta_2' = G_x - \frac{V^*}{U^*} \tag{34b}$$

3.4 Corner Problem Test Case

The wave/shock-capturing capabilities of SCIP3D were first checked out by the performance of fundamental 3D corner flow interaction problems. Calculations were performed for:

(1) a double expansion corner;
(2) an expansion/compression corner; and,
(3) a double compression corner.

In these test calculations, waves generated by two perpendicular walls interact with each other. Reference 34 provides details of these elementary cases. These calculations were performed starting with uniform supersonic flow, discontinuously turning the lower and side walls at x = 0. A mapped rectangular domain was implemented for all the calculations employing quarter-plane symmetry. The calculations were terminated before the wave systems reached the symmetry planes.

Boundary conditions at the walls were analyzed using a variant of the Abbett wave correction technique modified to employ the entropy variation along the grid line one grid interval away from the wall (see refs. 30, 34, 35). As discussed in Section 3.3: (1) wall point properties are first calculated using the MacCormack algorithm with differences evaluated 'into the flow' in both the predictor and corrector steps; and (2) the pressure and flow angles are then 'corrected' via a rotation in the plane containing the wall normal and predicted velocity vector so as to satisfy the boundary condition $\overline{V} \cdot \hat{n} = 0$. At the corner point, the Abbett technique is formulated whereby the properties at the corner are evaluated based on: (1) application of the MacCormack algorithm using both Y and Z derivatives 'into the flow' on both predictor and corrector steps; (2) a dual correction procedure to satisfy $\overline{V} \cdot \hat{n} = 0$ on both intersecting surfaces yielding the total turning angle, $\Delta\theta_T$, i.e.,

$$\Delta\theta_T = \Delta\theta_1 + \Delta\theta_2$$

where $\Delta\theta_1$ and $\Delta\theta_2$ are the turning corrections required on the two intersecting surfaces; and, (3) evaluation of the pressure via the relation

$$\ln(P_c\alpha/P_M) = \pm \frac{\gamma M_M^2}{\sqrt{M_M^2 - 1}}\Delta\theta T \qquad (35)$$

where P_M is the value predicted by the MacCormack algorithm and P_c is the corrected value. This approach has been found to work extremely well. Results for the double compression corner test case are described below.

In this Mach 3.17 case, both the lower wall and side wall were turned up by 12.5° generating two intersecting shock waves, as exhibited in the insert of Figure 8. The predicted pressure contours after 18 steps are shown in Figure 8 and exhibit the classic behavior obtained in experiments and using conically invariant marching procedures. The streamwise corner pressure variation is shown in Figure 9 and 'settles down' after several steps to the correct asymptotic value observed experimentally. The initial oscillations occur due to capturing a strong corner shock ($12^1/_2{}^\circ + 12^1/_2{}^\circ$ of abrupt compression) with no initial grid resolution.

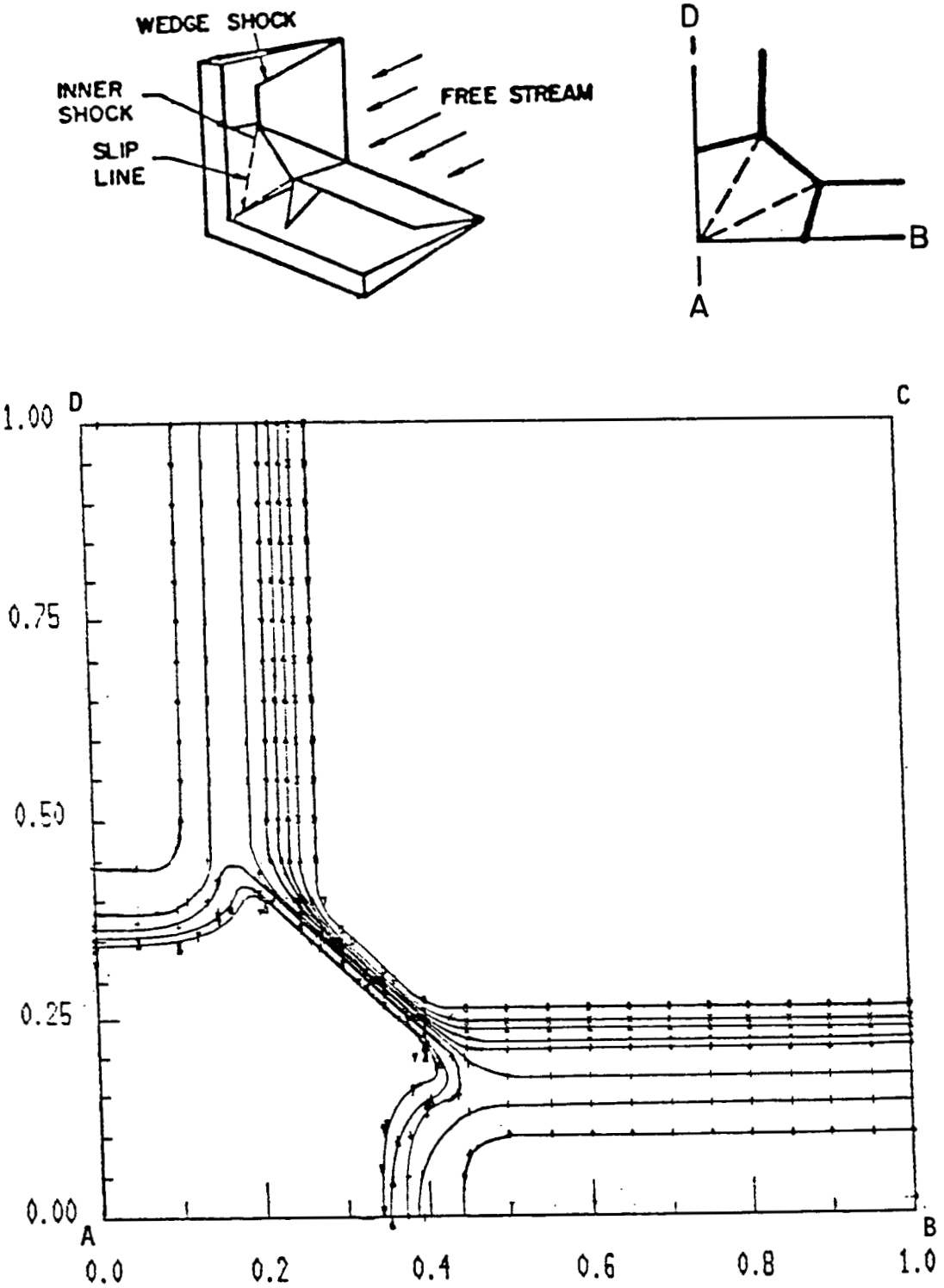

FIGURE 8. Pressure Contours For Double Compression Corner.

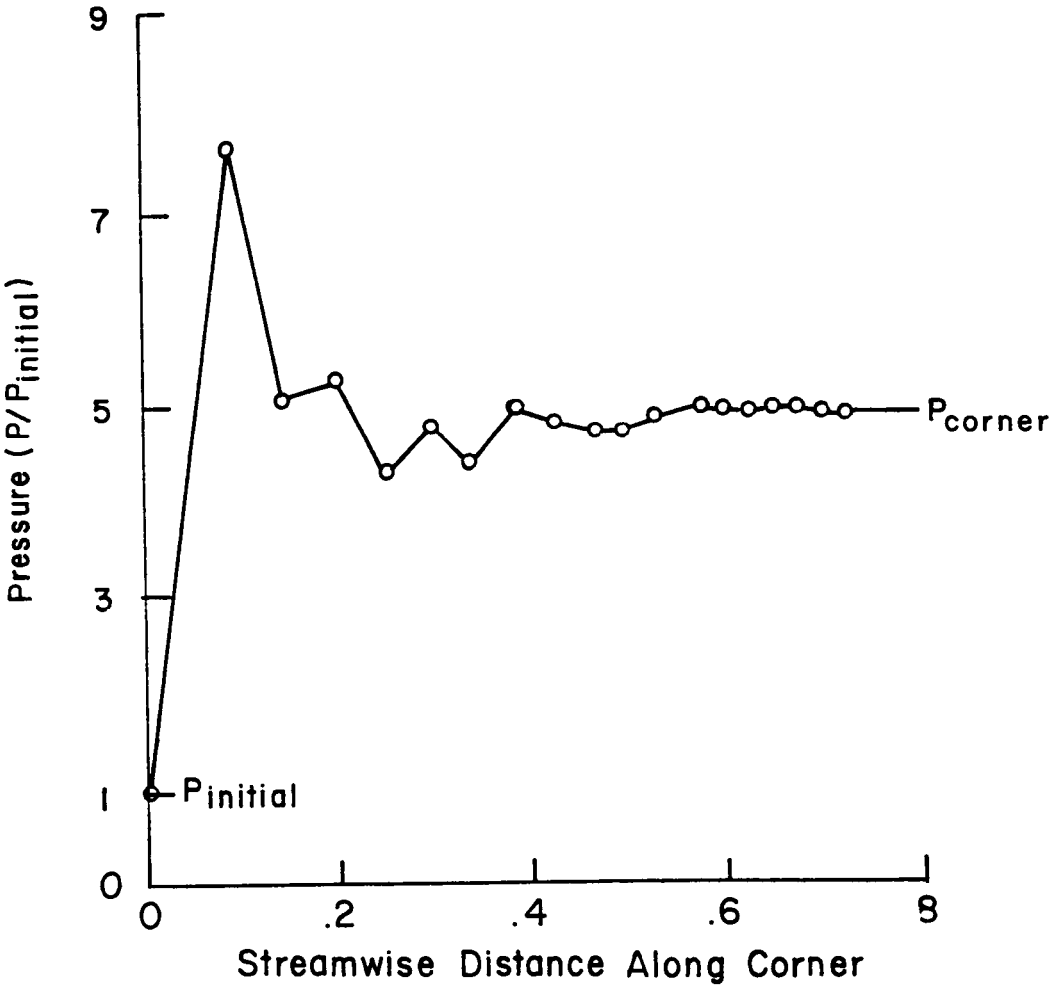

FIGURE 9. Streamwise Variation Of Corner Pressure For Double Compression Case.

3.5 Square Converging-Diverging Nozzle Problem

The next sample calculation was performed for a square converging-diverging nozzle (Figure 10) which encompasses the double-expansion and double-compression wave interactions discussed in Section 3.4. Complete details of this flowfield are given in ref. 34 which describes results utilizing the earlier BIGMAC 3D nozzle model of Dash and DelGuidice. The initial Mach number for this case was 2.94 and the initial pressure was 0.4 atm. The starting profile was uniform. Figure 11 exhibits predicted temperature contours on the symmetry planes (quarter plane symmetry was assumed) and pressure contours at the station x = 15 showing the occurrence of dual plane shock interactions. Figure 12 exhibits the predicted streamwise variation of Mach number along the axis and comparisons with the results of Chang[36] (which terminated at the shock). Figure 13 exhibits the streamwise variation of pressure along the axis and comparisons with results of the GIM code[37]. Figure 14 exhibits the predicted streamwise pressure variation along a wall/axis juncture. The results compare favorable with those of the GIM code and with previous BIGMAC shock-capturing results[34] (not shown). The predicted streamwise pressure variation along the corner is shown in Figure 15.

3.6 Balanced Pressure Square Jet Problem

This calculation was performed for a hot Mach 3 jet (T_J = 2000 °K) exhausting into a colder Mach 3 uniform external stream (T_E = 500 °K) - the resultant jet velocity ratio, U_J/U_E, was 2/1. The calculation was performed with a 21x21 square grid utilizing the 'uniform jet' startline procedure described in Section 3.1, to provide initial shear layer profiles. Of interest is the transition from square to circular type contours. The predicted outer jet boundary contours (ϕ = 0.01) shown in Figure 16 for several x stations [ϕ represents an inert species, viz., ϕ = 1 in the unmixed jet and equals 0 in the external streams; for Pr = 1, ϕ also represents the nondimensional axial velocity distributions, i.e., $\phi = (U-U_E)/(U_J-U_E)$ for constant pressure mixing] clearly exhibit this transition. At $x/r_j \sim 20$, the boundary contour still has a distinct noncircular appearance while at $x/r_j \sim 40$, the contour starts to appear

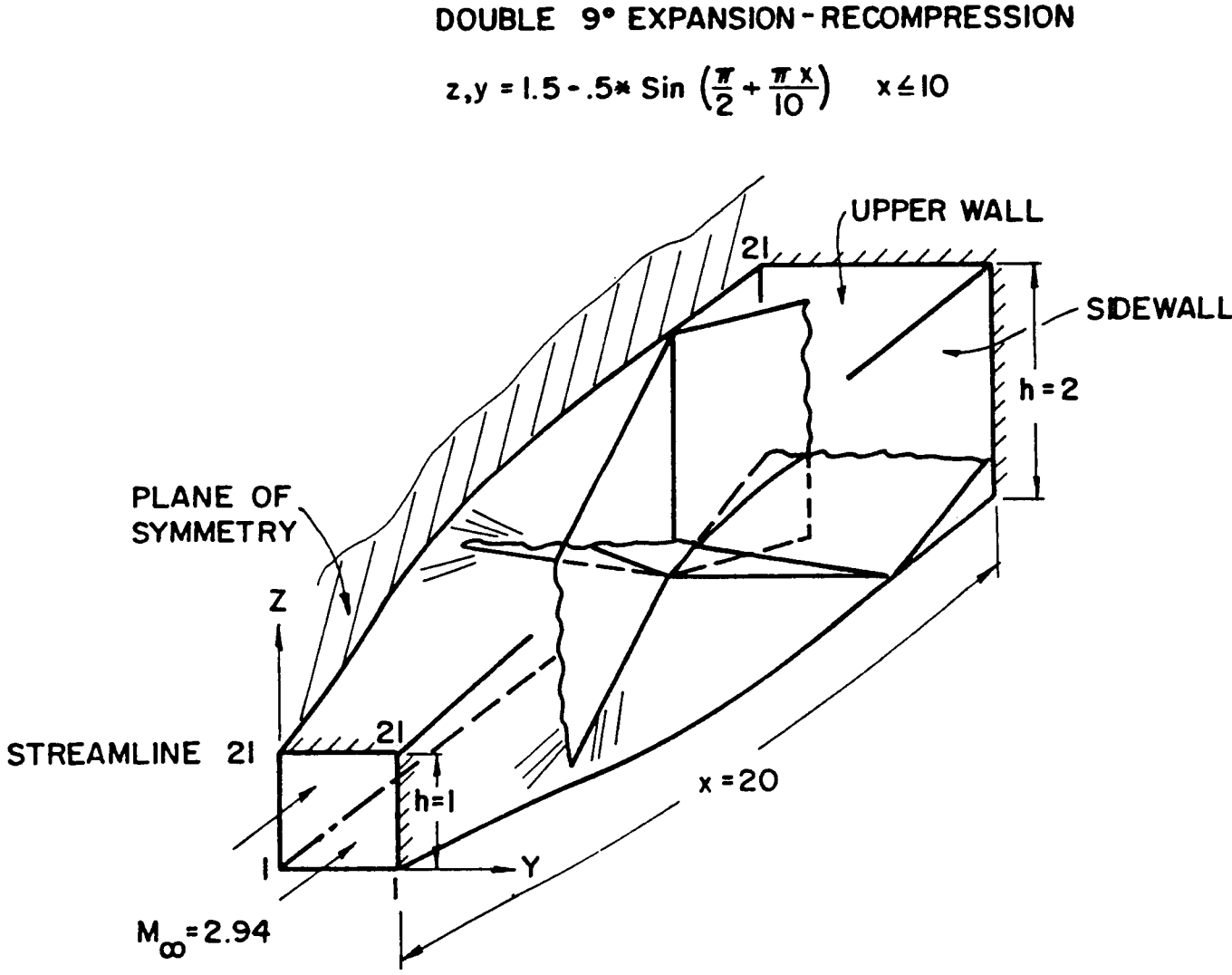

FIGURE 10. Square Converging-Diverging Nozzle.

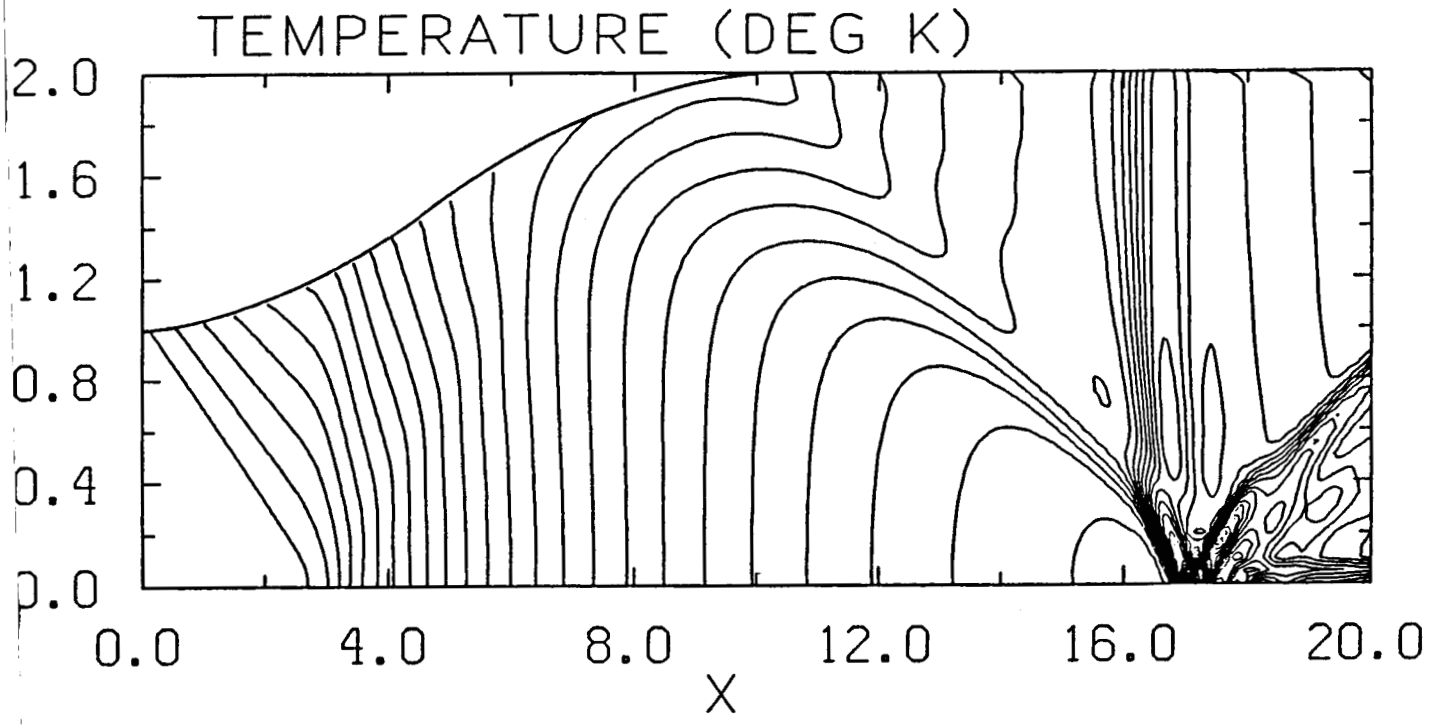

IGURE 11. Temperature Contours On Symmetry Plane for Square CD Nozzle Problem.

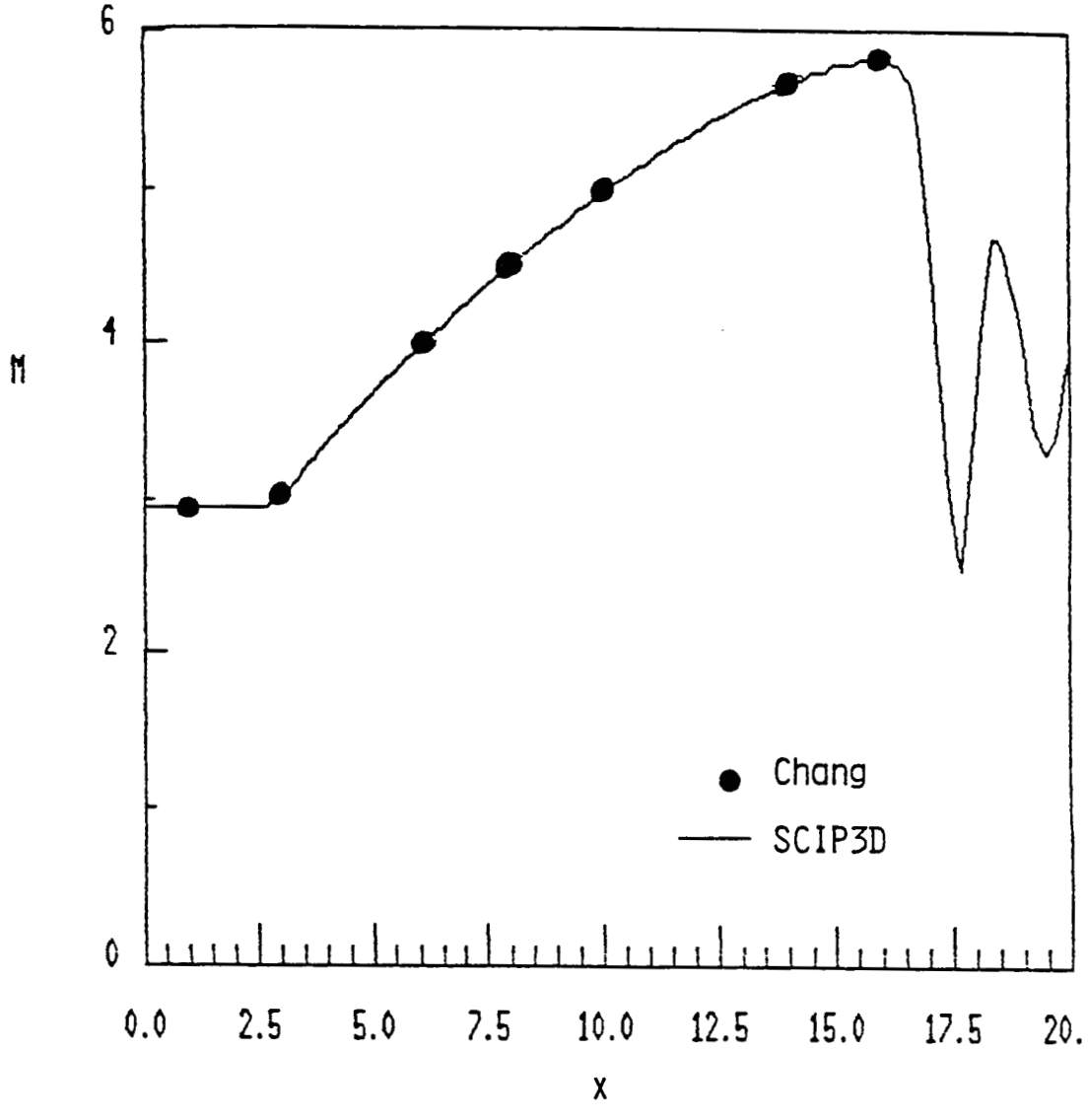

FIGURE 12. Streamwise Variation Of Mach Number Along The Axis For Square Nozzle Problem.

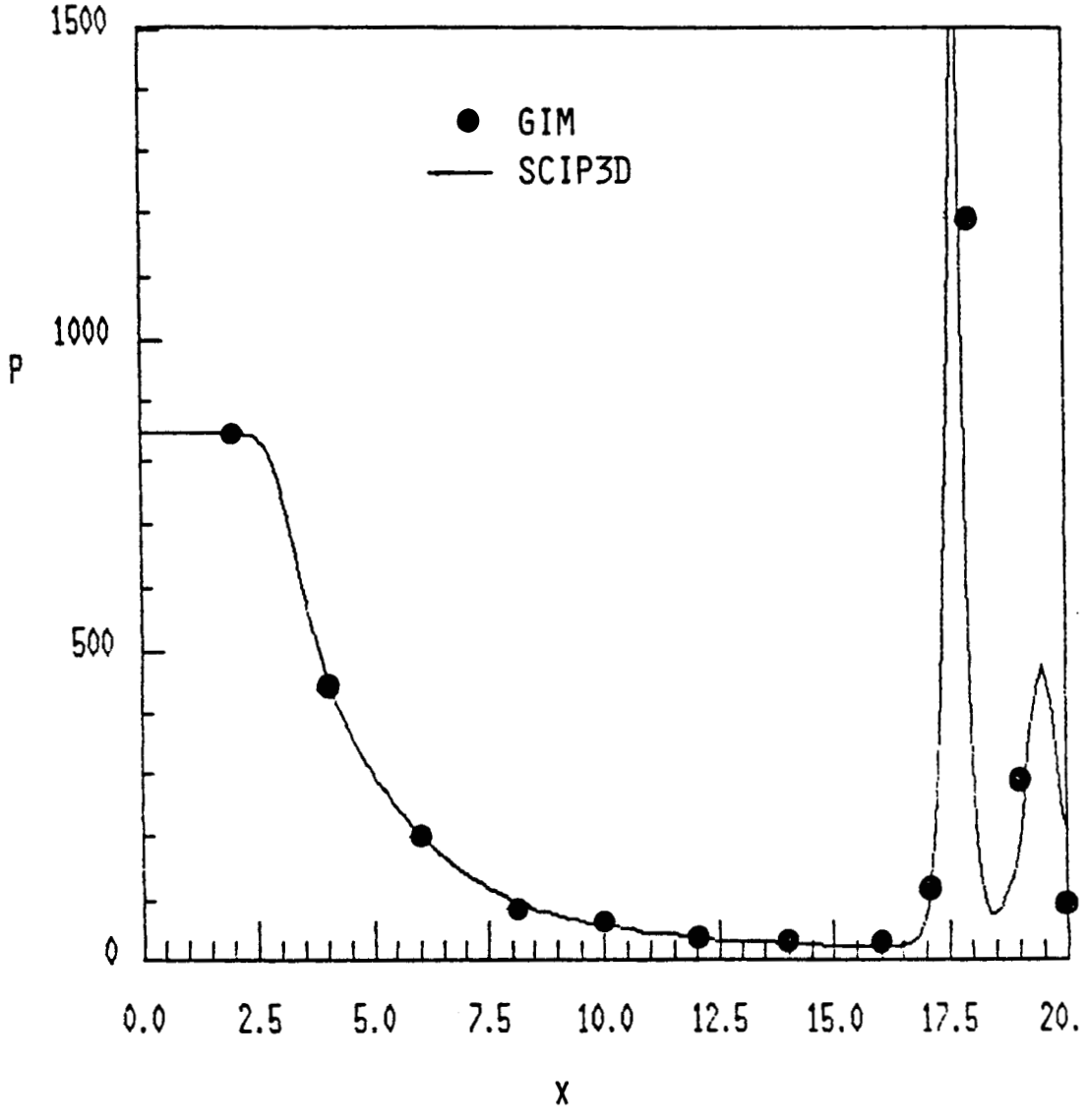

FIGURE 13. Streamwise Variation Of Pressure Along The Axis For Square Nozzle Problem.

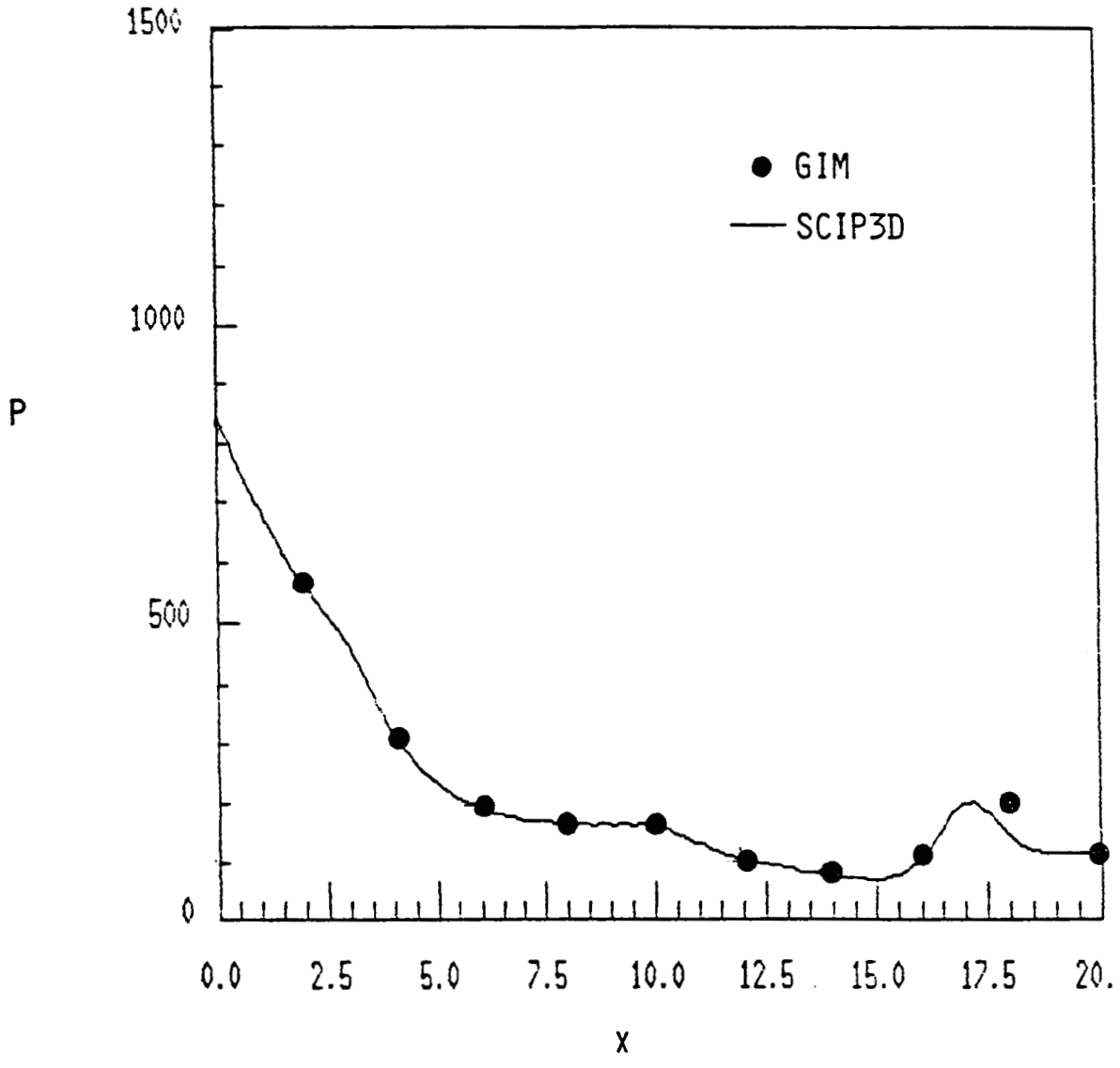

FIGURE 14. Streamwise Variation Of Pressure Along Wall/Axis Juncture For Square Nozzle Problem.

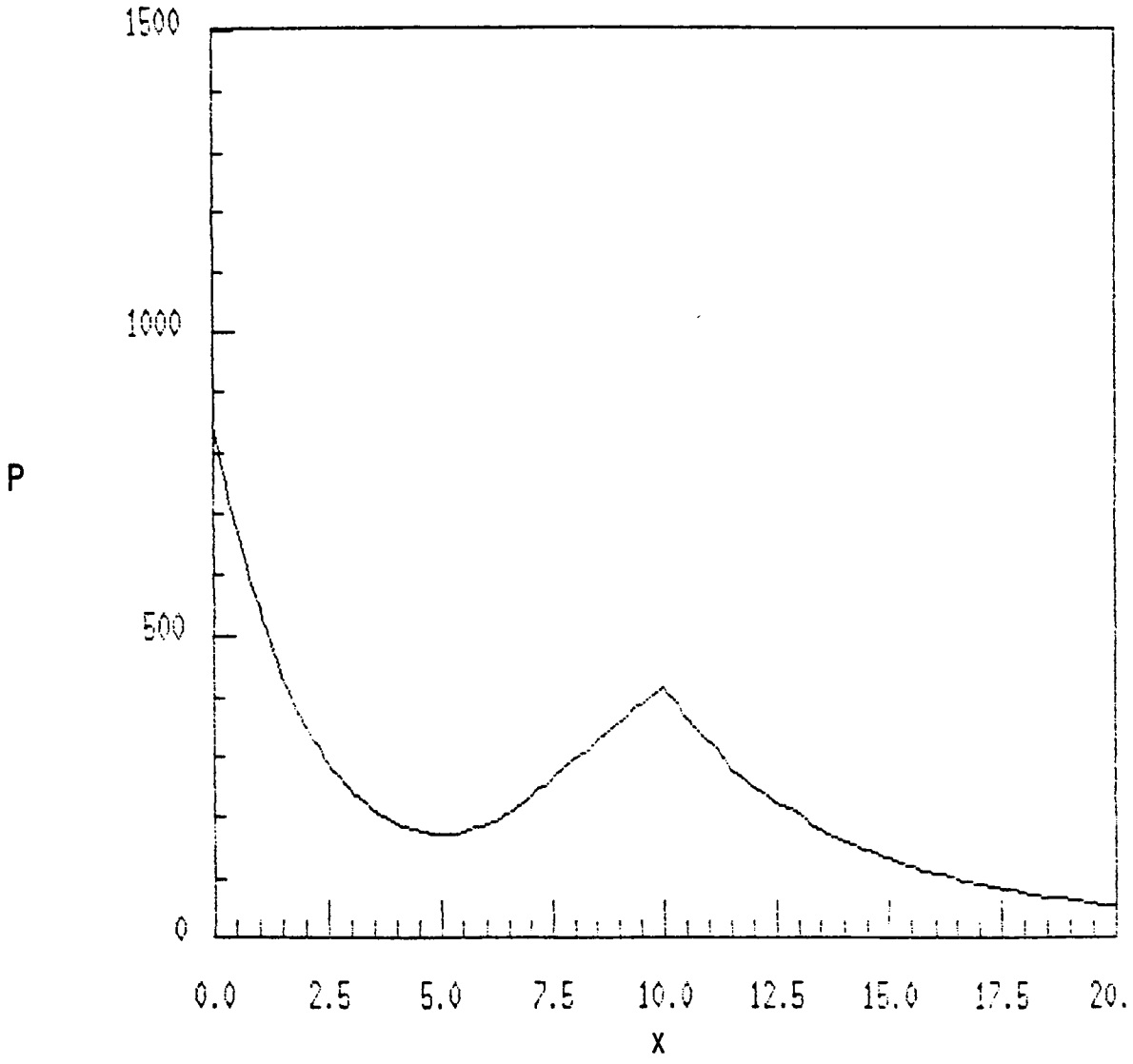

FIGURE 15. Streamwise Variation Of Pressure Along The Corner For Square Nozzle Problem.

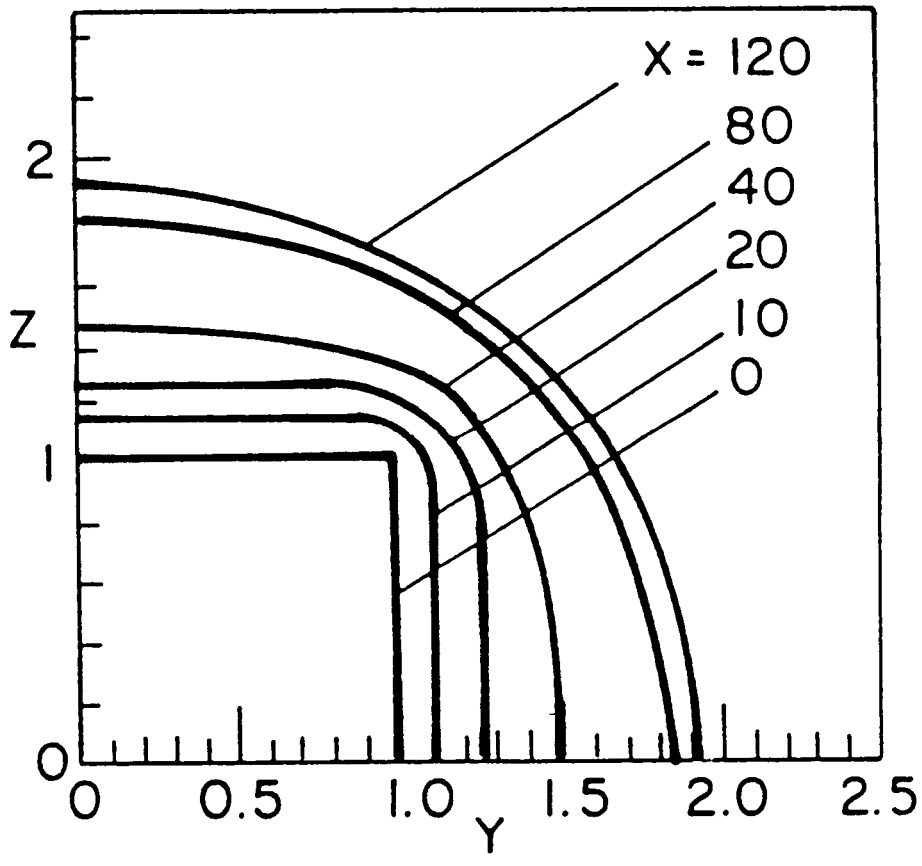

FIGURE 16. Jet Boundary Contours For Balanced Pressure Square Jet Problem, $k\varepsilon$ Turbulence Model Utilized.

circular. At $x/r_j \sim 80$, the outer contour is essentially circular as is the entire jet solution (Figure 17).

We note that at $x/r_j \sim 20$, the peak turbulence levels (Figure 18) occur on the two symmetry planes and are well off axis, characteristic of shear layer-like behavior, while further downstream, peak levels are centered about the jet axis. The predicted variation of the turbulent kinetic energy, k, and the species parameter, ϕ, along the jet axis are exhibited in Figure 19 and are compared with SCIPVIS[1] predictions for the 'corresponding' circular jet (the square jet was initially 2x2; the circular jet had an initial diameter of 2). The square jet is predicted to mix somewhat faster than the circular jet (which was also predicted using 21 grid points and the same turbulence model). If we perform the comparison for jets of equal mass flux on a scaled basis (viz., k, ϕ vs. $x/\pi A$), the circular jet would mix faster than the square jet. Figure 20 compares the predicted axial species decay along the jet centerline using the $k\varepsilon$ and kW turbulence models. The $k\varepsilon$ model is seen to predict substantially faster mixing in accord with past observations for axisymmetric jet problems (see ref. 1). Figure 21 depicts predicted species (ϕ) and temperature (T) contours in the plane of symmetry ($y = 0$ or $z = 0$) obtained using the $k\varepsilon$ turbulence model.

3.7 Underexpanded Square Jet Problem

The same square jet problem described above was repeated with the jet exhaust pressure boosted to 2 atm ($P_J/P_E = 2/1$). The calculation was performed in both rectangular and cylindrical coordinates.

3.7.1 Rectangular Coordinate Solution

The rectangular coordinate calculation was performed with a 21 x 21 rectangular grid initially spread evenly over the quarter plane domain $0 < y < 2$ and $0 < z < 2$. The calculation initiates with a Prandtl-Meyer fan propagating inward from the nozzle trailing edge lip to the axis, and with a plume induced bow shock propagating outward. Figure 22 exhibits pressure contours for this case on the symmetry planes ($y = 0$ or $z = 0$) with the extent of the shear layer ($.1 < \phi < .9$) superimposed. The symmetry plane

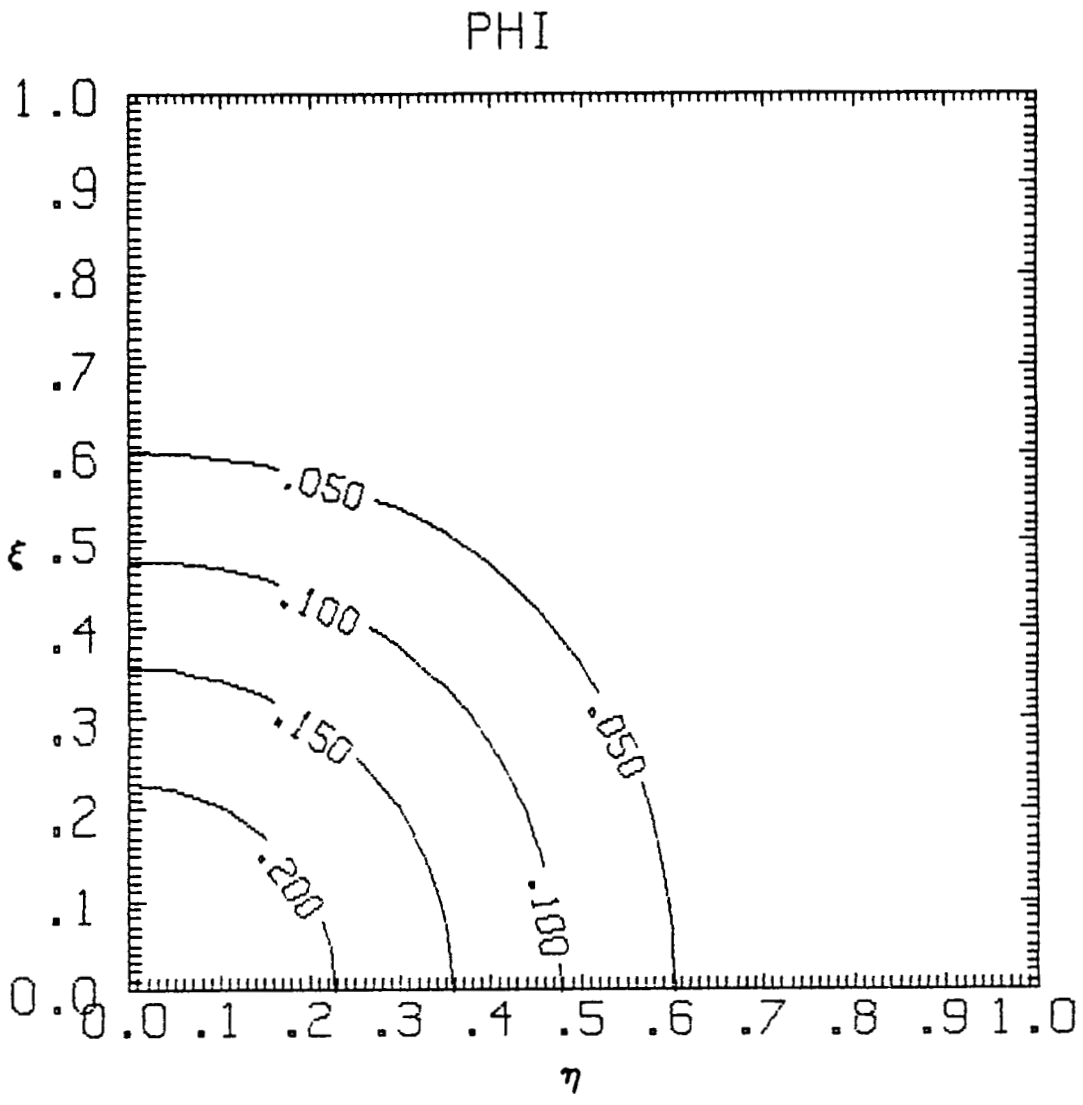

FIGURE 17. ϕ Contours At x/r_j = 80 For Balanced Pressure Square Jet Problem, kε Turbulence Model Utilized.

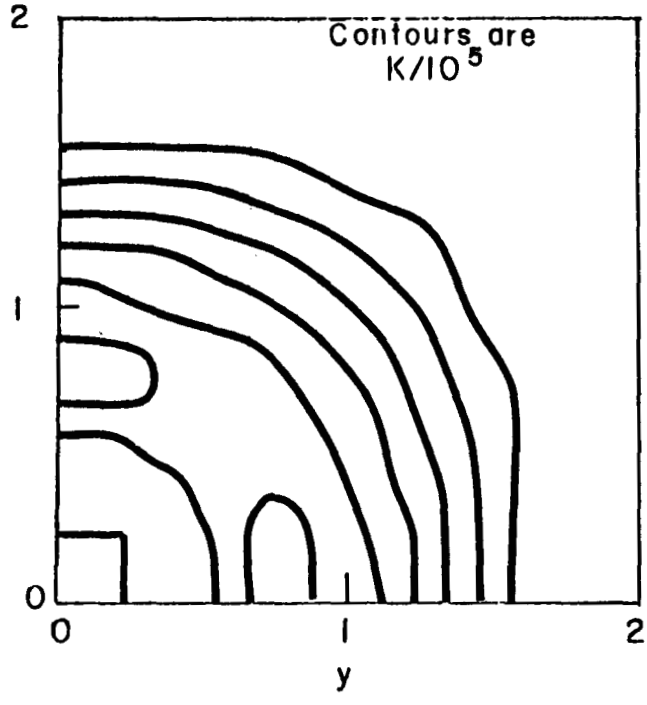

FIGURE 18. Turbulent Kinetic Energy Contours At $x/r_j = 20$ For Balanced Pressure Square Jet Problem, $k\varepsilon$ Turbulence Model Utilized.

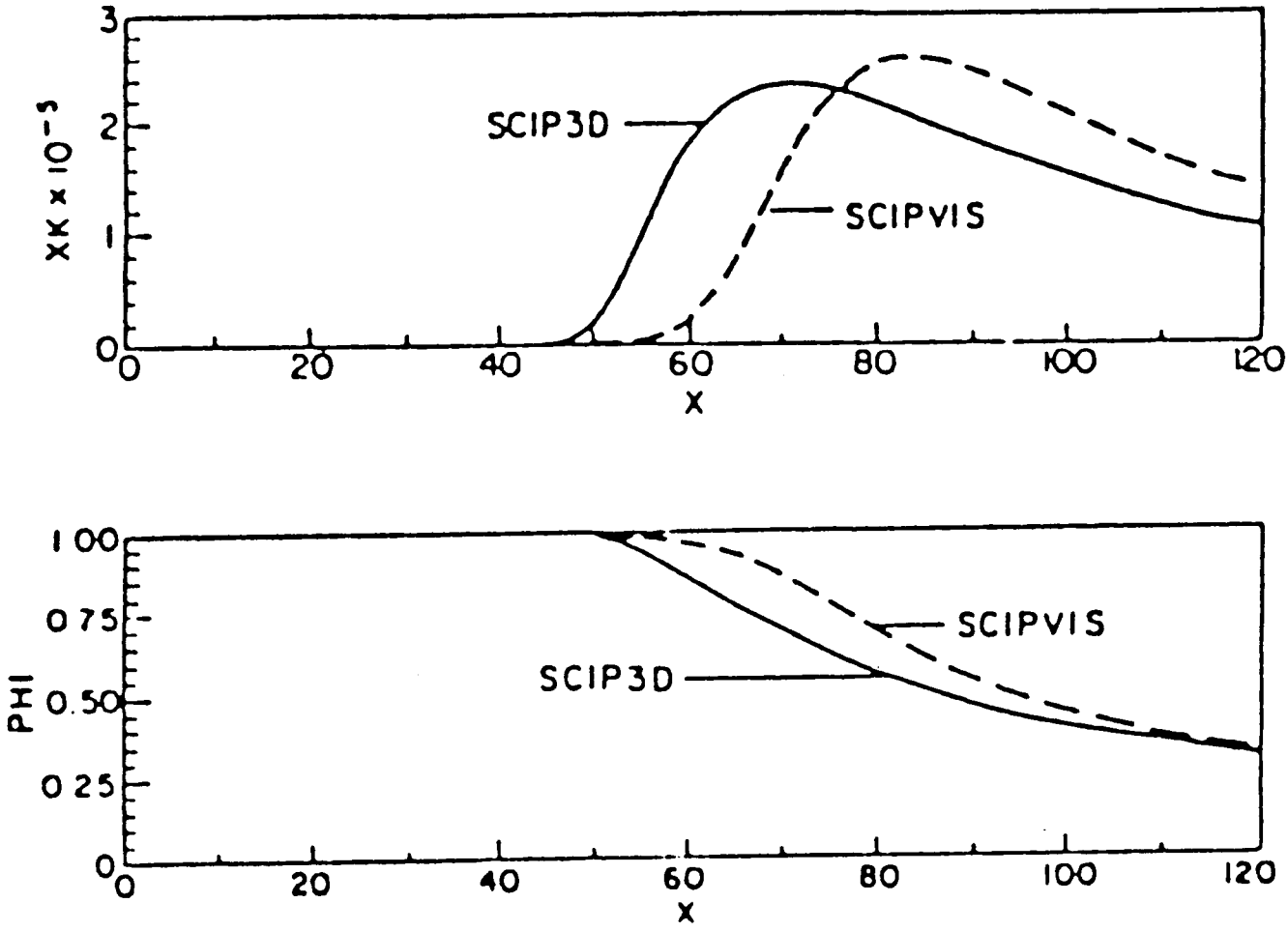

FIGURE 19. Variation Of Turbulent Kinetic Energy (XK) And Species Parameter (PHI) Along Axis Of Symmetry For Square (SCIP3D) And Circular (SCIPVIS) Jets - kW Turbulence Model Utilized.

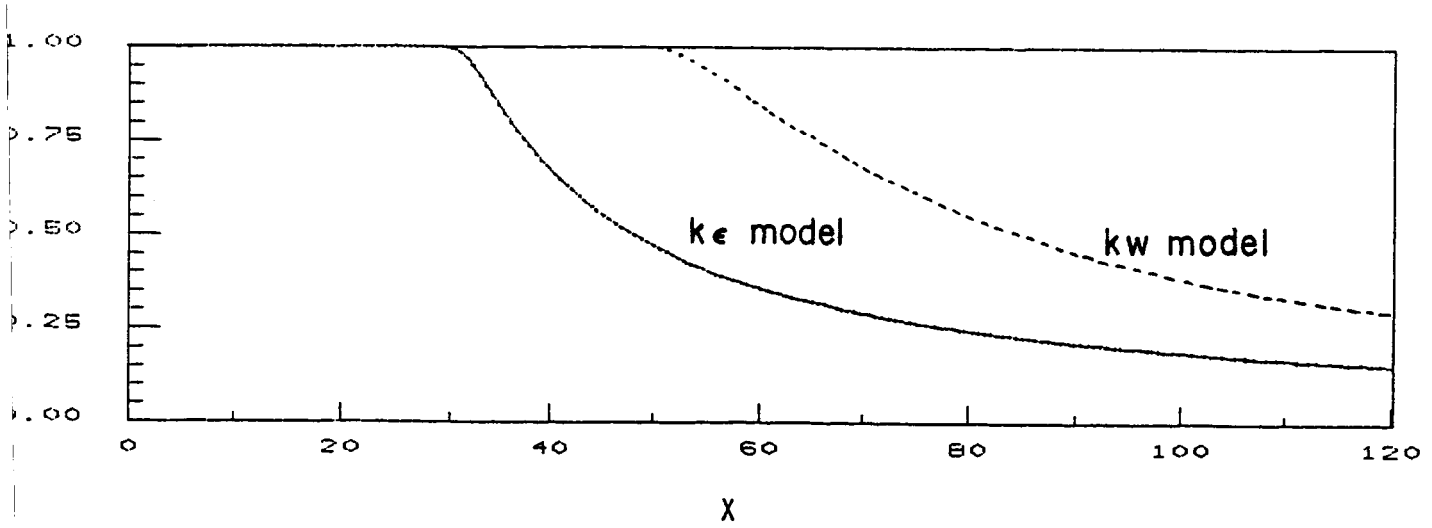

FIGURE 20. Comparison Of kε And kW Turbulence Model Results For Species Centerline Decay For Square Jet Problem.

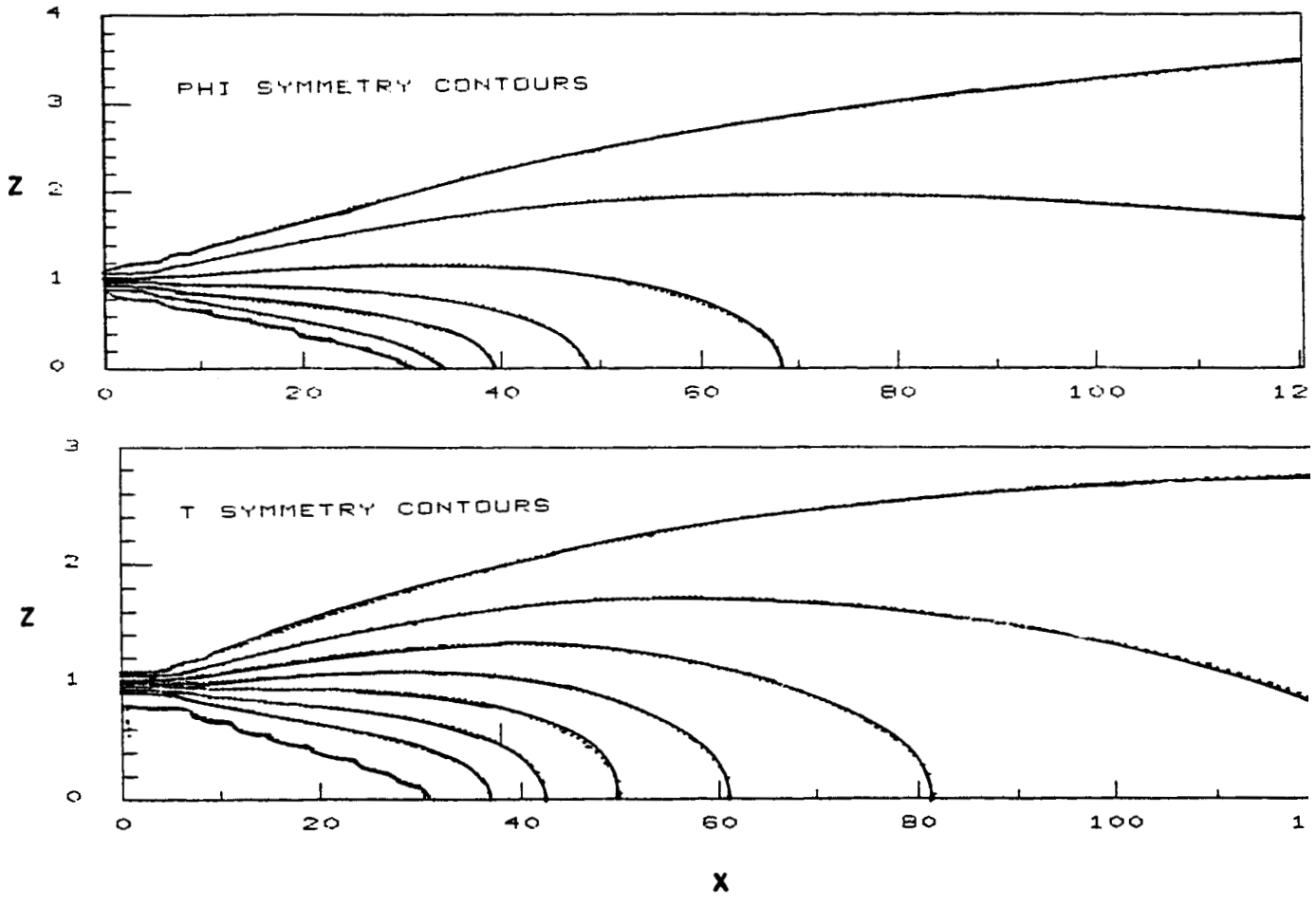

FIGURE 21. Predicted Species (PHI) and Temperature (T) Contours In Plane Of Symmetry For Square Jet Problem - kε Model Results.

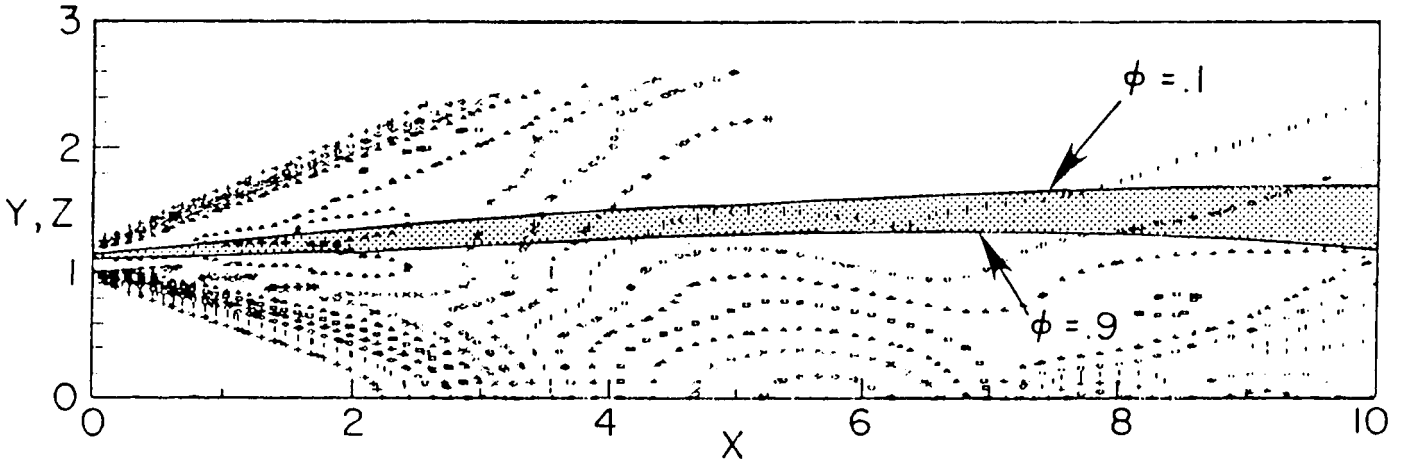

FIGURE 22. Pressure Contours In y,z = 0 Symmetry Planes For Under-expanded Square Jet Problem, Rectangular Coordinate Solution.

plot closely resembles the analogous 2D/axisymmetric jet solution plot. However, contours in the cross-flow planes, x = constant, clearly exhibit the 3D characteristics of this flow.

Figure 23 exhibits several pressure contours in the cross-flow planes at stations $0 < x < 10$. The square startline solution ($x \sim 0$) just downstream of the cowl lip depicts the inward expansion and outward compression process quite distinctly. The pattern at $x = 2$ shows the complex effects of the interaction of the initially planar/perpendicular wave fronts. On the symmetry planes $y = z = 0$, the pattern is 2D like but on the 45° plane ($y = z$), the 3D interactions of the waves are quite evident (e.g. the contour of minimum pressure centered about $y = z \sim .75$ results from the interaction of the two side expansions, etc). The wave fronts of the barrel shock can be distinguished at $x = 6$ and the pattern is highly three-dimensional. The reflected wave fronts are distinguishable at $x = 8$ and $x = 10$.

Figure 24 depicts ϕ contours at these same axial stations showing the evolution of the jet shear layer contour from square to rounded shapes. The initially square contours take on a somewhat irregular shape initially in response to the 3D convective cross-flow velocities generated by the pressure field. At $x = 10$, the contours again become smooth with rounding about the 45° plane, and downstream, will take on rounded shapes as in the balanced pressure case. The outer jet contours ($\phi = .1$) for the first several radii are compared on a single plot in Figure 25 for both the nearfield ($0 < x < 10$) solution and further downstream to $x = 40$.

The SCIP3D predicted nearfield centerline pressure variation is compared with SCIPVIS predictions for 'corresponding' planar (2D) and circular (AXI) jets (Figure 26). The initial square jet pressure decay predicted by SCIP3D is bounded by the planar and circular SCIPVIS predictions. The square jet recompression initiates downstream of the circular case and the pressure variation is more rapid with an overshoot occurring at $x \sim 8$ that is not evidenced in the circular or planar situations.

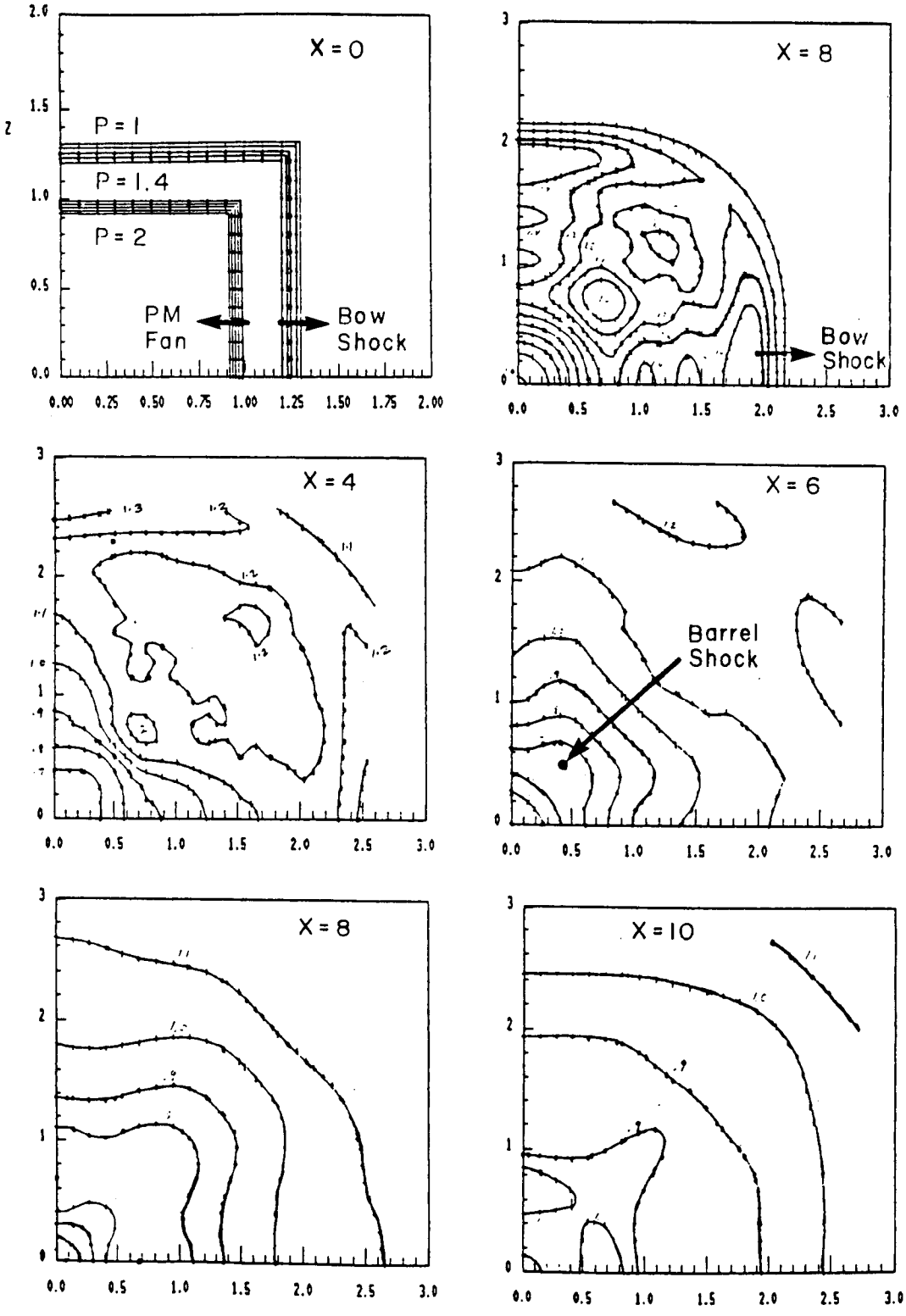

FIGURE 23. Cross-Flow Pressure Contours For Square Underexpanded Jet Problem, Rectangular Coordinate Solution.

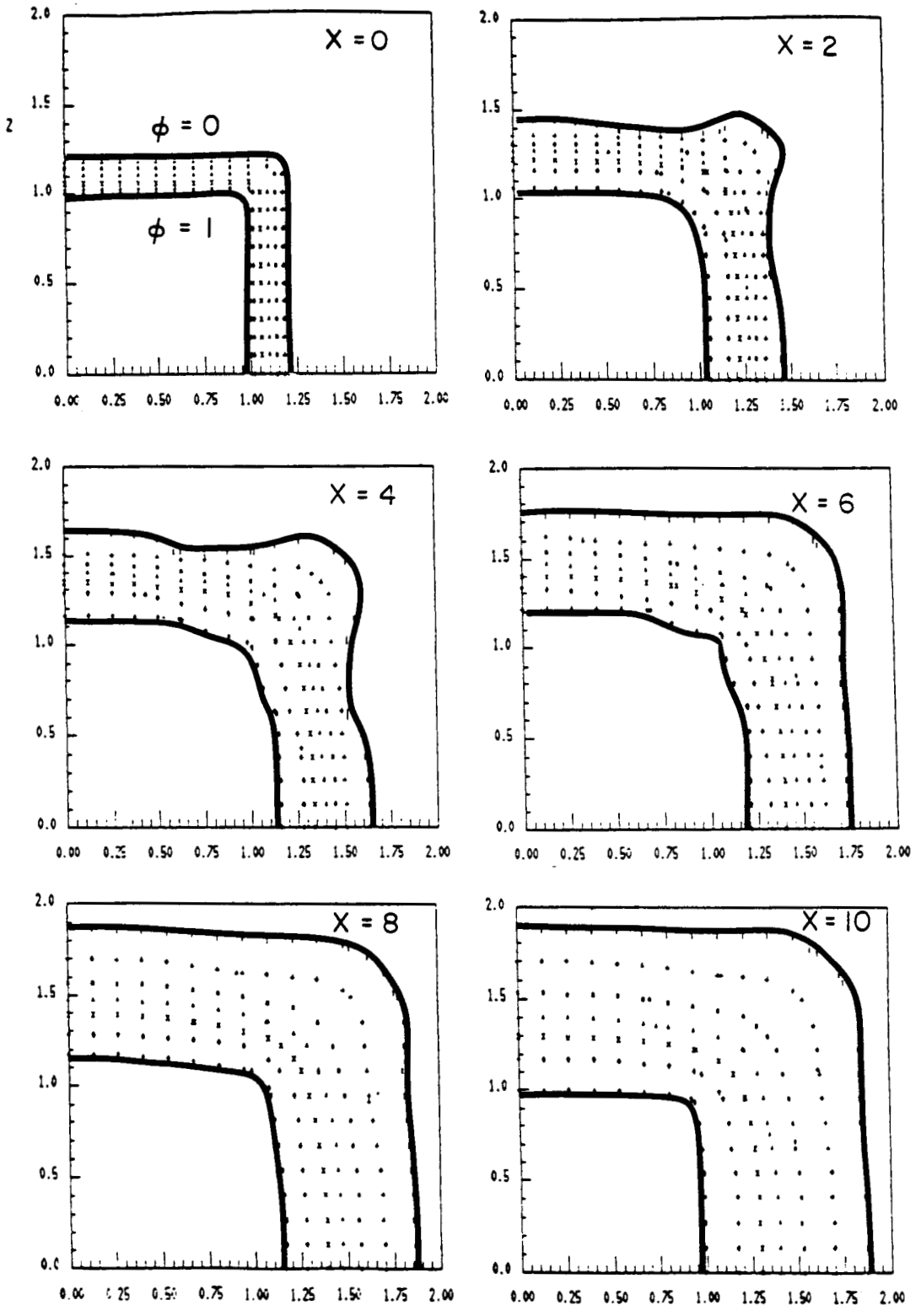

FIGURE 24. Cross-Flow ϕ Contours For Square Underexpanded Jet Problem, Rectangular Coordinate Solution.

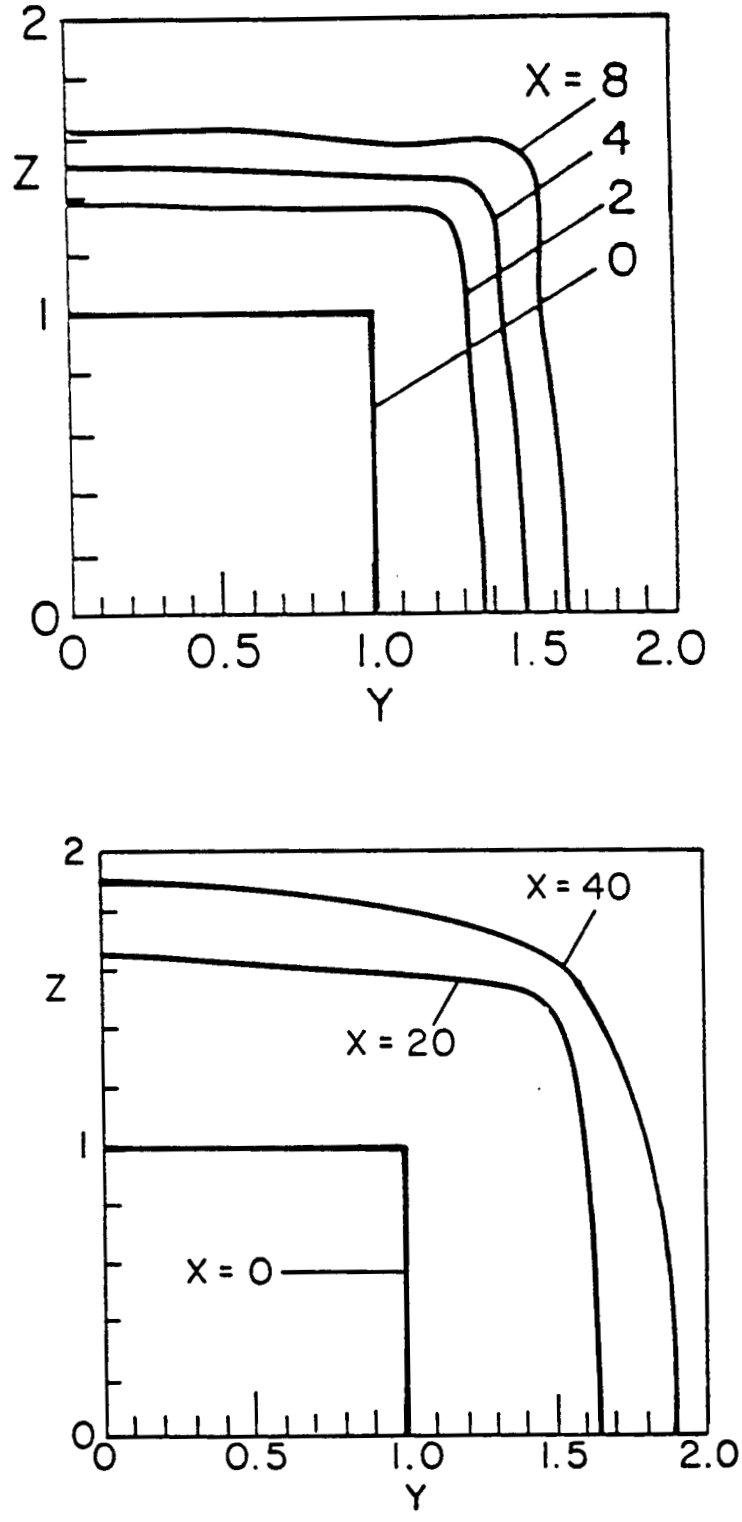

FIGURE 25. Outer Jet Contours (ϕ = .1) For Underexpanded Square Jet Calculation.

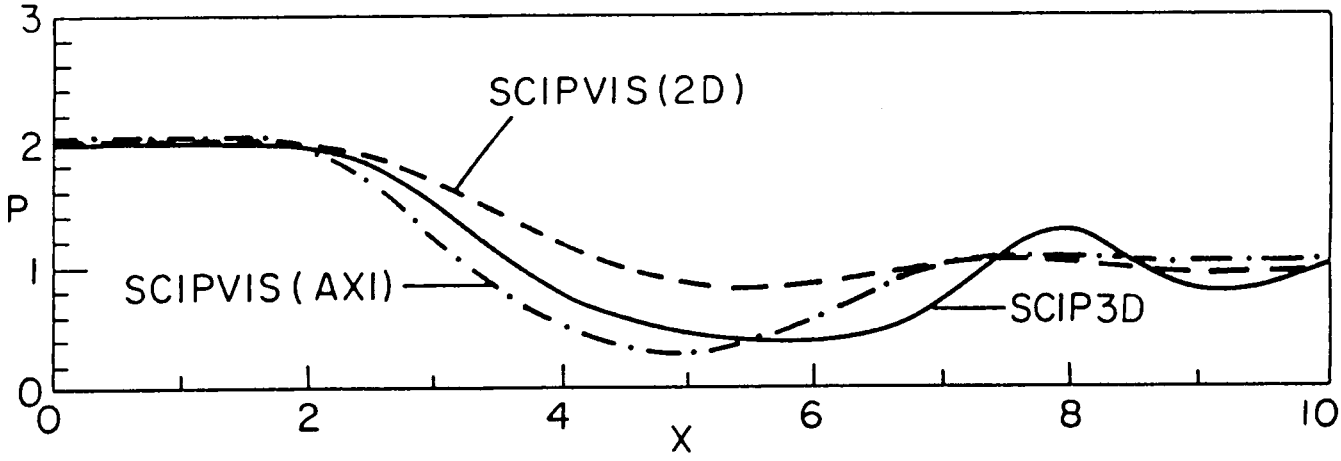

FIGURE 26. Comparison Of SCIP3D Predicted Centerline Pressure Variation For Underexpanded Square Jet Problem With SCIPVIS Predictions For Analogous Planar (2D) and Axisymmetric Jet Problems.

3.7.2 Cylindrical Coordinate Solution

In the rectangular coordinate solution, the boundaries $z_u(x)$ and $y_u(x)$ moved outward to encompass the viscous jet as per the discussion of Section 2.5 and the Figure 3 schematic. In cylindrical coordinates, the outer boundary, $r_u(x,\phi)$, adapts to the shape of the jet contour. Figure 27 depicts the cylindrical grid at x = 0 and x = 10 employed for this problem (21 points in the r direction and 12 points in the ϕ direction were utilized). Figure 28 exhibits pressure contours in the symmetry planes (ϕ = 0 and $\pi/2$) which should be compared with those of the rectangular solution (Figure 28). A comparison of predicted centerline pressures along the jet axis, and, predicted jet outer boundary variations in the symmetry plane are exhibited in Figure 29 for the cartesian and cylindrical solutions. The jet boundary variations are seen to be essentially identical. The axis pressure variations are comparable for $0 < x < 8$ but have some departures downstream, possibly due to the different grid resolution in the cross-flow direction which could affect the near-axis solution in the vicinity of shock reflection.

A comparison of ϕ contours at $x/r_j = 10$ (Figure 30) for the cartesian grid and cylindrical grid solutions shows that the mixing characteristics of the two solutions is essentially grid independent. Cross-flow velocity vectors for the cylindrical grid solution at x/r_j = 2, 4, 6, 8 and 10 are exhibited in Figures 31A, B, C, D, and E respectively, and clearly exhibit the wave effects. At x/r_j = 2 and 4 the plume is expanding and the cross-flow is small relative to the grid lines, ϕ = constant. At x/r_j = 6, the flow is recompressing and a barrel shock is propagating towards the axis (see also, the pressure contours of Figure 23). The cross-flow is seen to be highly three-dimensional in the vicinity of the barrel shock. At x = 8 the barrel shock has reflected from the axis, and, at x = 10, the reflected shock has propagated back into the flow turning it parallel to the axis.

3.8 Balanced Pressure 4/1 Aspect Ratio Rectangular Jet Problem

This quarter plane symmetry calculation was performed for an exhaust emanating from a rectangular nozzle ($0 < y < 2$; $0 < z < 1/2$) with the

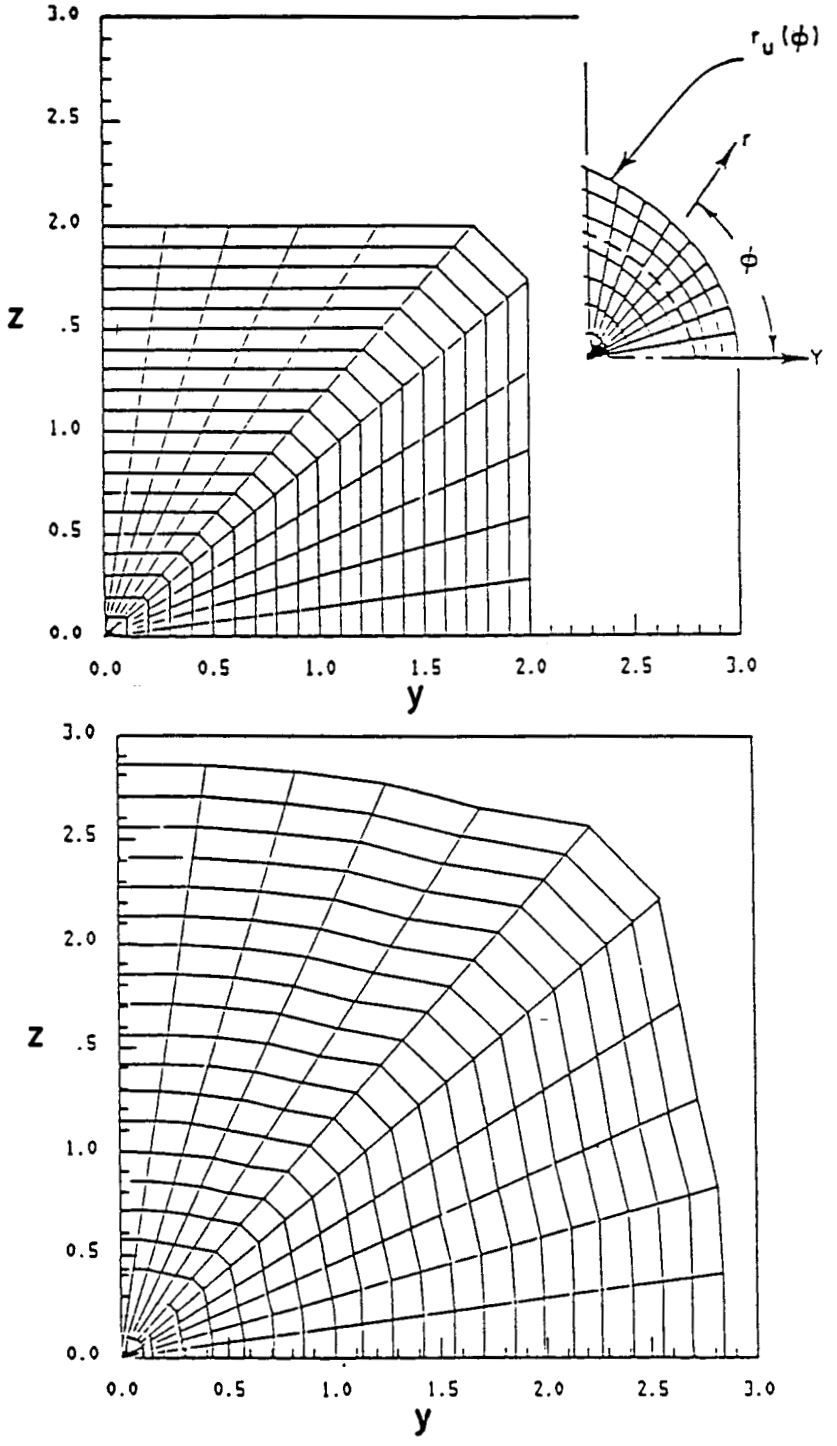

FIGURE 27. Adaptive Cylindrical Grid; Grid Distribution At x = 0 And 10 For Underexpanded Square Jet Problem.

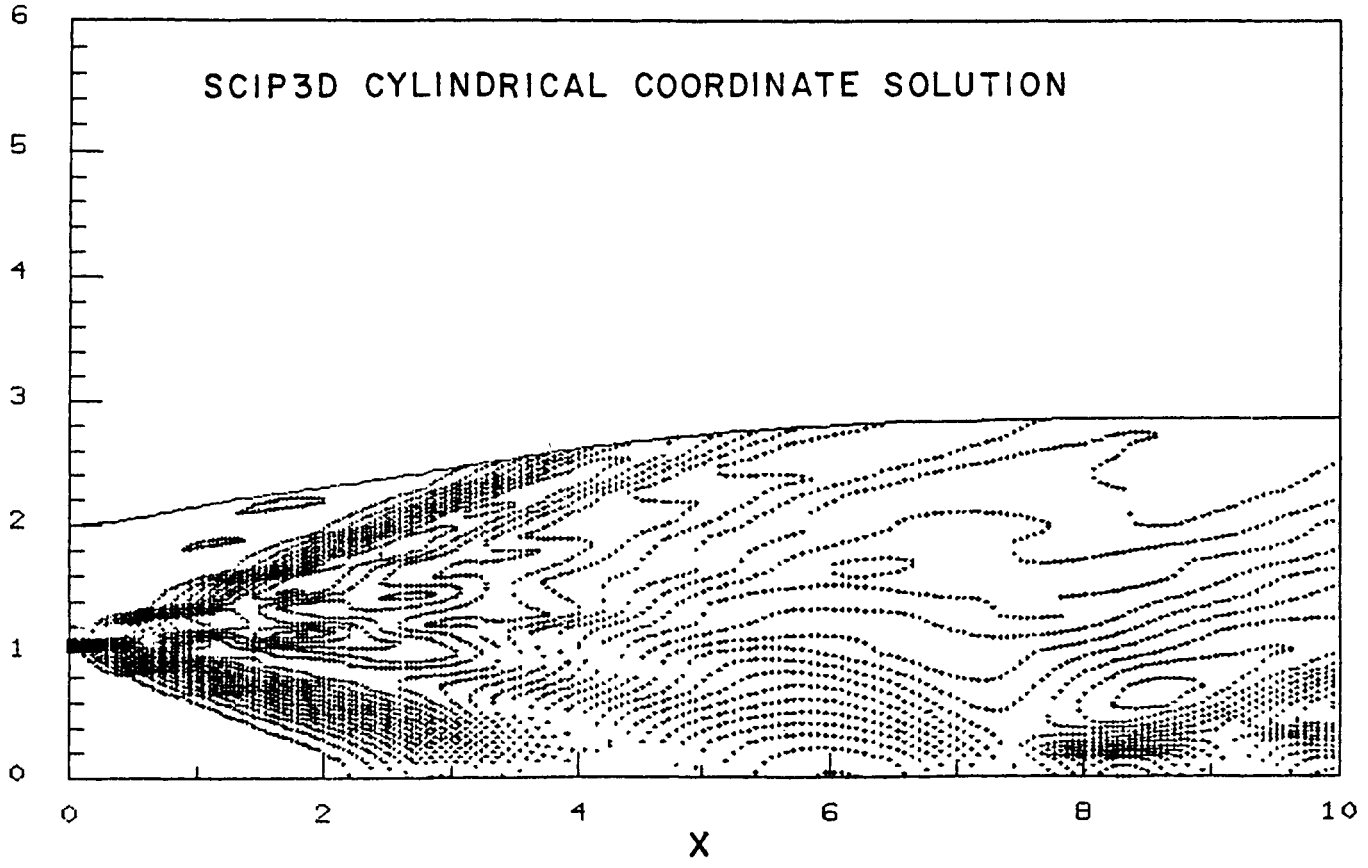

FIGURE 28. Pressure Contours In Symmetry Planes For Underexpanded Square Jet Problem, Cylindrical Solution.

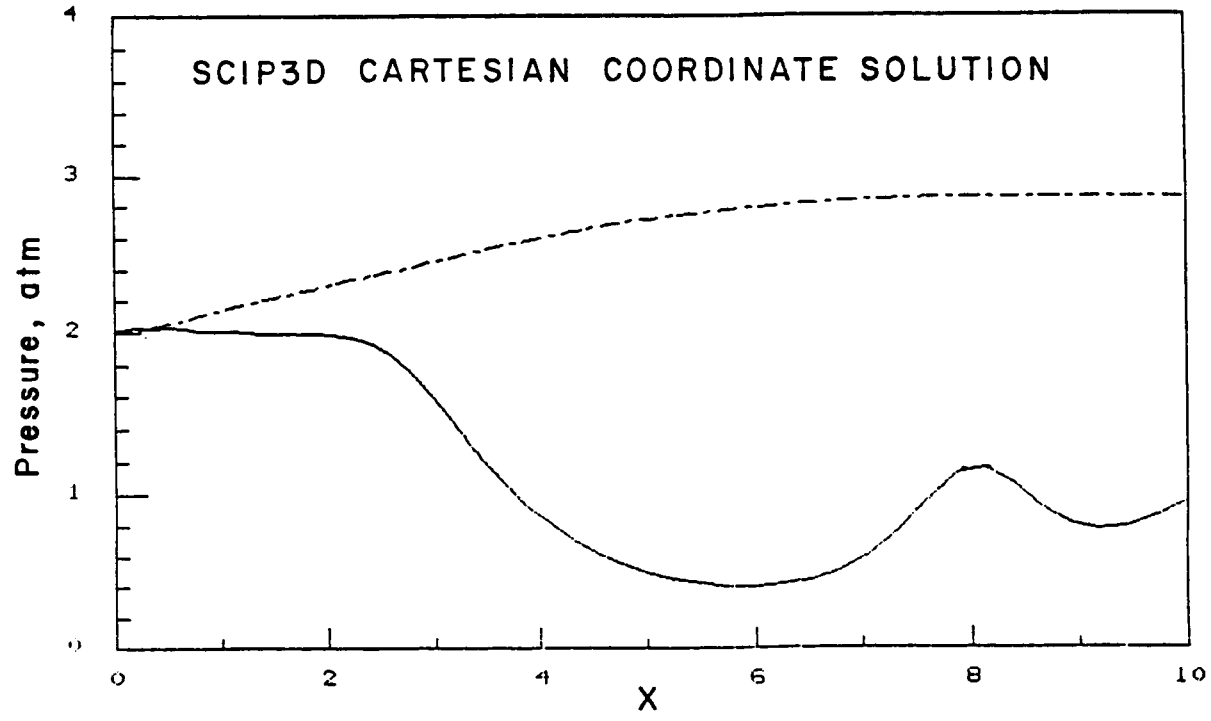

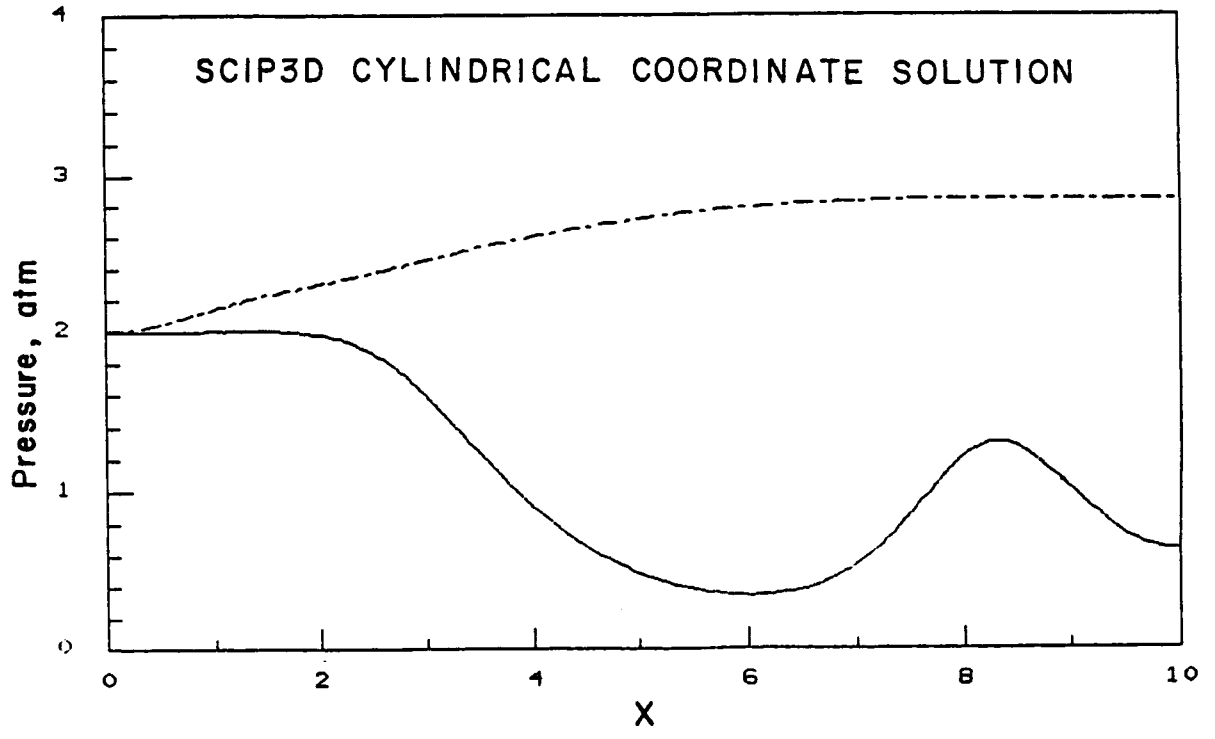

FIGURE 29. Comparison Of Centerline Pressure Variations And Jet Outer Boundary Variations For Cartesian Grid And Cylindrical Grid Solutions.

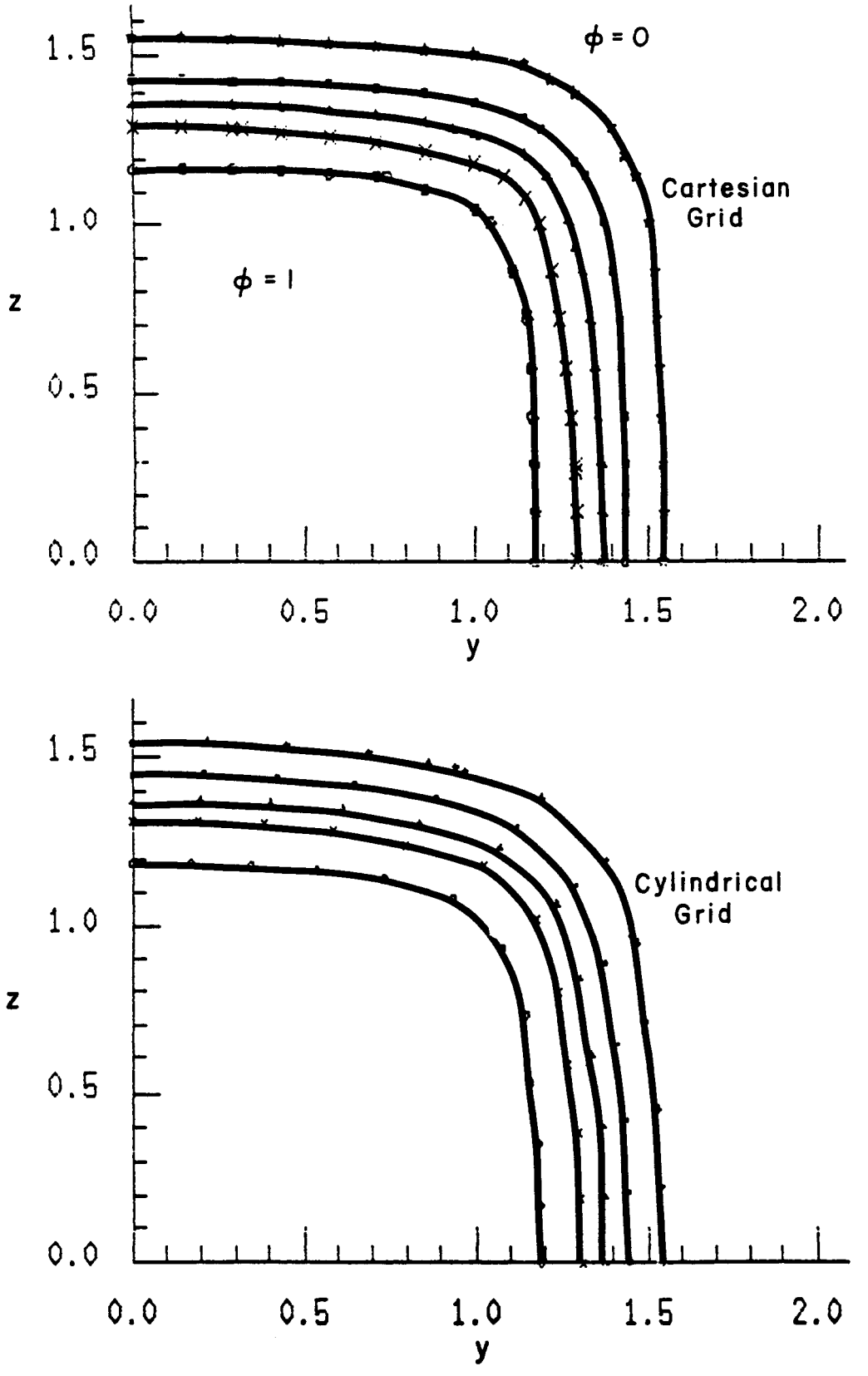

FIGURE 30. Comparison Of Cartesian Grid And Cylindrical Grid ϕ Contours At $x/r_i = 10$ (ϕ = .1, .3, .5, .7, .9 From Outer To Inner Contour).

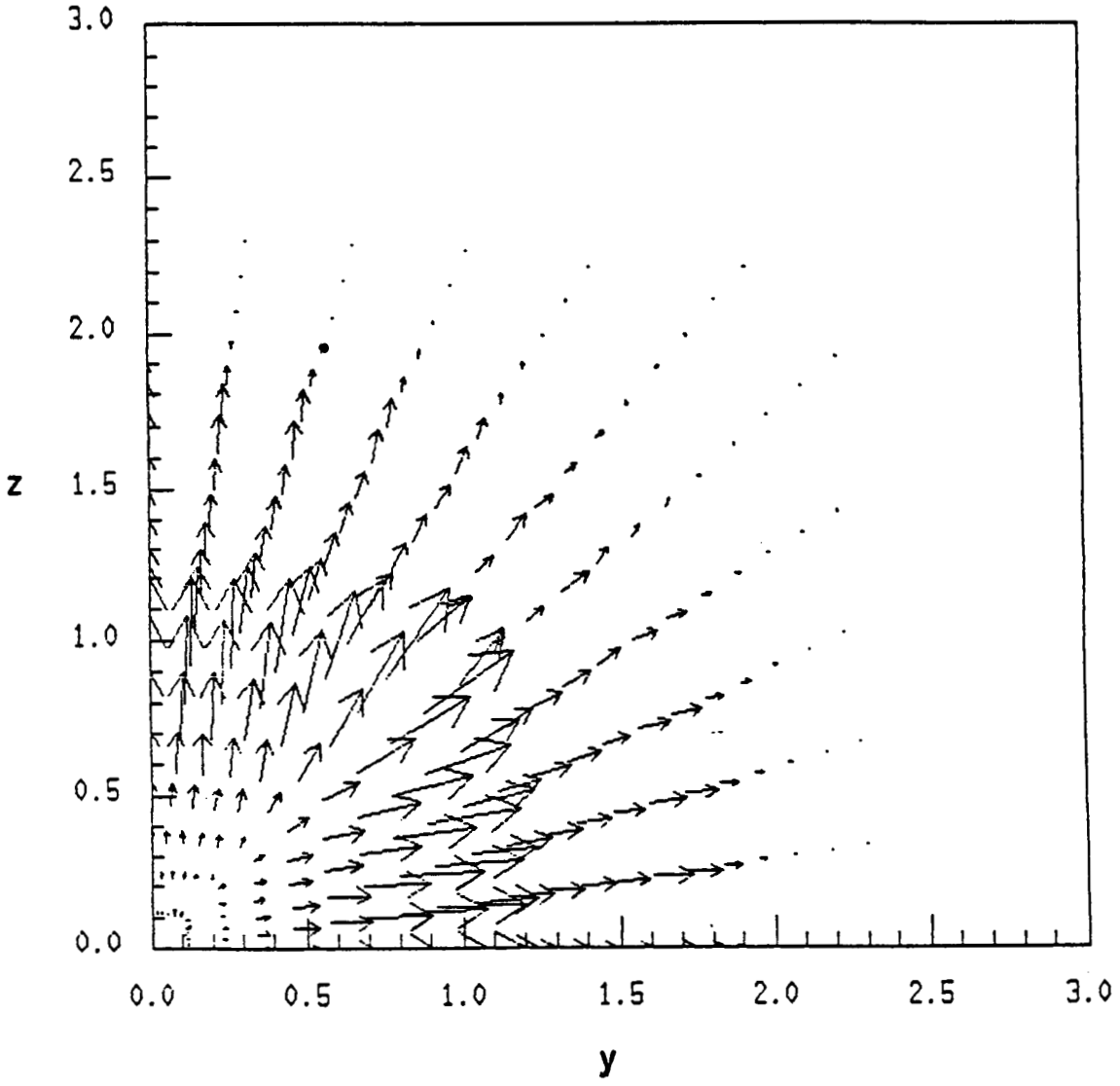

FIGURE 31A. Cross-Flow Velocity Vectors At $x/r_j = 2.$

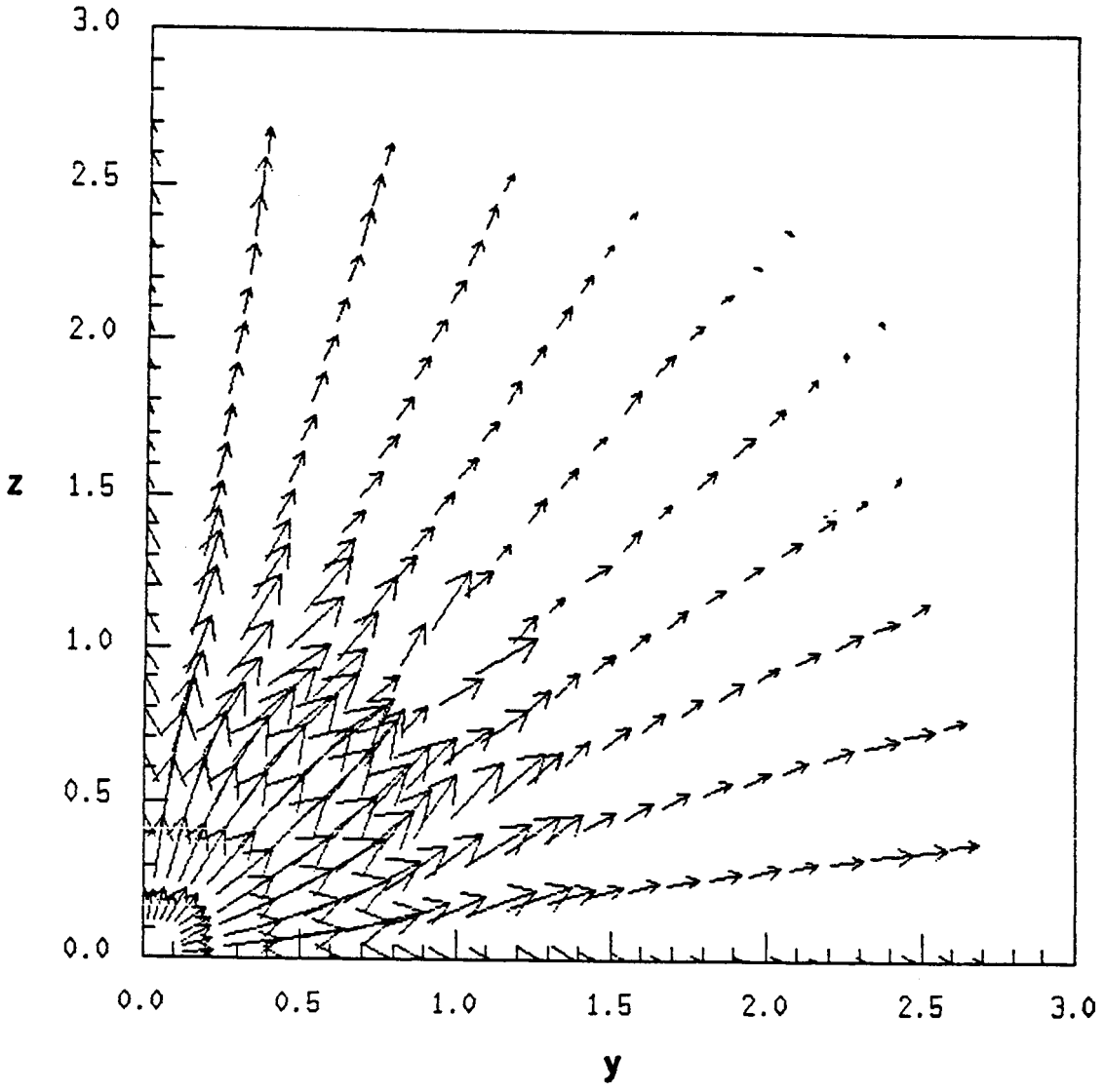

FIGURE 31B. Cross-Flow Velocity Vectors At $x/r_j = 4$.

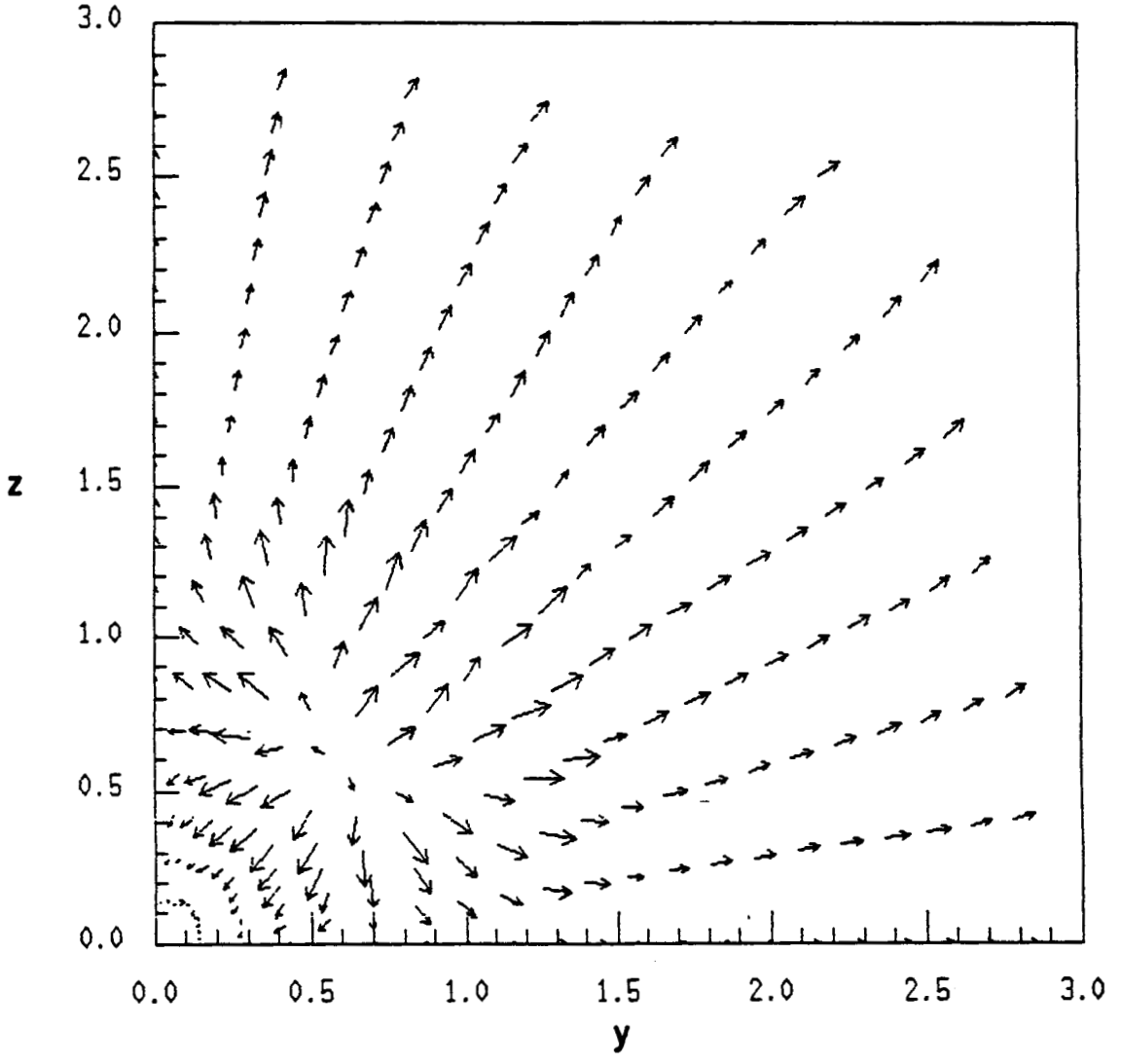

FIGURE 31C. Cross-Flow Velocity Vectors At $x/r_j = 6$.

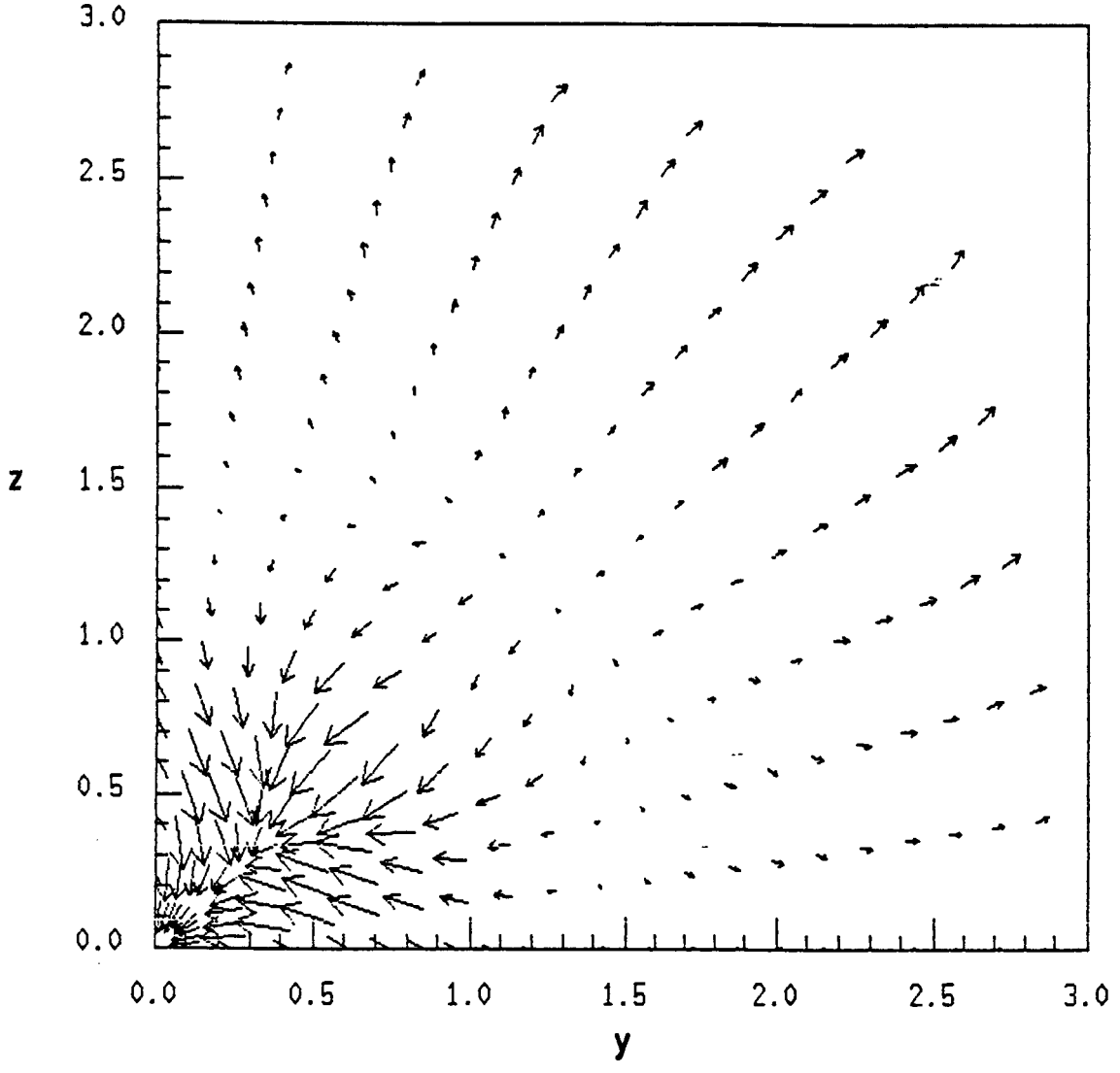

FIGURE 31D. Cross-Flow Velocity Vectors At $x/r_j = 8$.

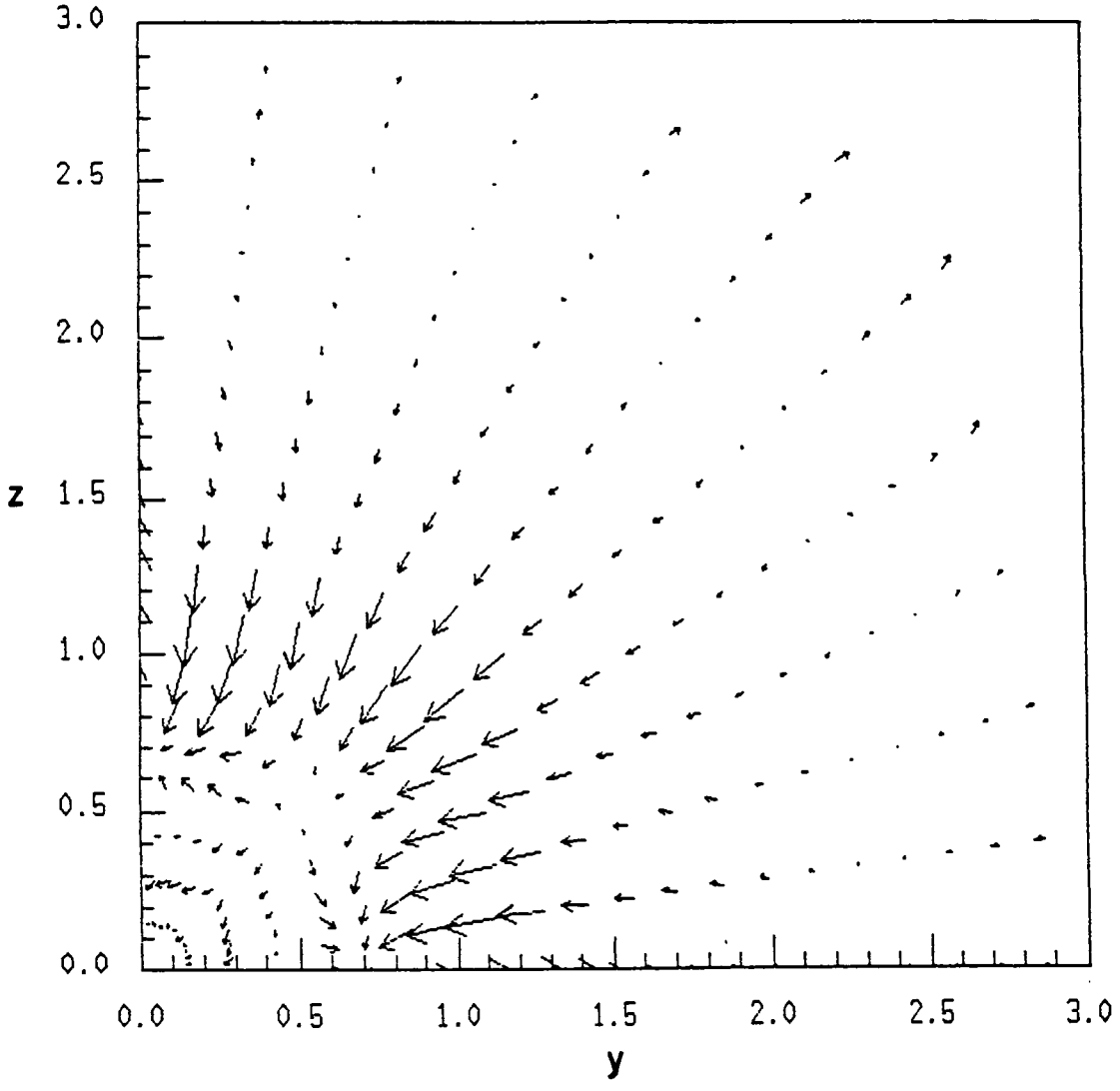

FIGURE 31E. Cross-Flow Velocity Vectors At $x/r_j = 10$.

initial 21x21 grid encompassing the domain $0 < y < 2.5$ and $0 < z < 1$. The computational boundaries $y_u(x)$ and $z_u(x)$ adapted to the growth of the jet as described in Section 2.5. The calculation was run out to $x = 120$ using the $k\varepsilon$ turbulence model. The exhaust and external flow conditions were the same as for the previous balanced-pressure square jet case, namely $M_J = 3$, $T_J = 2000$ °K and $M_E = 3$, $T_E = 500$ °K.

The nearfield structure of the rectangular jet flow is exhibited by the contours of the velocity, U; the species parameter, ϕ; the temperature, T; and, the turbulent kinetic energy, k; in the symmetry planes $y = 0$ and $z = 0$ as exhibited in Figure 32-35. Cross-flow contours of ϕ at $x = 5$, 10, 20 and 40 (Figure 36) show the nearfield shape change from a rectangular to an elliptical cross-section. Cross-flow contours of k at = 10, 20 and 30 (Figure 37) show peak values of turbulence to be off-axis and initially dominated by the stronger mixing in the vertical (z) direction.

The overall jet structure (nearfield/farfield) is exhibited in the ϕ symmetry plane contours of Figure 38 for $0 < x < 120$, and, the ϕ cross-flow contours at $x = 60$, 80 and 100 (Figure 39). The centerline variations of ϕ, T, and k for $0 < x < 120$ are exhibited in Figures 40 - 42.

3.9 Underexpanded 4/1 Aspect Ratio Rectangular Jet Problem

The above problem was repeated with the jet pressure boosted to 2 atm, and all other conditions remaining the same. The pressure contours in the two symmetry planes ($y = 0$ and $z = 0$) are exhibited in Figure 43 with the shear layer ($.1 < \phi < .0$) superimposed. Jet contours ($\phi = .1$) at $x = 0$, 10, 20 and 40 (Figure 44) exhibit a gradual transition towards an elliptical cross section, with the 'effective' aspect ratio at $x = 40$ (y_{MAX}/z_{MAX}) reduced from 4/1 to 2.3/1. The bulges due to wave/shear layer interactions are quite pronounced at $x = 10$ and 20. Note that the ϕ contours at $x = 10$ and 20 nearly coincide since the jet has fully expanded at $x = 10$ and then recompresses in going from 10 to 20. The predicted pressure variation along the jet axis of symmetry is exhibited in Figure 45.

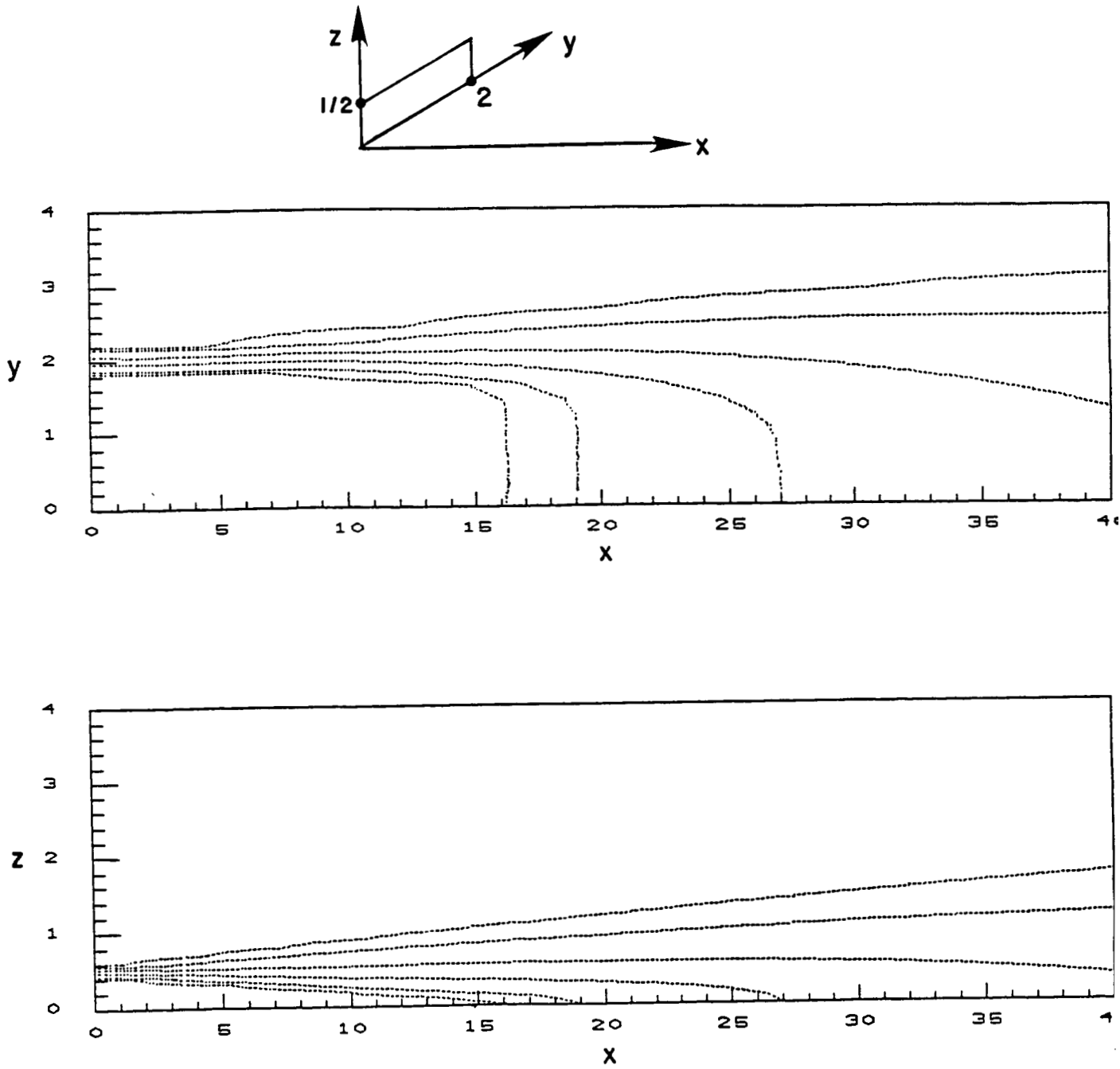

FIGURE 32. U Contours For 4/1 Balanced Pressure Mixing Problem In Symmetry Planes.

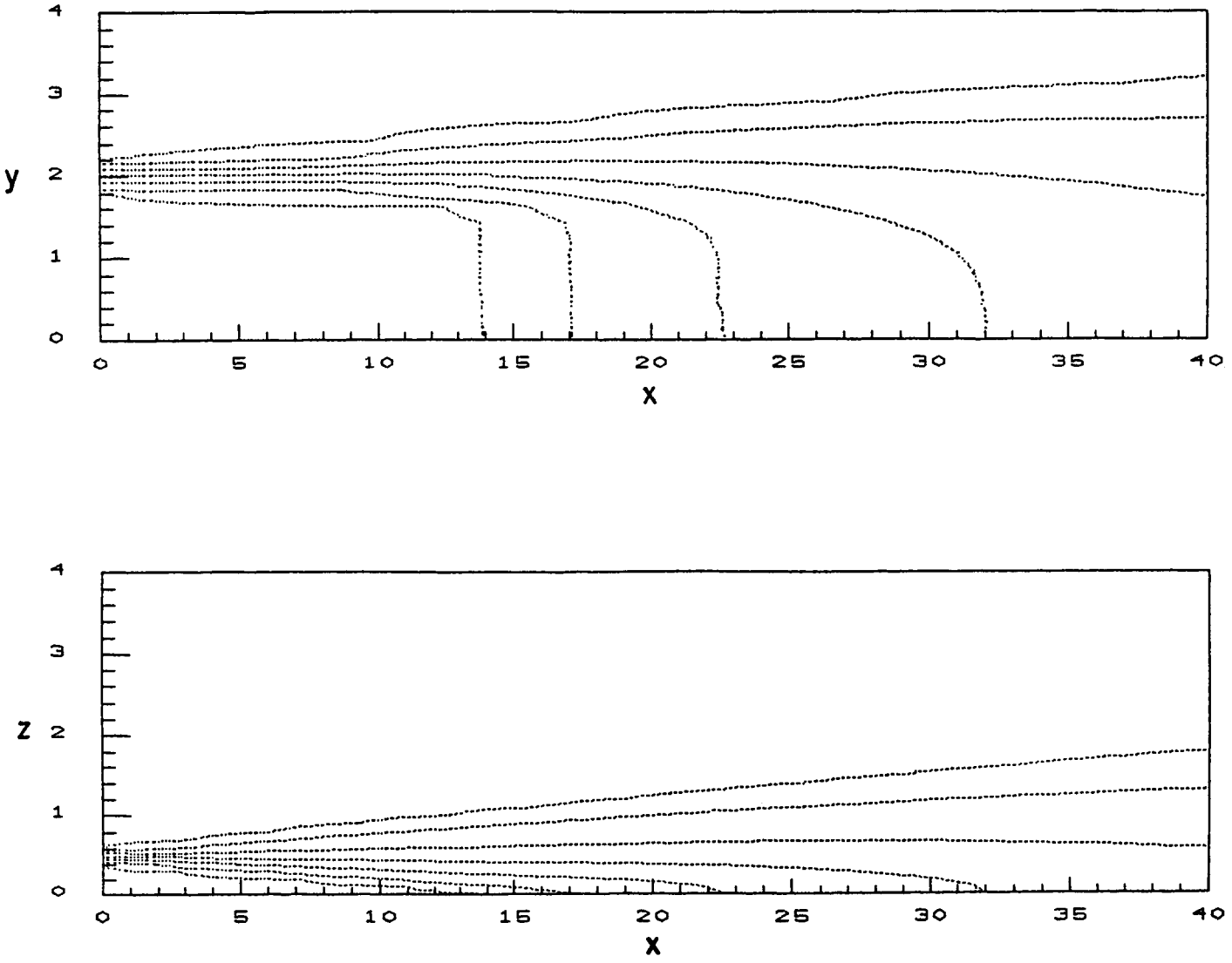

FIGURE 33. ϕ Contours For 4/1 Balanced Pressure Mixing Problem In Symmetry Planes.

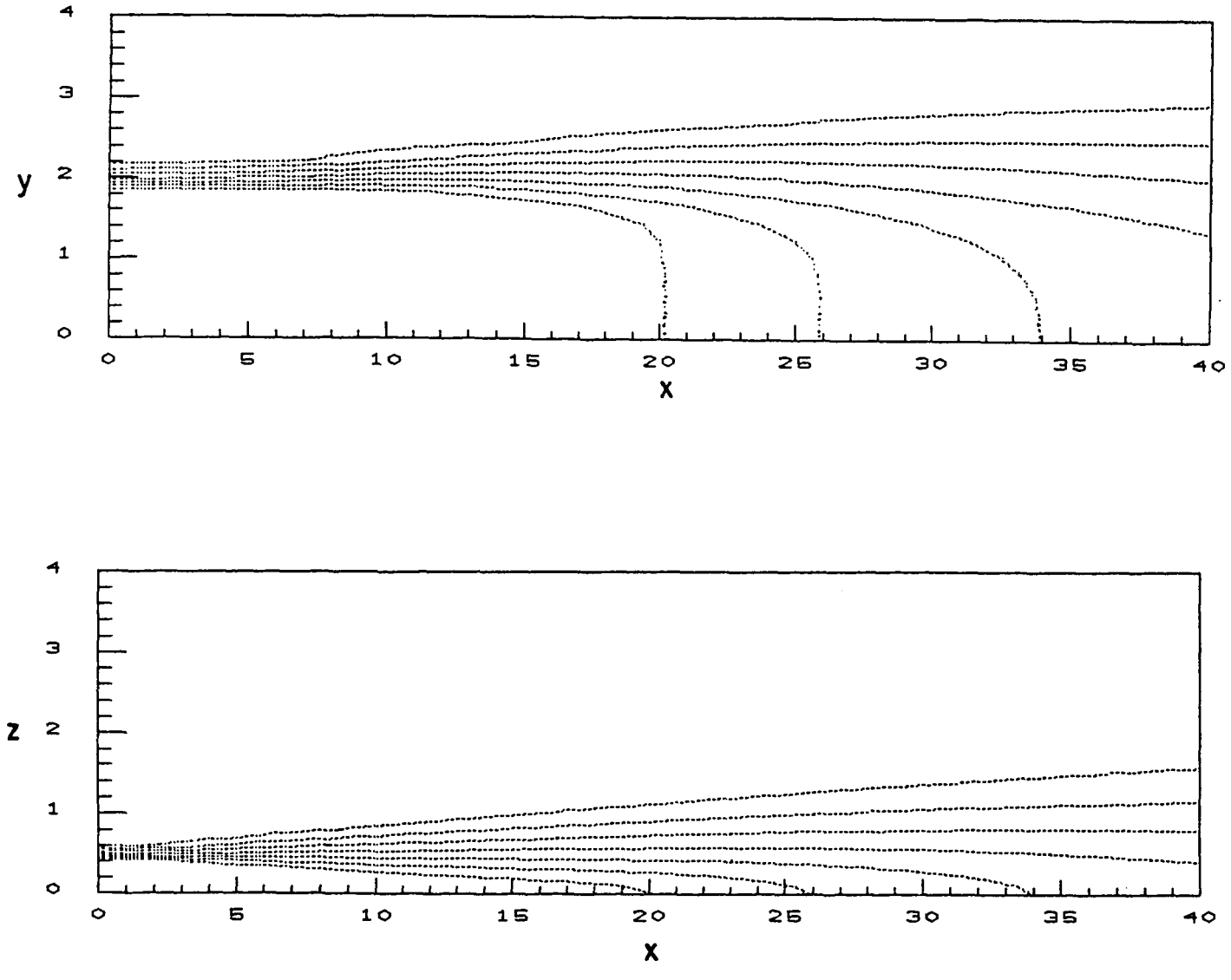

FIGURE 34. T Contours For 4/1 Balanced Pressure Mixing Problem In Symmetry Planes.

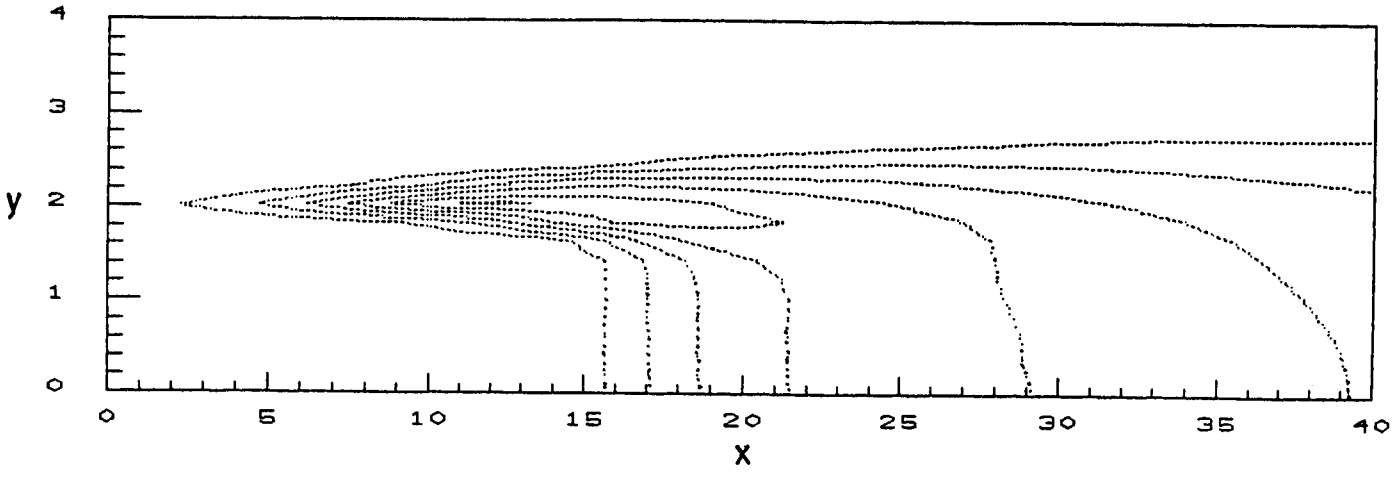

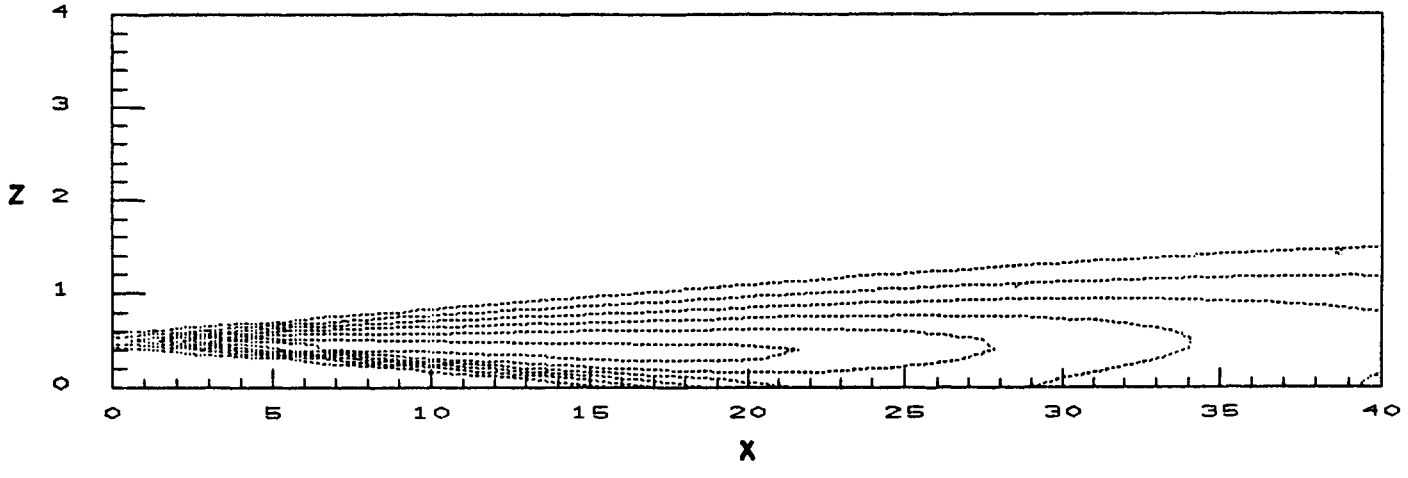

FIGURE 35. K Contours For 4/1 Balanced Pressure Mixing Problem In Symmetry Planes.

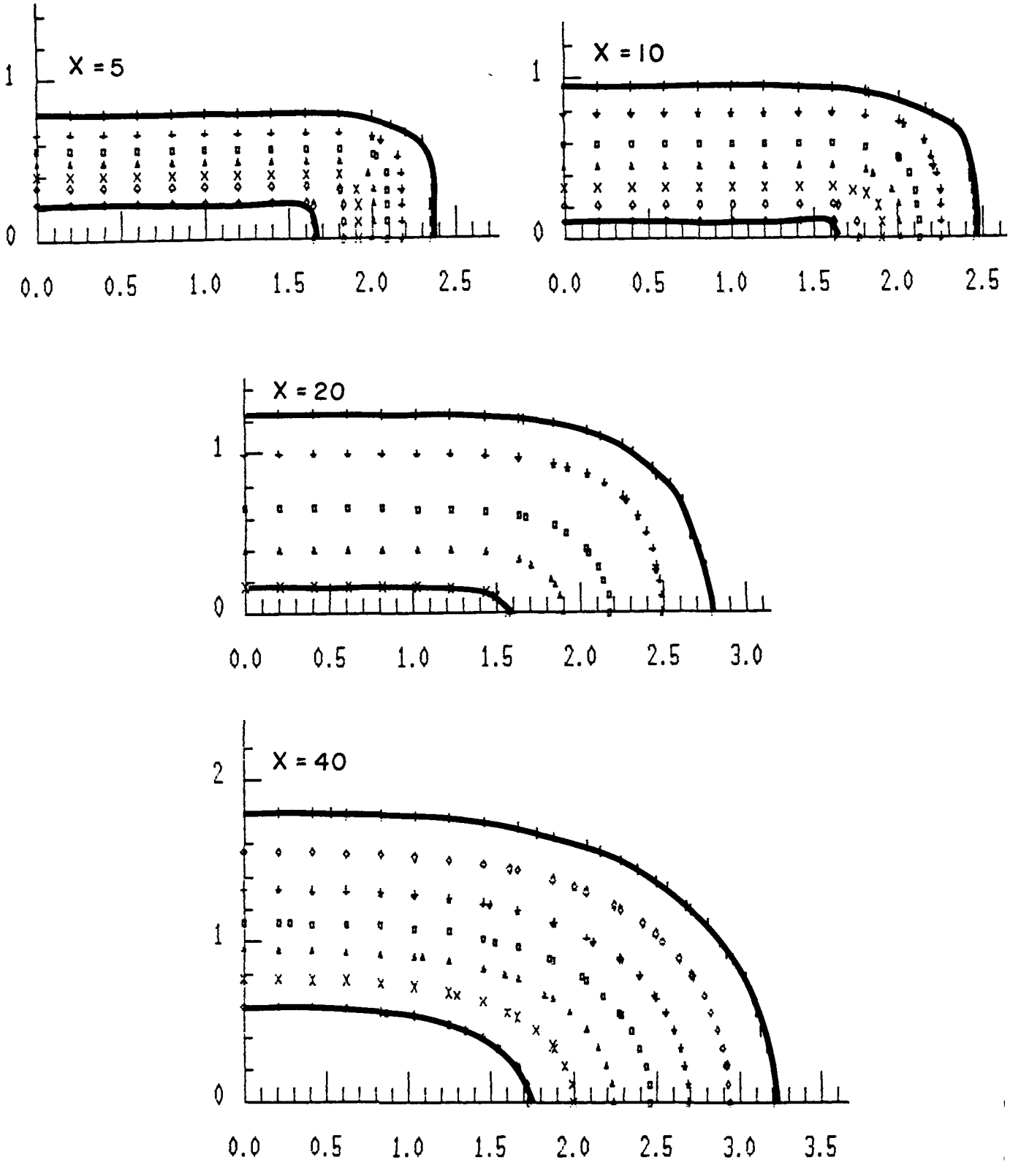

FIGURE 36. Cross-Flow Contours Of ϕ For 4/1 Balanced Pressure Rectangular Jet Case.

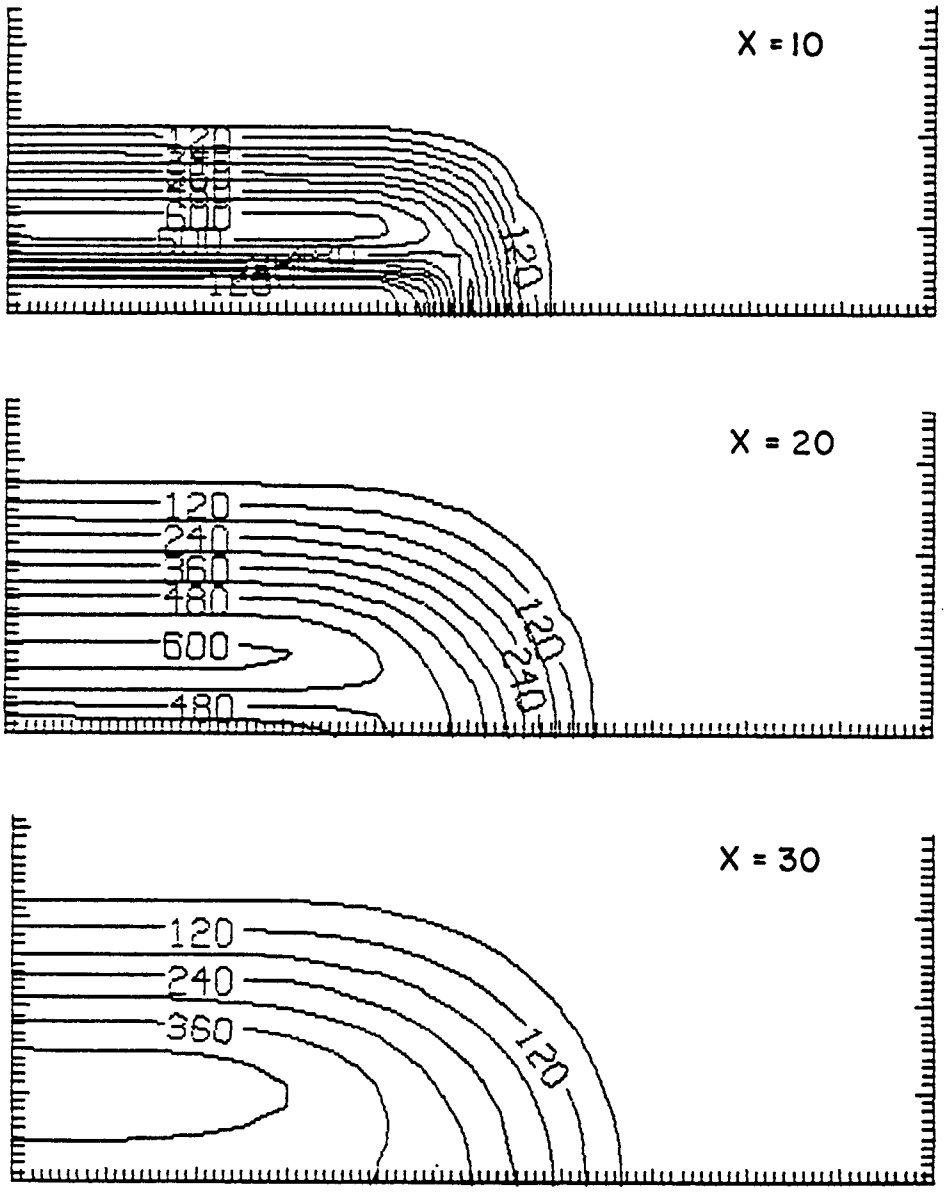

FIGURE 37. Cross-Flow Contours Of K For 4/1 Balanced Pressure Rectangular Jet Case.

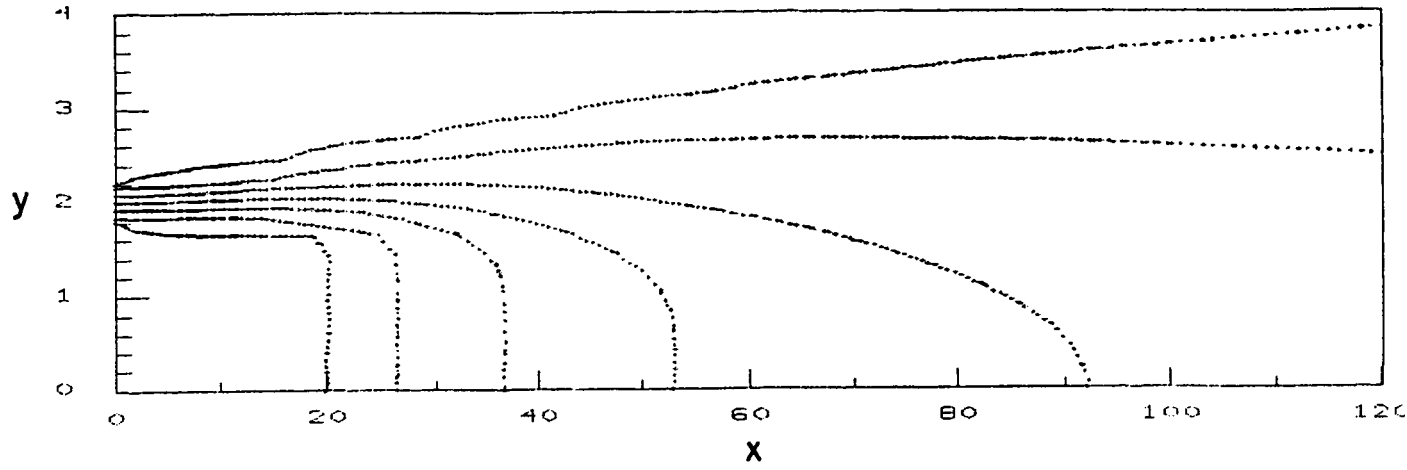

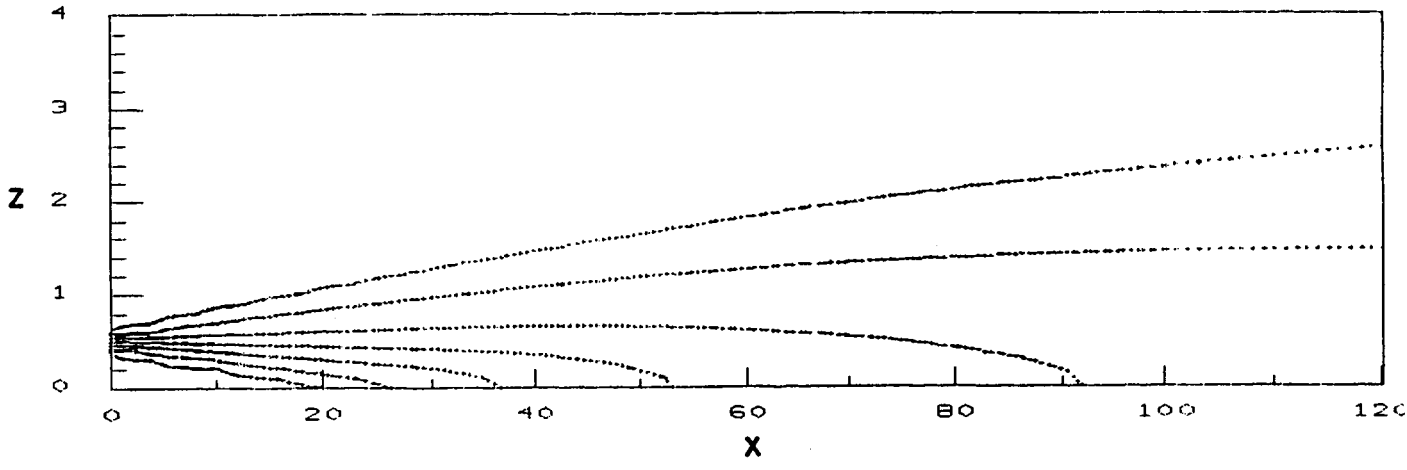

FIGURE 38. Overall Jet Structure In Symmetry Planes As Exhibited By ϕ Contours For 4/1 Balanced Pressure Case.

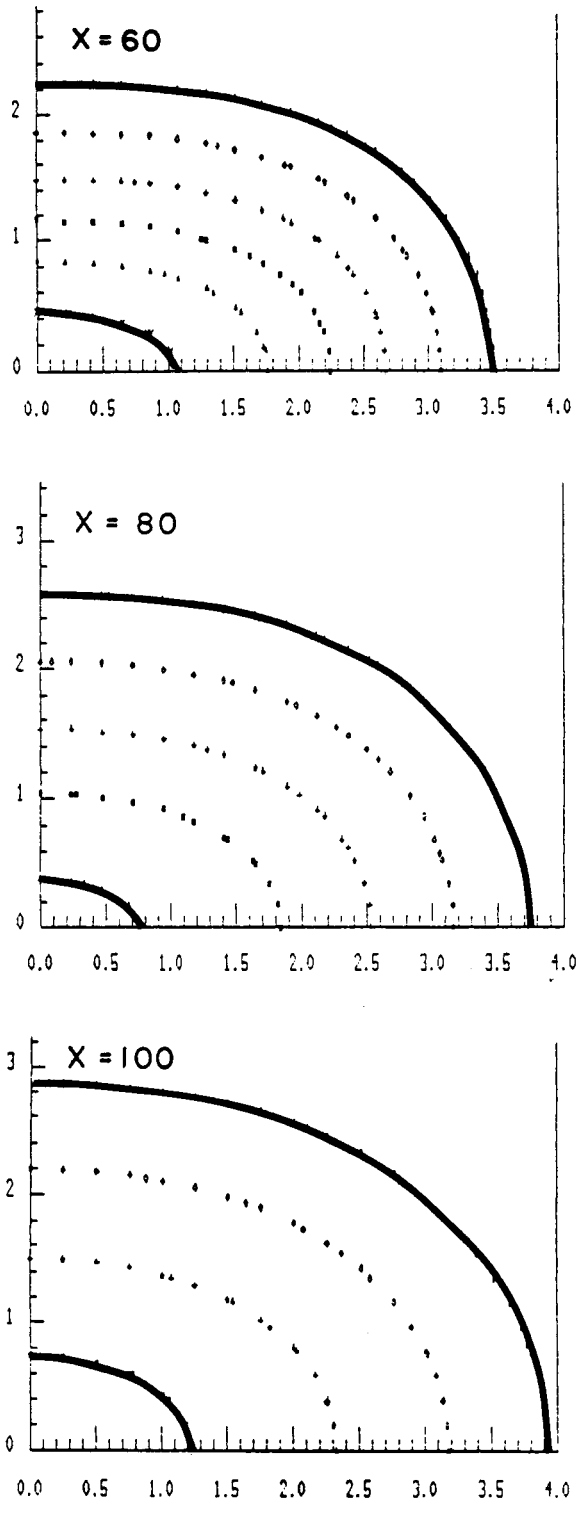

FIGURE 39. ϕ Contours In Cross-Flow Plane At x = 60, 80, And 100 For 4/1 Balanced Pressure Case.

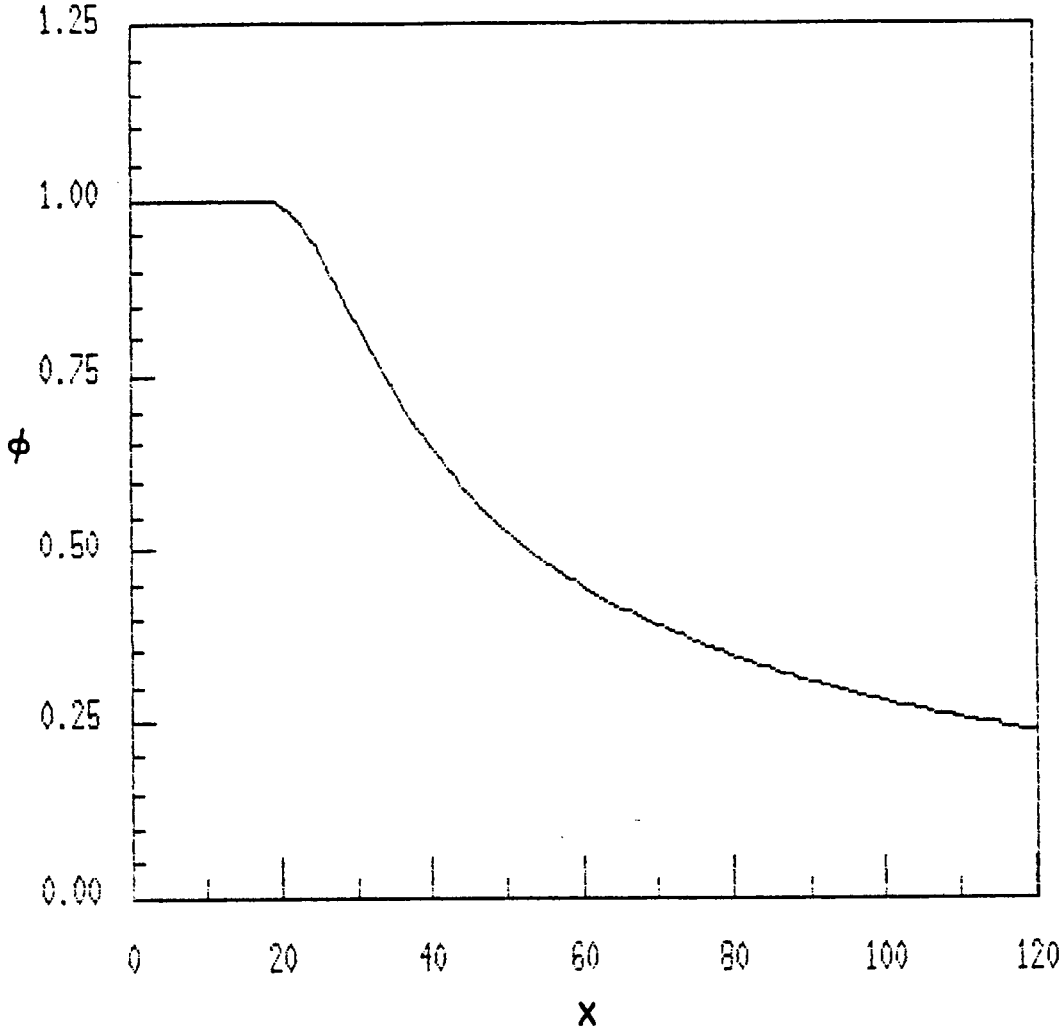

FIGURE 40. Centerline Variation Of ϕ; 4/1 Balanced Pressure Case.

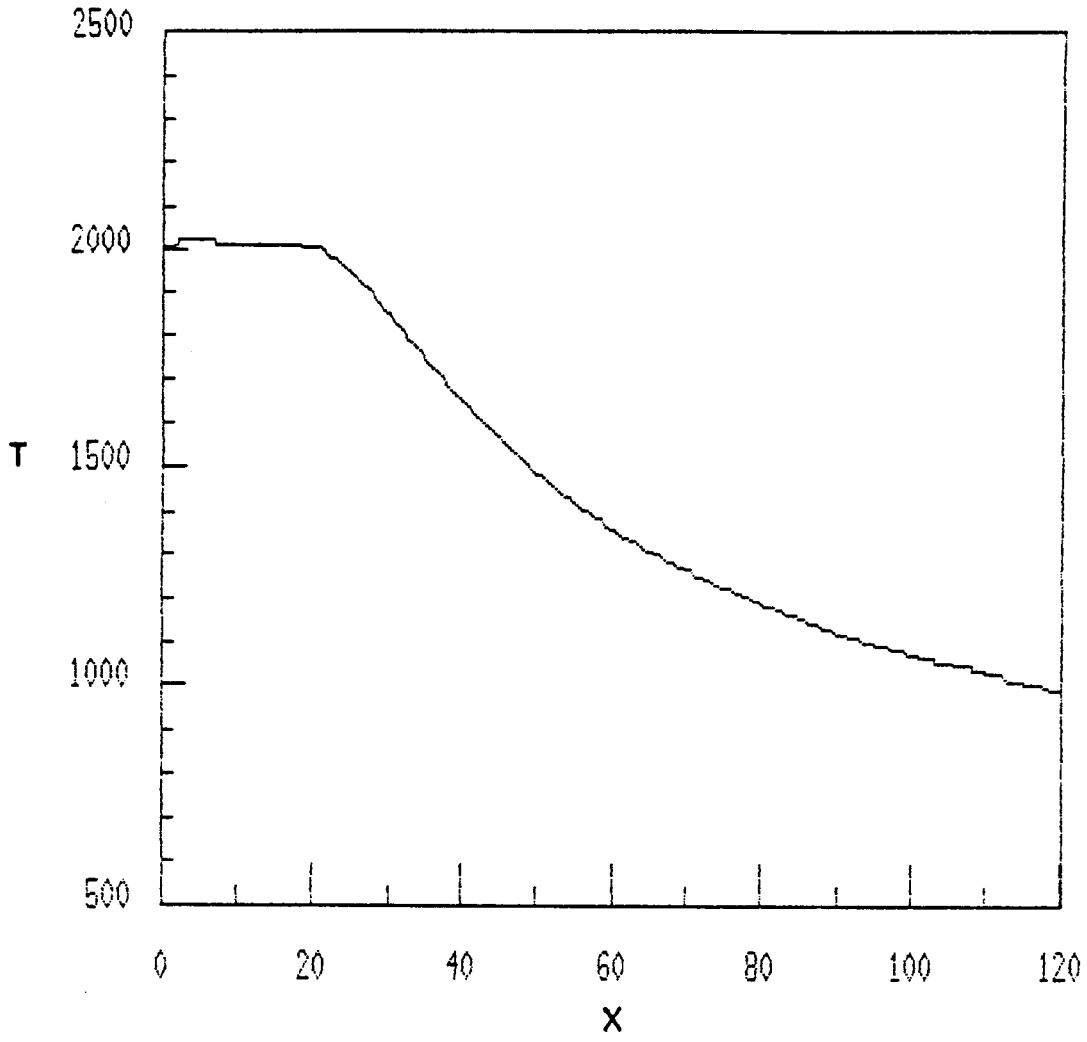

FIGURE 41. Centerline Variation Of T; 4/1 Balanced Pressure Case.

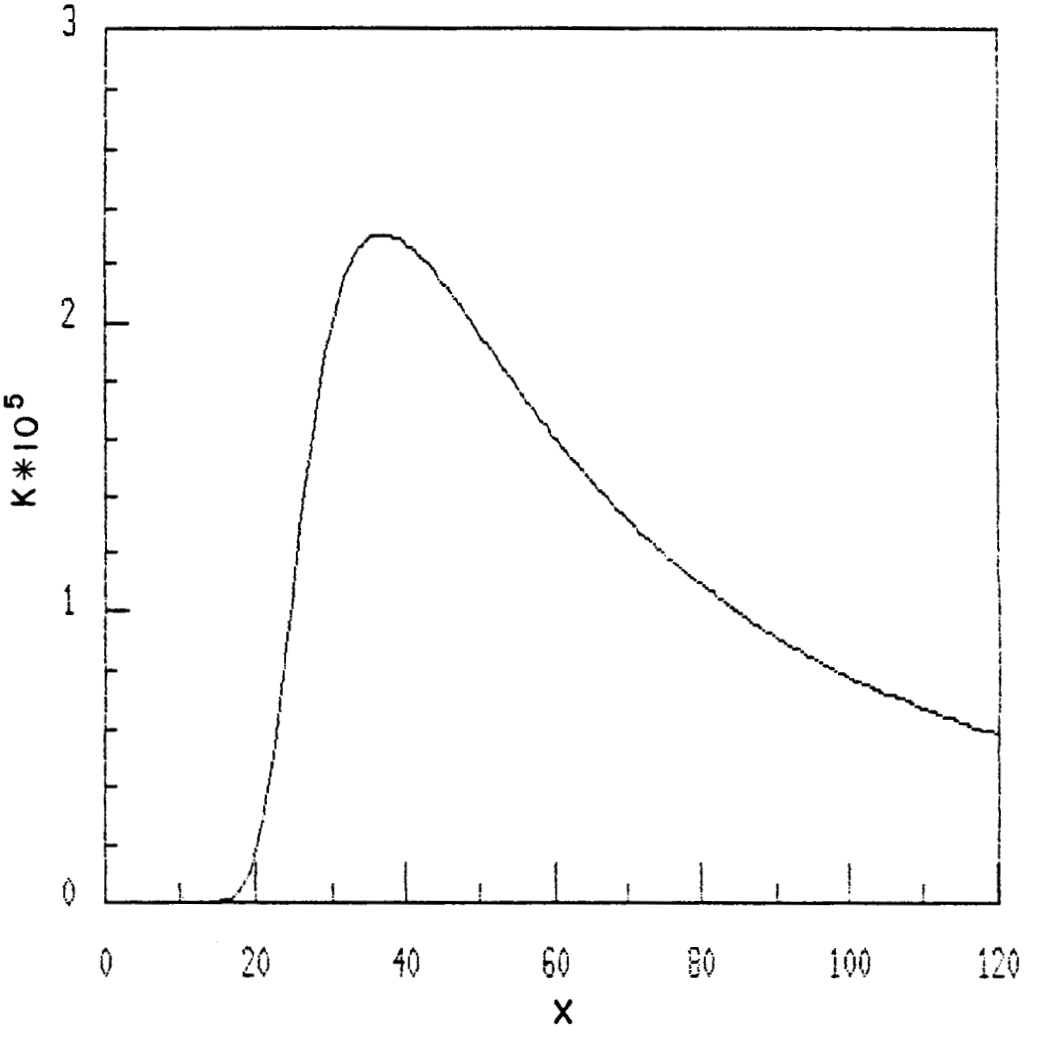

FIGURE 42. Centerline Variation Of K; 4/1 Balanced Pressure Case.

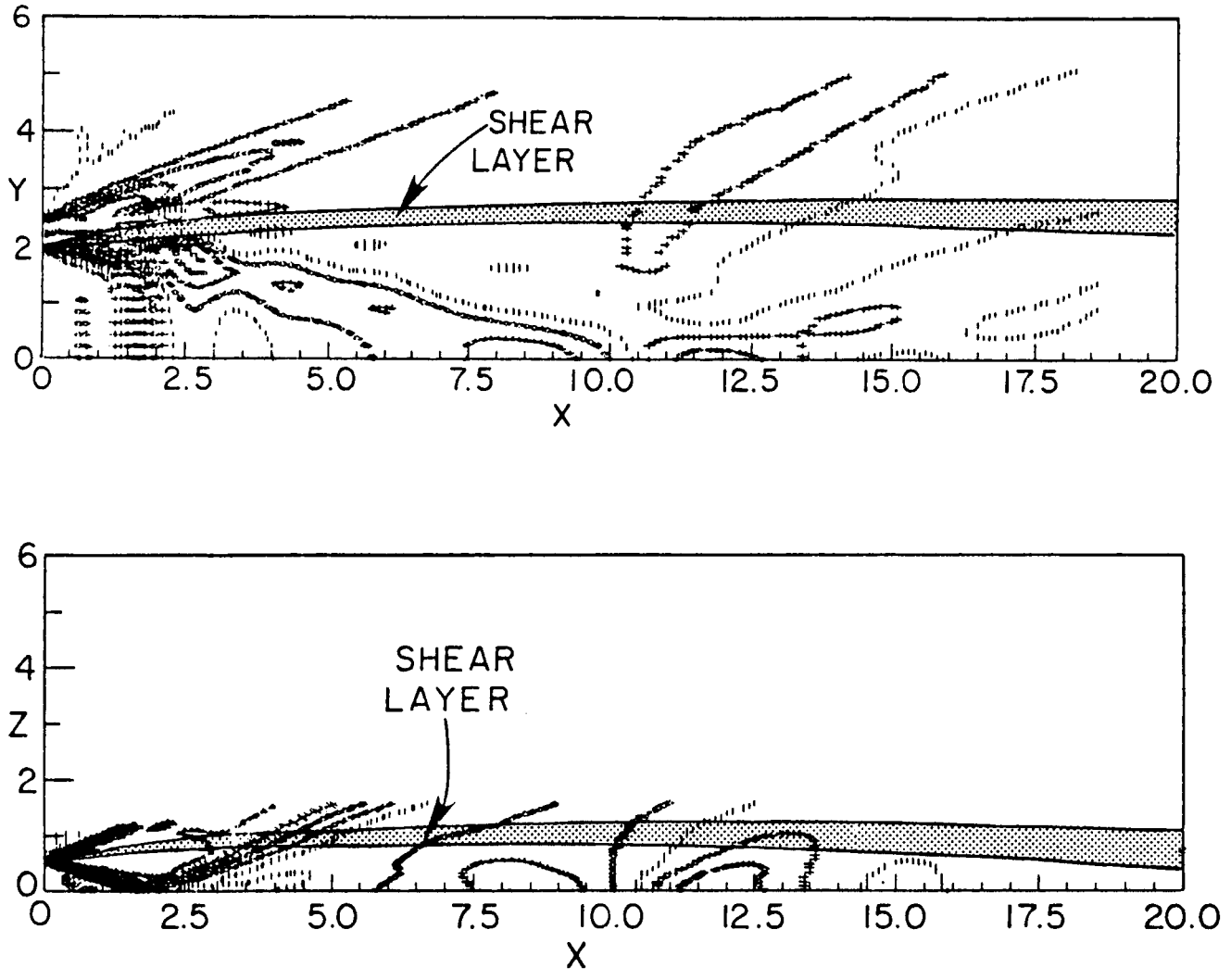

FIGURE 43. Pressure Contours In Symmetry Planes For 4/1 Underexpanded Case.

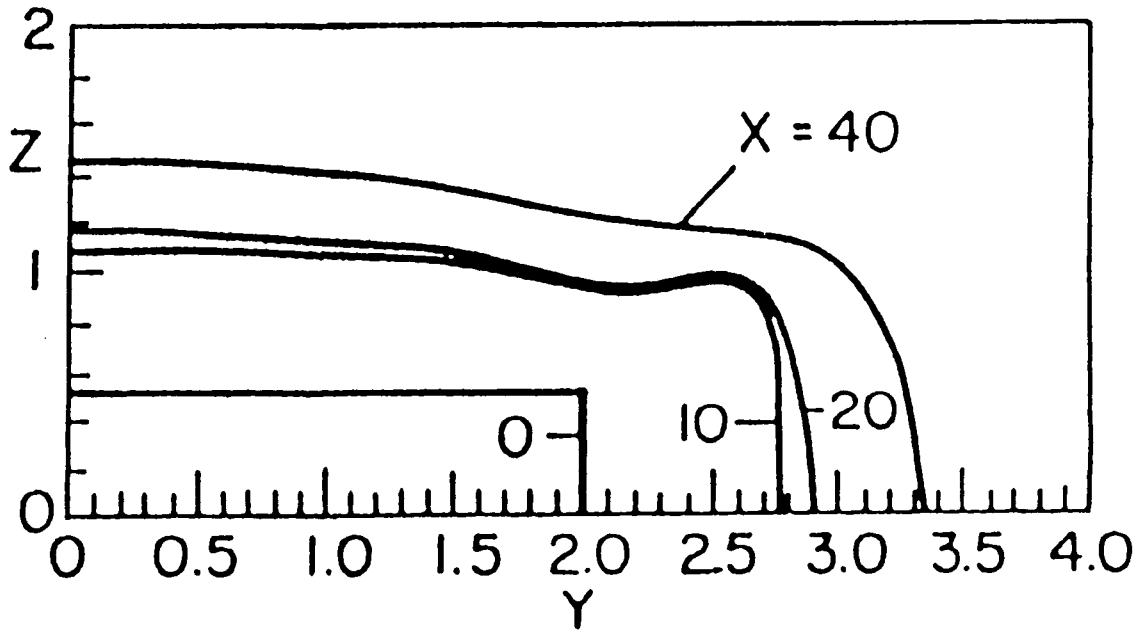

FIGURE 44. Jet Cross-Flow Contours For Rectangular Underexpanded Jet ($P_J/P_E = 2$).

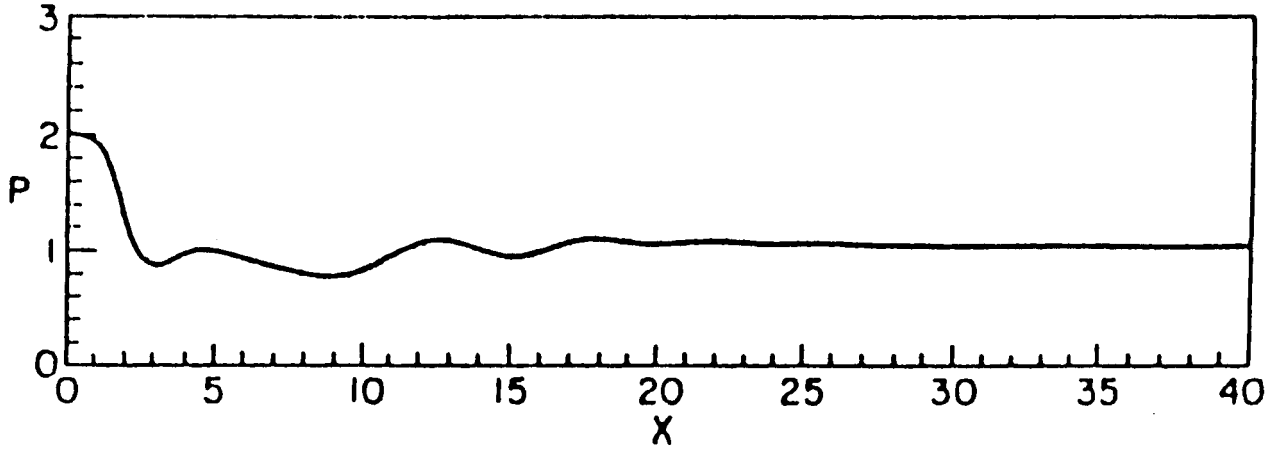

FIGURE 45. Pressure Variation Along Jet Axis; Underexpanded Rectangular Jet.

3.10 Multiple Underexpanded Square Jet Problem

A calculation analogous to that of the underexpanded square jet problem (Section 3.7) was performed for an infinite array of square underexpanded jets as exhibited in Figure 46. The jets are initially 2x2 and their axes of symmetry have a spacing of 4. The lower portion of Figure 46 exhibits a schematic of the predicted shear layer growth and shock pattern for $0 < x < 40$ in the symmetry plane $z = 0$. The calculation was performed utilizing symmetry conditions on the planes $z = 0$, $y = 0$ and $y = 2$. The predicted pressure contours and ϕ contours in the plane $z = 0$ are exhibited in Figure 47. The flow is characterized by jet-induced bow shocks traversing the flow in the spanwise direction as readily evidenced by the pressure contours of Figure 47. The species contours expand/contract in accordance with the passage of the shock waves. The individual mixing regions coincide at $x \sim 35$ as indicated by the coalescence of the outer ϕ contours. ϕ contours at the axial stations $x = 0, 10, \ldots, 60$ (Figure 48) exhibit the growth history of the individual jets and their interaction for $x > 35$, with pronounced wave interactions producing the corner region bulges in the early growth stage ($0 < x < 20$). The mixing characteristics in the symmetry planes $z = 0$ (TOP VIEW) and $y = 0$ (SIDE VIEW) are exhibited by the velocity and turbulent kinetic energy profiles at $x = 0, 10, \ldots, 60$ provided in Figure 49.

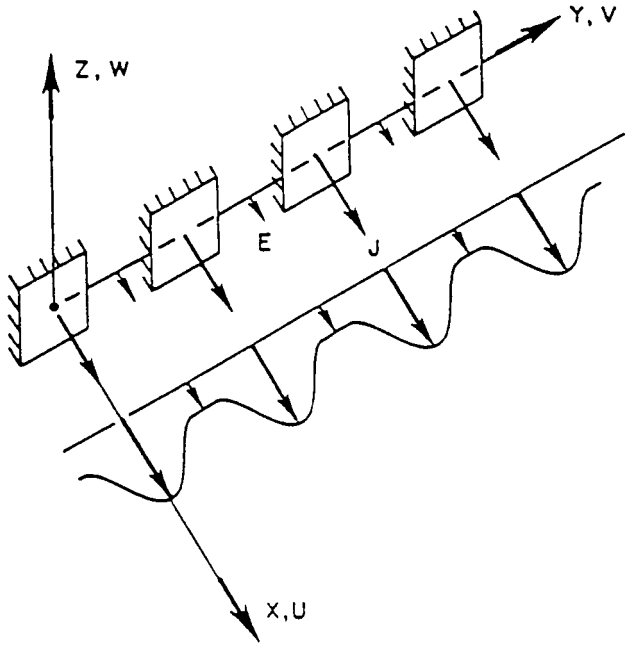

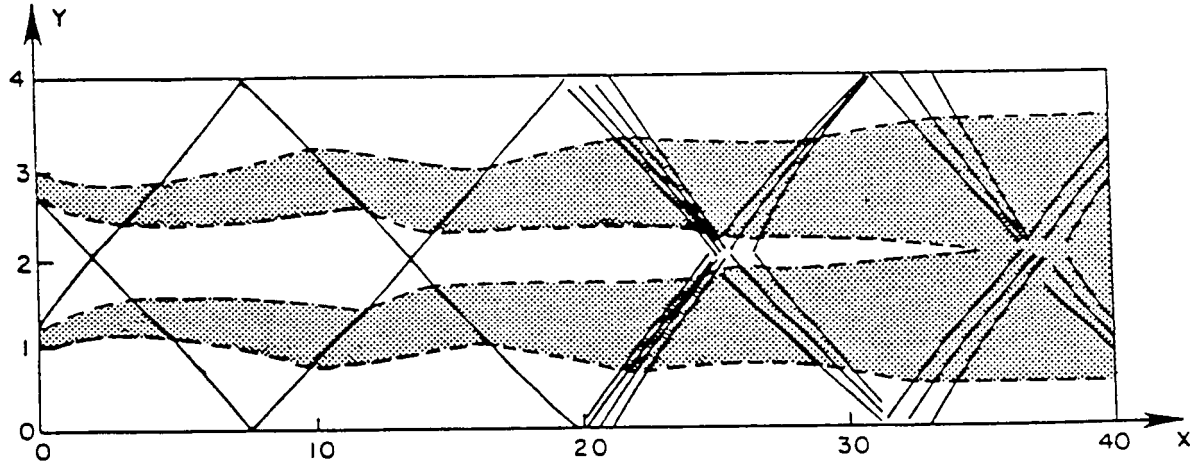

FIGURE 46. Schematic Of Multiple Square Jet Problem And Shock/Shear Layer Pattern In z = 0 Symmetry Plane.

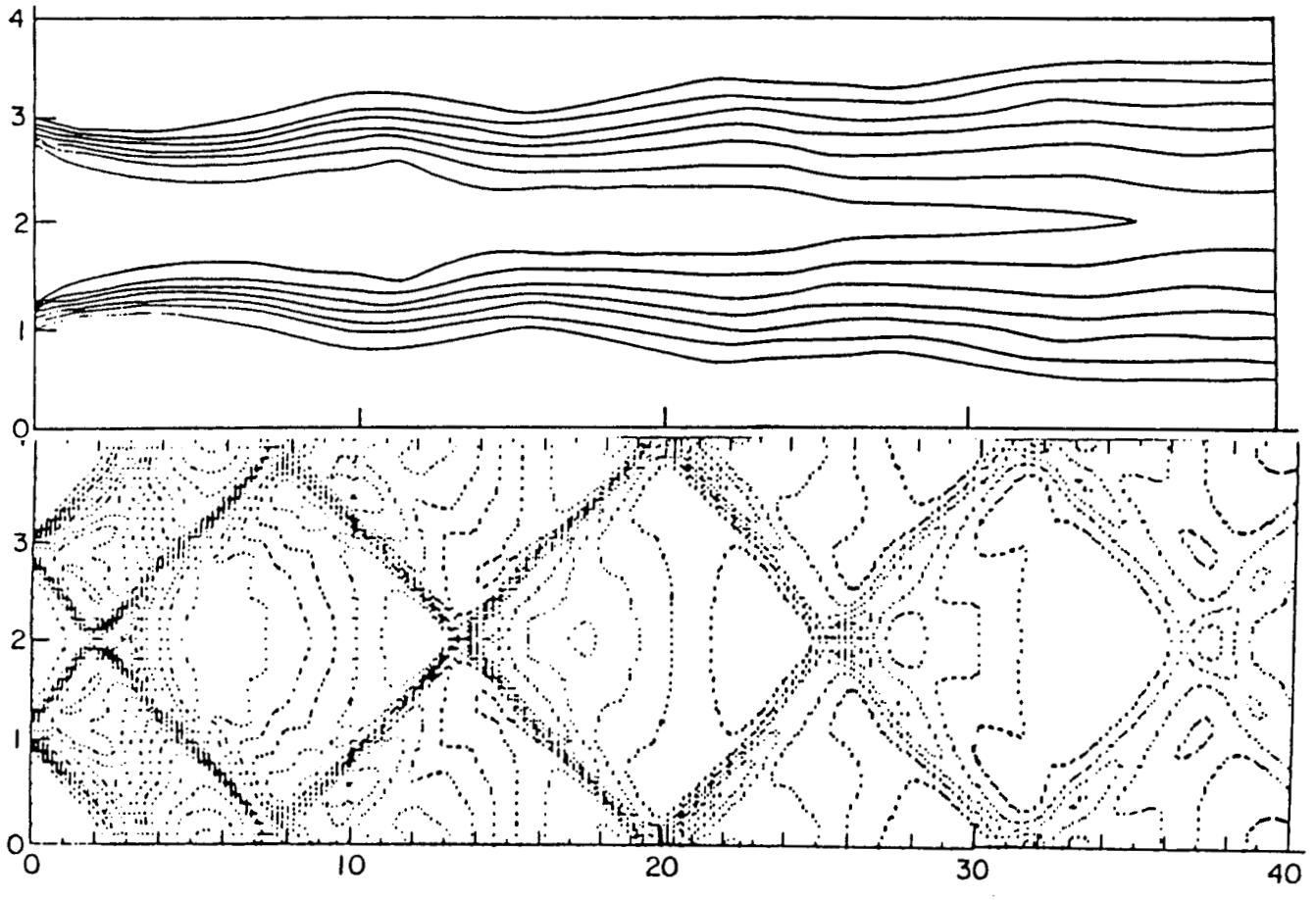

FIGURE 47. ϕ and P Contours In z = 0 Symmetry Plane For Multiple Square Jet Problem.

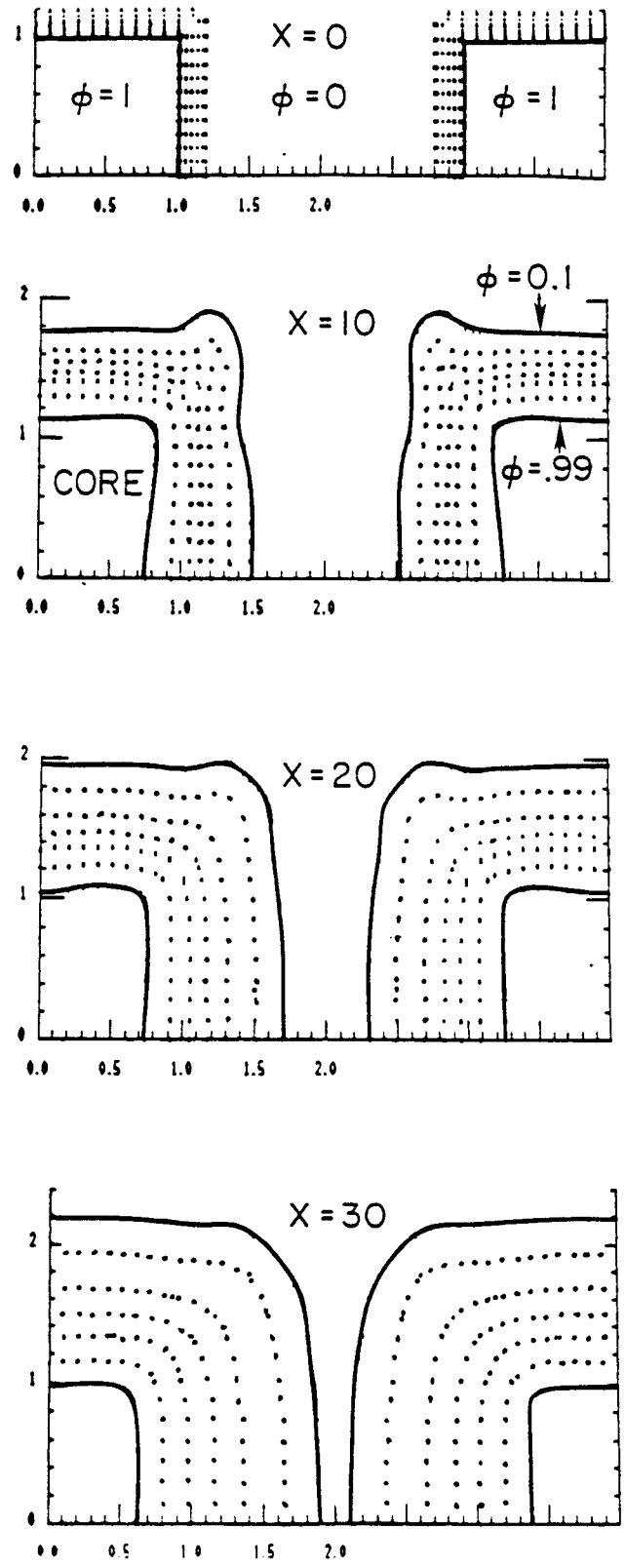

FIGURE 48. ϕ Cross-Flow Contours For Multiple Square Jet Problem.

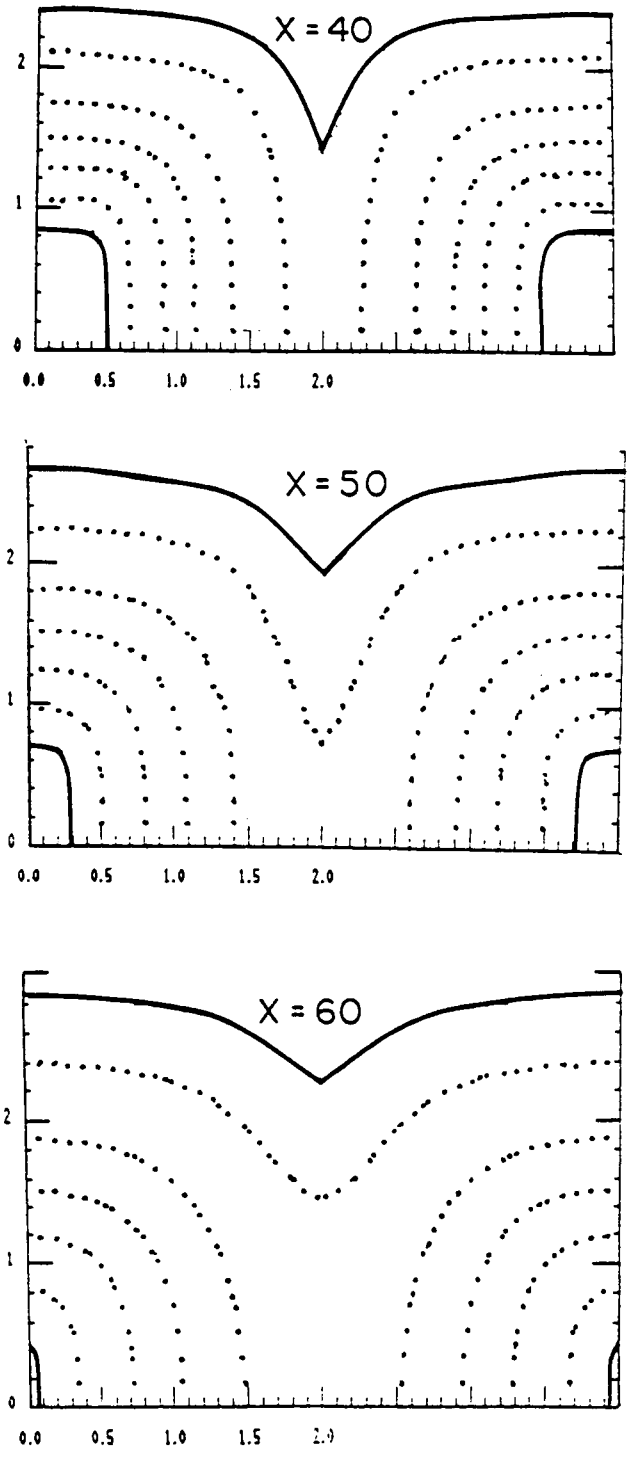

FIGURE 48 (CONT'D). 6 Cross-Flow Contours For Multiple Square Jet Problem.

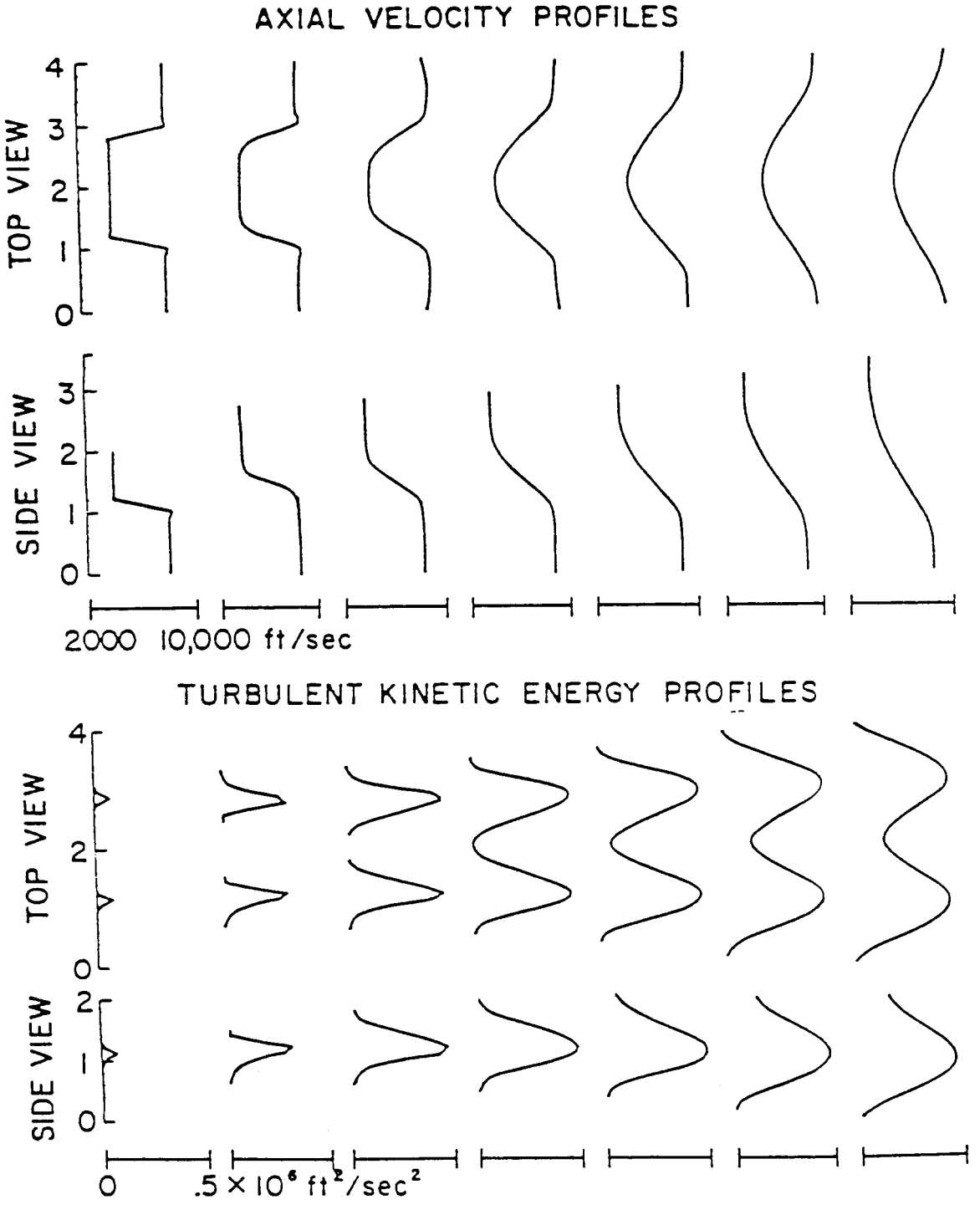

FIGURE 49. Axial Velocity And Turbulent Kinetic Energy Profiles For Multiple Jet Problem.

4. NUMERICAL PROCEDURES FOR ANALYZING SUBSONIC MIXING PROBLEMS AND NUMERICAL STUDIES

4.1 Overview of Pressure-Split PNS Subsonic Marching Approach

One of the most popular procedures for the analysis of 3D subsonic mixing problems has been the SIMPLE procedure of Patankar and Spalding[38]. Numerous codes have been developed based on this procedure for both free and ducted jet mixing problems. In the SIMPLE procedure, the flow solution is obtained by a stepwise parabolic marching integration combined with a quasi-elliptic cross-flow integration. To permit spatial marching, the pressure field is split with the streamwise component imposed (or arrived at from global continuity constraints for ducted flows) and the cross-flow variation arrived at from the coupled solution of the continuity and cross-flow momentum equations.

The SIMPLE procedure utilizes an iterative cross-flow integration approach whereby:

(1) the cross-flow momentum equations are independently solved to yield the cross-flow velocities, V and W; and,

(2) a pressure correction equation arrived at from continuity with 'partial' cross-flow momentum coupling is used to upgrade the pressure field.

Steps (1) and (2) are iterated upon until a converged cross-flow solution is obtained. This iterative cross-flow procedure is not always stable and according to Carroll[39], **'most of the instabilities are caused by the coupling between the equations'**. To reduced these instabilities, significant underrelaxation is required between the iterative sweeps. In addition, in complex regions such as the initial corner regions of rectangular jets, convergence problems occur which sometimes cannot be remedied by underrelaxation.

In analyzing 2D subsonic mixing layers, a very different 'philosophy' of approach is often taken for unbounded problems, which more closely follows standard boundary layer precepts. Thus, in the 2D boundary layer cross-flow

integration procedure of Bradshaw and coworkers[40,41] the cross-flow (normal) velocity is obtained from the continuity equation while the cross-flow pressure variation is arrived at from the normal momentum equation. Here, the roles of the cross-flow equations are reversed. This approach has better convergence characteristics than the SIMPLE procedure, and, if the pressure variation is negligible, reduces to a standard boundary layer solution requiring no iterations.

Recently, Dash and Sinha[8] have reformulated the 2D cross-flow equations to obtain an independent equation for the cross-flow velocity which requires no assumptions about the cross-flow pressure or density variations. This provides a noniterative solution to the cross-flow equations for unbounded flows in situations with large cross-flow variations, and thus, improves upon the iterative procedure of Bradshaw and coworkers. An extension of this noniterative cross-flow procedure to 3D free jet flows is discussed in this report. The numerical framework for the parabolic (streamwise) portion of the jet mixing solution parallels that of SCIP3D as will be summarized below.

In the new cross-flow approach formulated:

(1) continuity-based equations for the cross-flow velocity components, V and W, are arrived at via combining the continuity and cross flow momentum equations, and, differential equation-of-state relations, subjected to fixed values of parabolic variables, U (streamwise velocity) and H (total enthalpy) arrived at apriori;

(2) the V (or W) equation is coupled to the W (or V) and P dependent variables only through vertical (z direction) derivative terms - thus in the absence of local cross-flow, no coupling occurs and V (or W) can be solved independently as in the 2D approach of Dash and Sinha;

(3) recognizing that V and W must be closely coupled in vortical (e.g., corner) regions, the V and W equations are solved concurrently in a coupled fashion with the cross-flow pressure field lagged;

(4) the cross-flow pressure field is updated using a cross-flow momentum equation - if the pressure changes are negligible, the solution is converged and no iterations are required; if the pressure changes are substantial, Step (3) is repeated using the updated pressure field; and,

(5) the direction of the cross-flow integration sweeps are alternated at subsequent steps to eliminate biasing of the difference relations.

The present coupled, explicit cross-flow solution procedure is restricted to free (unbounded) jet flowfields with quarter plane symmetry. For other subsonic jet mixing problems with different types of boundary conditions, the cross-flow solution procedure requires modification.

4.2 Parabolic Marching Procedure

The 'parabolic portion' of the pressure-split PNS marching integration is performed using a variant of the SCIP3D integration procedure with the following modifications:

(1) the streamwise (axial) momentum equation is solved with $\alpha = 0$ so that $E_U = \rho U^2$ (rather than $P+\rho U^2$) and the pressure gradient, $\overline{\partial P/\partial x}$, is treated as a prescribed forcing function (see eq. 1);

(2) an upwind variant of the MacCormack predictor/corrector algorithm is employed (see ref. 1);

(3) the wave portion of the jet growth rule given by eq. (19) is eliminated (i.e., $dz_U/dx = z_U(\partial f/\partial z)_{JMAX}/f_1$);

(4) a simple subsonic decode procedure is utilized to obtain the non-conservation variables from the $\overline{E}$ conservation array after both the predictor and corrector steps, viz.:

$$f = E_f/\rho U$$

where:

$$E_f = \rho U f$$

and;

(5) the pressure field is approximated by:

$$\frac{\partial P}{\partial \xi} = \overline{\frac{\partial P}{\partial x}} + a_y \frac{\partial P}{\partial \eta} + a_z \frac{\partial P}{\partial \zeta} \qquad (36)$$

which is solved in an explicit predictor/corrector fashion using central differences, with $\overline{\partial P/\partial x}$ specified.

At the completion of the predictor/corrector 'parabolic integration', 'firm' values of the variables U, H and ϕ are obtained, and 'approximate'

values of the variables V, W and P are available which do not satisfy the continuity equation. The values of V, W and P are then revised to satisfy the coupled continuity and cross-flow (V,W) momentum equations with U, H and ϕ fixed, and, with the approximate values of V, W and P used in evaluating coefficients for the cross-flow integration to be discussed below. No iterations between the parabolic and cross-flow sweeps are performed; rather, the axial step size is reduced in regions with large gradients (such as the initial jet mixing region) to minimize errors incurred by this approximation.

4.3 Cross-Flow Equations

Expanding the mapped form of the continuity equation yields the form listed below (eq. 37).

$$\frac{\partial \rho}{\partial \xi} + \tilde{V} \frac{\partial \rho}{\partial \eta} + \tilde{W} \frac{\partial \rho}{\partial \zeta} + \left(\frac{\rho b_y}{U} \right) \frac{\partial V}{\partial \eta} + \left(\frac{\rho b_z}{U} \right) \frac{\partial W}{\partial \zeta}$$

$$= \frac{\rho}{U} \left[- \frac{\partial U}{\partial \xi} + a_y \frac{\partial U}{\partial \eta} + a_z \frac{\partial U}{\partial \zeta} \right] \qquad (37)$$

In eq. (37), b_y, b_z, a_y and a_z are mapping transformation terms and the derivatives of the streamwise (axial) velocity, U_ξ, U_η and U_ζ are known from the parabolic integration performed apriori. The density derivatives in the continuity equation are replaced by derivatives of pressure and cross-flow velocities, as well as known derivatives of streamwise velocity and total enthalpy. This is accomplished by differentiating the perfect gas state relation (eq. 38) which yields the density derivative ρ_α given by eq. (39) where α represents the ξ, η or ζ directions.

$$H = \frac{\gamma}{\gamma-1} \frac{P}{\rho} + \frac{1}{2} (U^2 + V^2 + W^2) \qquad (38)$$

which yields:

$$\rho_\alpha = \frac{\gamma}{a^2} P_\alpha + \frac{\rho}{a^2} (\gamma-1) \left[U U_\alpha + V V_\alpha + W W_\alpha - H_\alpha \right] \qquad (39)$$

An important consideration concerns the treatment of the pressure gradient term, P_ζ. Here, equation (36) is utilized which brings in the pressure-split approximation. Substituting the ρ_a expression into equation (37) with P_ζ given by equation (36) yields the Modified Continuity Equation given by equation 40.

Modified Continuity Equation

$$\begin{aligned}
&(\tilde{\gamma}\frac{\tilde{V}}{\tilde{U}})V_\xi + \left[\tilde{\gamma}\tilde{V}\frac{V}{U} + \frac{b_y}{\gamma M^2}\right]V_\eta + (\tilde{\gamma}\tilde{W}\frac{\tilde{V}}{\tilde{U}})V_\zeta \\
&\quad + (\tilde{\gamma}\frac{\tilde{W}}{\tilde{U}})W_\xi + (\tilde{\gamma}\tilde{V}\frac{\tilde{W}}{\tilde{U}})W_\eta + \left[\tilde{\gamma}\tilde{W}\frac{W}{U} + \frac{b_z}{\gamma M^2}\right]W_\zeta \\
&\quad + (b_{y\beta}\frac{V}{\tilde{U}})P_\eta + (b_{z\beta}\frac{W}{\tilde{U}})P_\zeta = B_P
\end{aligned} \tag{40}$$

where:

$$\begin{aligned}
B_P = &-\frac{\overline{\partial P/\partial x}}{\rho U} - \left[\tilde{\gamma} + \frac{1}{\gamma M^2}\right]U_\xi + \left[\frac{a_y}{\gamma M^2} - \tilde{\gamma}\tilde{V}\right]U_\eta \\
&+ \left[\frac{a_z}{\gamma M^2} - \tilde{\gamma}\tilde{W}\right]U_\zeta + \frac{\tilde{\gamma}}{\tilde{U}}\left[H_\xi + \tilde{V}H_\eta + \tilde{W}H_\zeta\right]
\end{aligned} \tag{41}$$

The cross-flow momentum equations in the y and z coordinate directions in transformed ξ, η and ζ coordinates are listed below:

$$V_\xi + \tilde{V}V_\eta + \tilde{W}V_\zeta + \frac{b_y}{\rho U}P_\eta = \frac{V_V}{\rho U} \tag{42}$$

$$W_\xi + \tilde{V}W_\eta + \tilde{W}W_\zeta + \frac{b_z}{\rho U}P_\zeta = \frac{V_W}{\rho U} \tag{43}$$

where V_V and V_W are the parabolized stress terms, and $\tilde{\gamma}$, β, $\tilde{V}$ and $\tilde{W}$ are defined by:

$$\tilde{\gamma} = (\gamma-1)/\gamma$$

$$\beta = \rho U^2$$

$$\tilde{V} = [b_y \frac{V}{U} - a_y]$$

$$\tilde{W} = [b_z \frac{W}{U} - a_z]$$

The Modified Continuity Equation (eq. 40) and these two momentum equations comprise three equations for the cross-flow variation of three variables, V, W and P, with the parabolic variables U and H known apriori. By manipulations analogous to those of reference 8, continuity-based equations for V and W can be obtained which would be independent of all other parameters in the absence of cross-flow. The procedure for obtaining the 'W equation' is described below.

Starting with the Modified Continuity Equation, we replace the terms V_ξ and P_ζ with their equivalents obtained from the V (eq. 42) and W (eq. 43) momentum equations, respectively. The V_ξ term is given by:

$$(\tilde{\gamma}\frac{V}{U})V_\xi = (\tilde{\gamma}\frac{V}{U}) \left[\frac{V_V}{\rho U} - \frac{b_y}{\rho U} P_\eta - \tilde{V}V_\eta - \tilde{W}V_\zeta \right] \tag{44}$$

The P_ζ term is given by:

$$(b_z \frac{W}{\beta})P_\zeta = (\frac{\rho UW}{\beta}) \left[\frac{V_W}{\rho U} - W_\xi - \tilde{V}W_\eta - \tilde{W}W_\zeta \right] \tag{45}$$

Substituting the expressions given by eqs. (44) and (45) into the Modified Continuity Equation, and grouping like terms, yields the expression:

$$\boxed{\begin{aligned} &(\frac{W}{\gamma U})W_\xi + (\frac{W\tilde{V}}{\gamma U})W_\eta + (\frac{W\tilde{W}}{\gamma U} - \frac{b_z}{\gamma M^2})W_\zeta \\ &= - B_P + \frac{\tilde{\gamma}V}{\beta} V_V + \frac{W}{\beta} V_W + \frac{b_y V}{\gamma\beta} P_\eta + \frac{b_y}{\gamma M^2} V_\eta \end{aligned}} \tag{46}$$

Following the analogous steps, the 'V equation' listed below is obtained.

$$\left(\frac{V}{\gamma U}\right)V_{\xi} + \left(\frac{V\tilde{V}}{\gamma U} - \frac{b_y}{\gamma M^2}\right)V_{\eta} + \left(\frac{V\tilde{W}}{\gamma U}\right)V_{\zeta}$$

$$= -B_P + \frac{V}{\beta}V_V + \frac{\tilde{\gamma}W}{\beta}V_W + \frac{b_z W}{\gamma\beta}P_{\zeta} + \frac{b_z}{\gamma M^2}W_{\zeta} \qquad (47)$$

4.4 Cross-Flow Integration Procedure

Referring to Figure 3, the cross-flow plane, ξ = constant, is subdivided into IMAX-1 equally spaced intervals, $\Delta\eta$, where $\eta = (I-1)/(IMAX-1)$, and, JMAX-1 equally spaced intervals, $\Delta\zeta$, where $\zeta = (J-1)/(JMAX-1)$. For quarter plane symmetry, the boundary conditions are as follows:

$W = 0$ on $\zeta = 0$ (J=1)

$V = 0$ on $\eta = 0$ (I=1)

$P = P_E$ on $\zeta = 1$ (J=JMAX); $\eta = 1$ (I=IMAX)

Equations (40) and (41) are solved in the following manner on the plane ξ = constant:

(1) the turbulent stress terms V_V and V_W are treated as forcing functions terms;

(2) the pressure gradient terms P_{η} and P_{ζ} are lagged;

(3) the W equation (40) is integrated sweeping upward from $\xi = 0$ to 1 (i.e., from J = 1 to JMAX);

(4) the V equation (41) is integrated sweeping spanwise from $\eta = 0$ to 1 (i.e., from I = 1 to IMAX);

(5) the W and V equations are solved concurrently in a coupled manner which entails either:

C-2

(a) sweeping upward from J to J + 1 with a nested spanwise sweep from I = 1 to IMAX; or,

(b) sweeping spanwise from I to I + 1 with a nested upward sweep from J = 1 to JMAX.

(6) after the coupled W and V solutions are obtained, the cross-flow pressure field is upgraded:

(a) sweeping downward from $\xi = 1$ to 0 (i.e., from J = JMAX to J = 1) using the W normal momentum equation if an upward (a type) sweep was used in Step (5); or,

(b) sweeping spanwise from $\eta = 1$ to 0 (i.e., from I = IMAX to (I = 1) using the V normal momentum equation if a spanwise (b type) sweep was used in Step (5).

Referring to Figure 50, the V and W equations are solved using the triangular-type difference elements exhibited. The W equation is integrated upward in the ξ direction from known values of W (= 0) on the plane of symmetry, $\zeta = 0$. The V equation is integrated spanwise in the η direction from known values of V (= 0) on the plane of symmetry, $\eta = 0$. The upward/spanwise integrations in the ζ/η directions are performed using a two point (trapezoidal) procedure (as in the 2D cross-flow analysis of reference 8). The other family of derivatives (η for W equation, ζ for V equation) are evaluated using central differences.

4.5 Pressure-Split PNS Subsonic Square Jet Calculation

This square jet calculation (Mach .5 into quiescent stream) was performed for a nozzle having the exit plane boundaries $y = \pm 1$ and $z = \pm 1$. The calculations were performed utilizing quarter plane symmetry with the initial grid extending to y = 2 and z = 2 yielding a substantial buffer region of uniform exhaust flow about the jet. Figure 51 depicts predicted ϕ contours at x = 20 obtained utilizing both the $k\varepsilon$ and kW turbulence models with the full pressure-split methodology. The faster mixing predicted by the $k\varepsilon$ model coincides with past experience for low speed axisymmetric jets. The pressure split solutions yield jet contours which have distinct kinks in the outer mixing region. This is to be contrasted with the smooth contours obtained by suppressing the effects of convective velocities on the solution

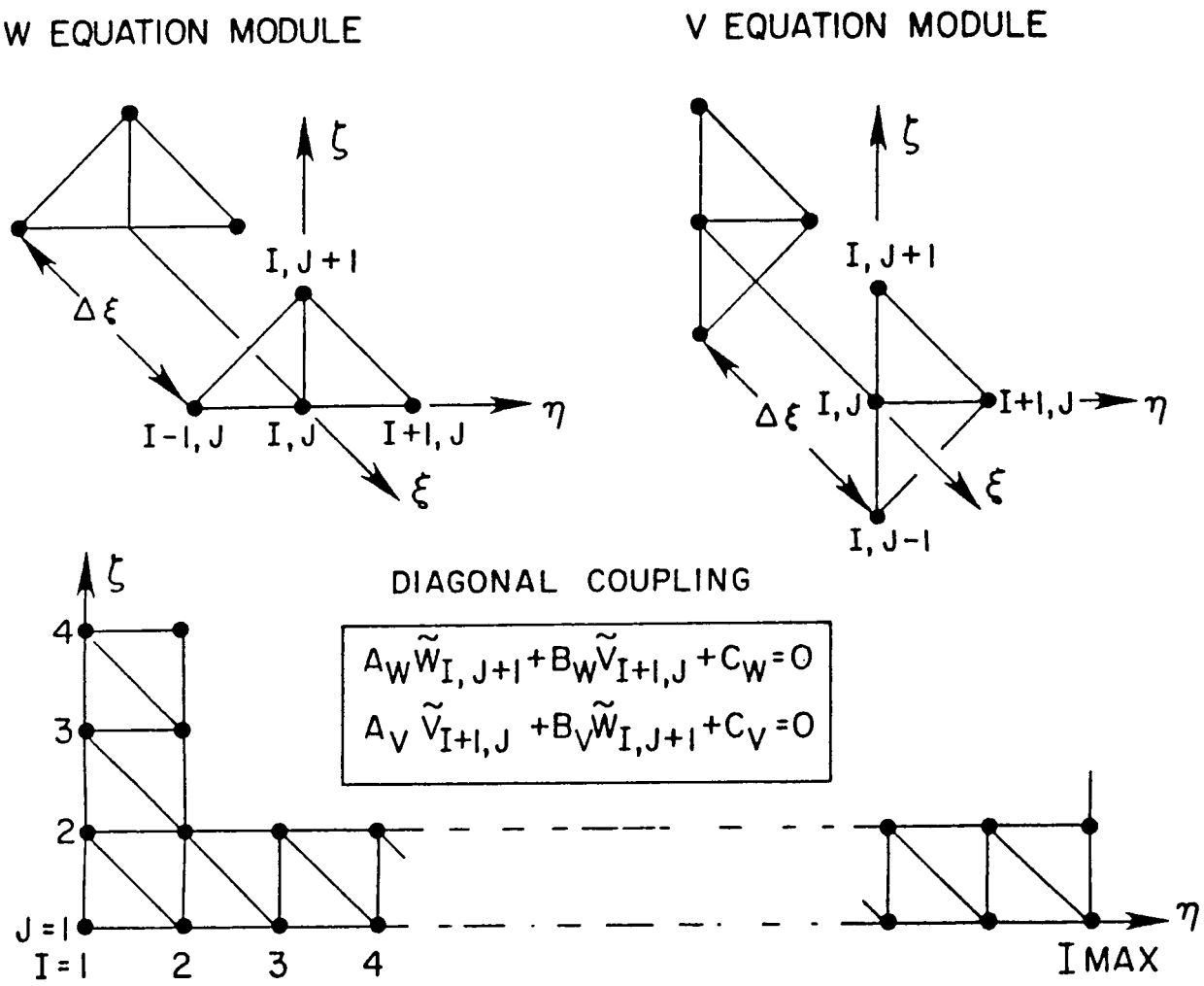

FIGURE 50. V And W Grids And Diagonal Coupling Nomenclature For Subsonic Cross-Flow Solution.

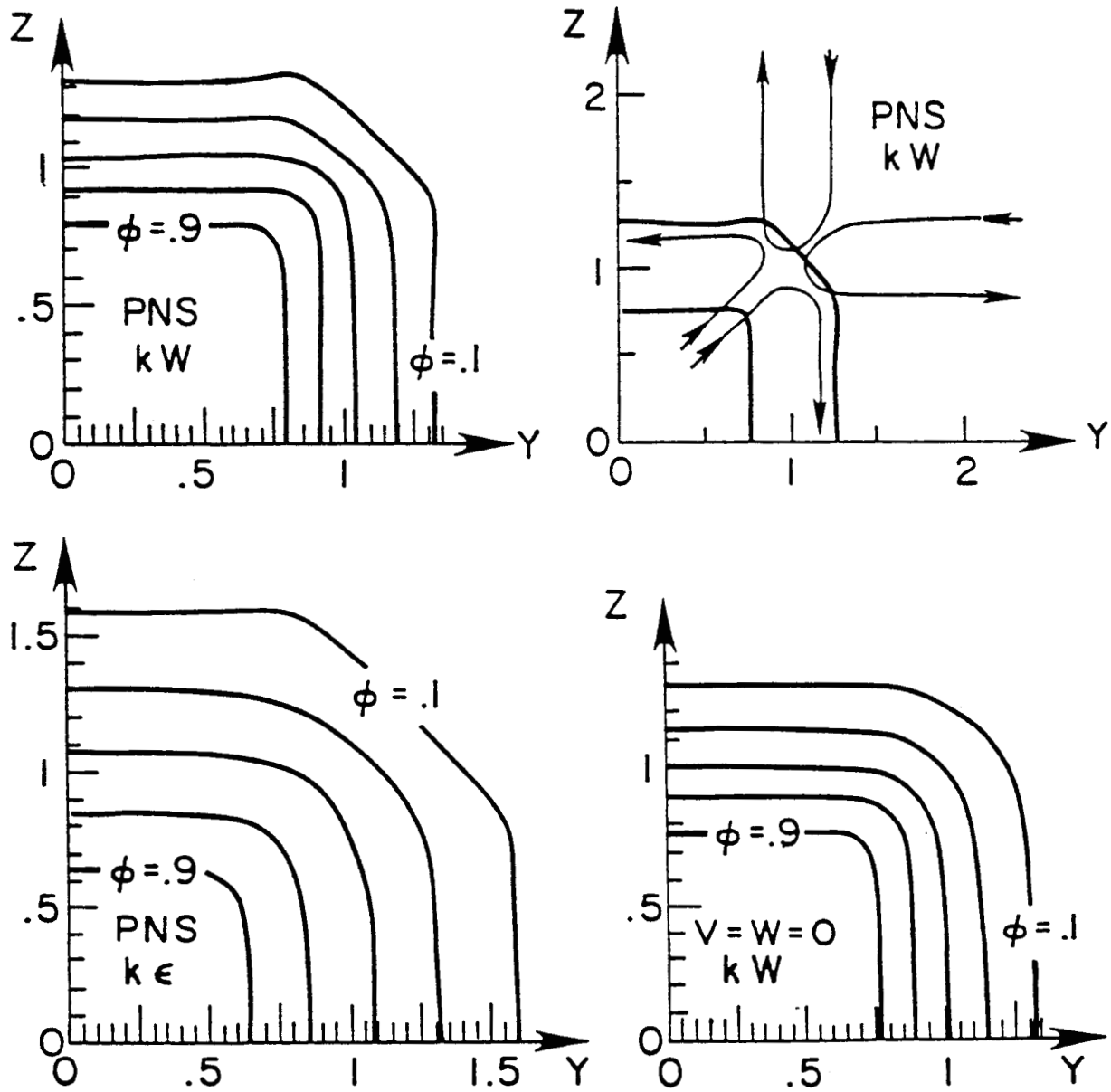

FIGURE 51. Square Subsonic Jet Calculations; Cross-Flow Contours At x = 20.

(i.e., by enforcing both V and W = 0 and thus generating a 'diffusion only' type solution).

The kinks in the ϕ contours appear to be associated with the 'abrupt' breakdown of the initial vortex sheet surrounding the jet with the subsequent formation of a pair of counter-rotating streamwise vortices symmetrically spaced about the corner region, as schematized in Figure 51*. A vector plot of the cross flow velocity field corresponding to the PNS/kW solution at x = 20 is given in Figure 52. We note that the jet entrainment velocities on the symmetry planes are in accord with values for planar jet mixing solutions. The 'flattening' of the outer ϕ profiles along the 45° plane (y = z) is attributed to the significantly enhanced entrainment produced by the 3D corner mixing. The 'kinks' in the outer ϕ profiles correspond to the positions where the streamwise vortices 'pump fluid out' of the jet.

The subsequent development of the jet out to x = 100 (PNS/kW solution) is exhibited by the ϕ = 0.1 contours at x = 40 (inner contour is ϕ = 0.9) 60, 80 and 100 superimposed on the cross-flow velocity vector field (Figure 53). The corner-induced streamwise vortex pattern persists in the cross-flow plane despite the nearly circular behavior of the streamwise parabolic solution. The variation of ϕ and turbulent kinetic energy, k, along the jet centerline are exhibited in Figure 54, and, are compared with 'corresponding' planar and axisymmetric jet solutions (viz., solutions having nozzle exit heights/diameters of 2) predicted using the SPLITP jet mixing model.

4.6 Pressure-Split PNS 4/1 Aspect Ratio

A 4/1 aspect ratio jet was analyzed having conditions identical to those of the square jet case. The nozzle exit extended to y = $\pm$2 and z = $\pm$0.5, while the initial grid, employing quarter plane symmetry, extended to y = 2.5 and z = 1 (i.e., a uniform buffer of freestream flow of width ~ 0.5

---

* The numerical approach may also have some influence on the vortical behavior predicted, e.g., the spatial marching procedure provides no mechanism for streamwise pressure gradients and/or upstream influence effects to be accounted for, which might influence the results.

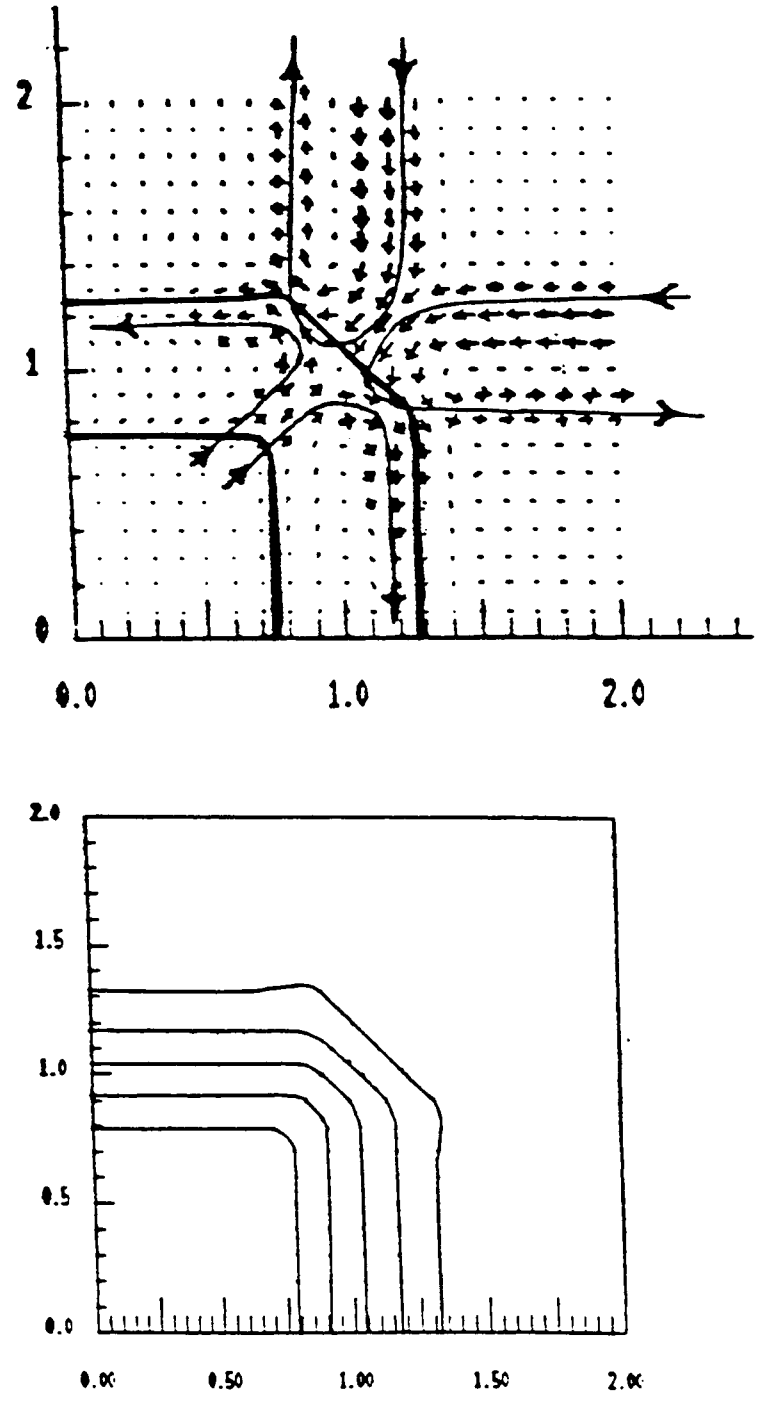

FIGURE 52. Square Jet Calculation; Streamwise Vortices Generated By Corner Region At x = 20.

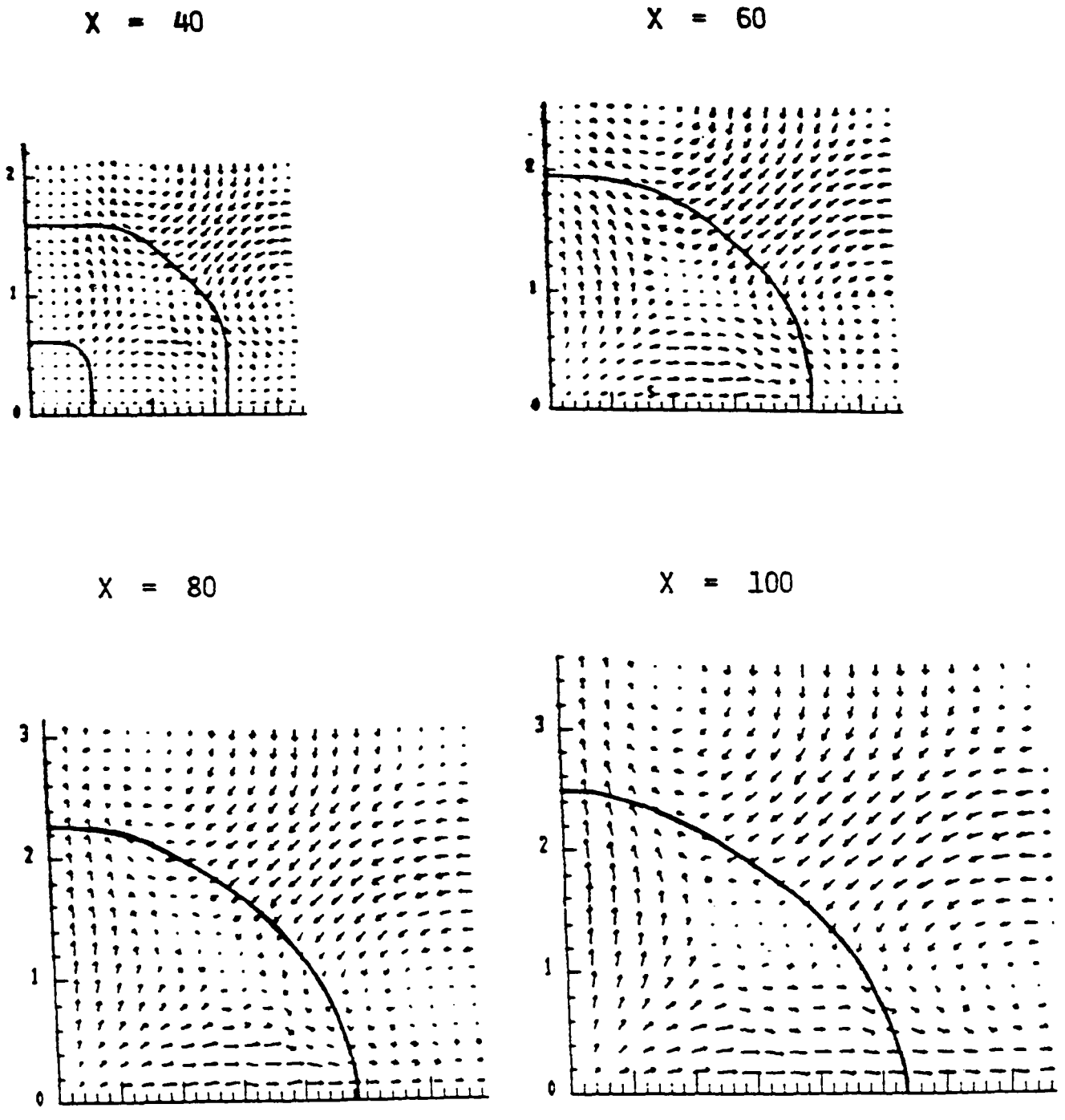

FIGURE 53. Subsonic Square Jet Calculation; ϕ = 0.1 Contours Superimposed On Cross-Flow Vectors Maps At x = 40 - 100.

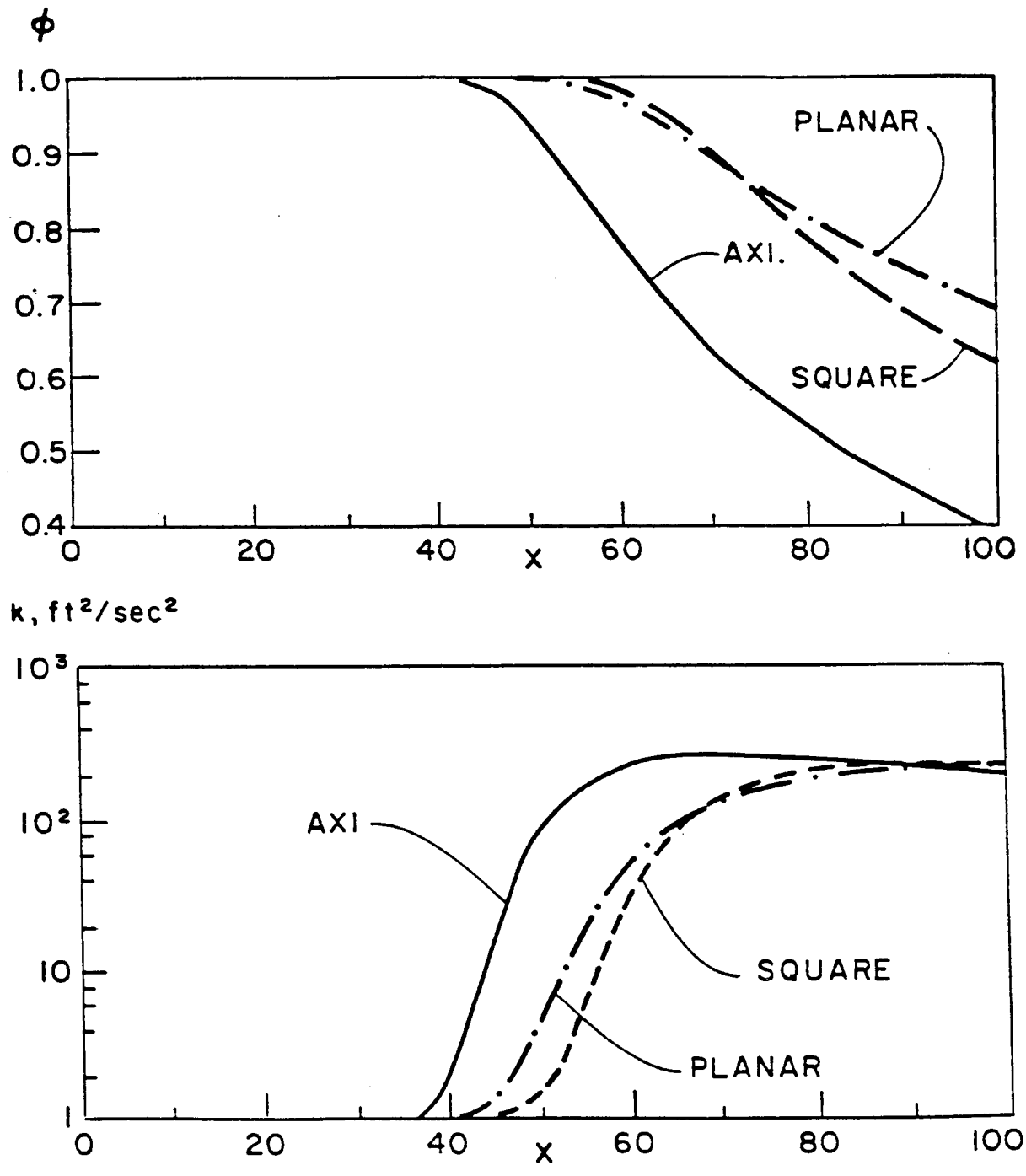

FIGURE 54. Subsonic Square Jet Predictions For ϕ And k Variations Along Axis.

surrounded the jet initially). Figure 55 depicts predicted jet contours at x = 20 using the kW turbulence model with the pressure split, PNS approach, and, with the 'diffusive limit' approach whereby the convective velocities are suppressed (V = W = 0). As in the square jet case, the PNS ϕ contours exhibit pronounced kinks associated with the corner generated streamwise vortices depicted in Figure 55, while the case with convective velocities suppressed yields smooth, kink-free contours.

The development of the jet out to x = 100 is exhibited by the ϕ = 0.1 contours in the cross-flow plane at x = 40 (inner contour is ϕ = 0.9) 60, 80 and 100 (Figure 56) with a schematic of the streamwise vortex pattern superimposed. By x = 100, the jet contour takes on an elliptic appearance with the vortex-induced kinks no longer evident. The ϕ contours in the y = 0 and z = 0 symmetry planes out to x = 300 are depicted in Figure 57, indicating that by x = 300, the flow is nearly circular. Profiles of ϕ and turbulent kinetic energy, k, in the two symmetry planes at x = 100, 200 and 300 are exhibited in Figure 58. The variation of axial velocity, U, and turbulent kinetic energy, k, along the jet axis of symmetry are depicted in Figure 59.

4.7 Parabolic Marching Approach (P = P(x) Only)

An alternate procedure for analyzing subsonic jet mixing problems involves the solution of a reduced set of parabolic 'boundary layer equations'. In this approach, the cross-flow grid must be aligned so that one coordinate direction is essentially normal to the jet boundary. This can be accomplished using the hybrid adaptive rectangular/cylindrical grid discussed previous (see Figure 4). Utilizing this adaptive grid, the z (cartesian) and r (cylindrical) directions align themselves normal to the jet boundary. Thus, W represents the velocity in the normal (entrainment) direction and V represents the cross-flow velocity. The equations solved neglect pressure variations in the cross-flow plane (P = P(x) only). The solution procedure employs a single parabolic solution sweep whereby the V component of velocity is determined from the V-momentum equation while the W component of velocity is determined from the continuity equation aposteriori. The W-momentum equation is neglected consistent with the approximation of constant pressure in the cross-flow plane.

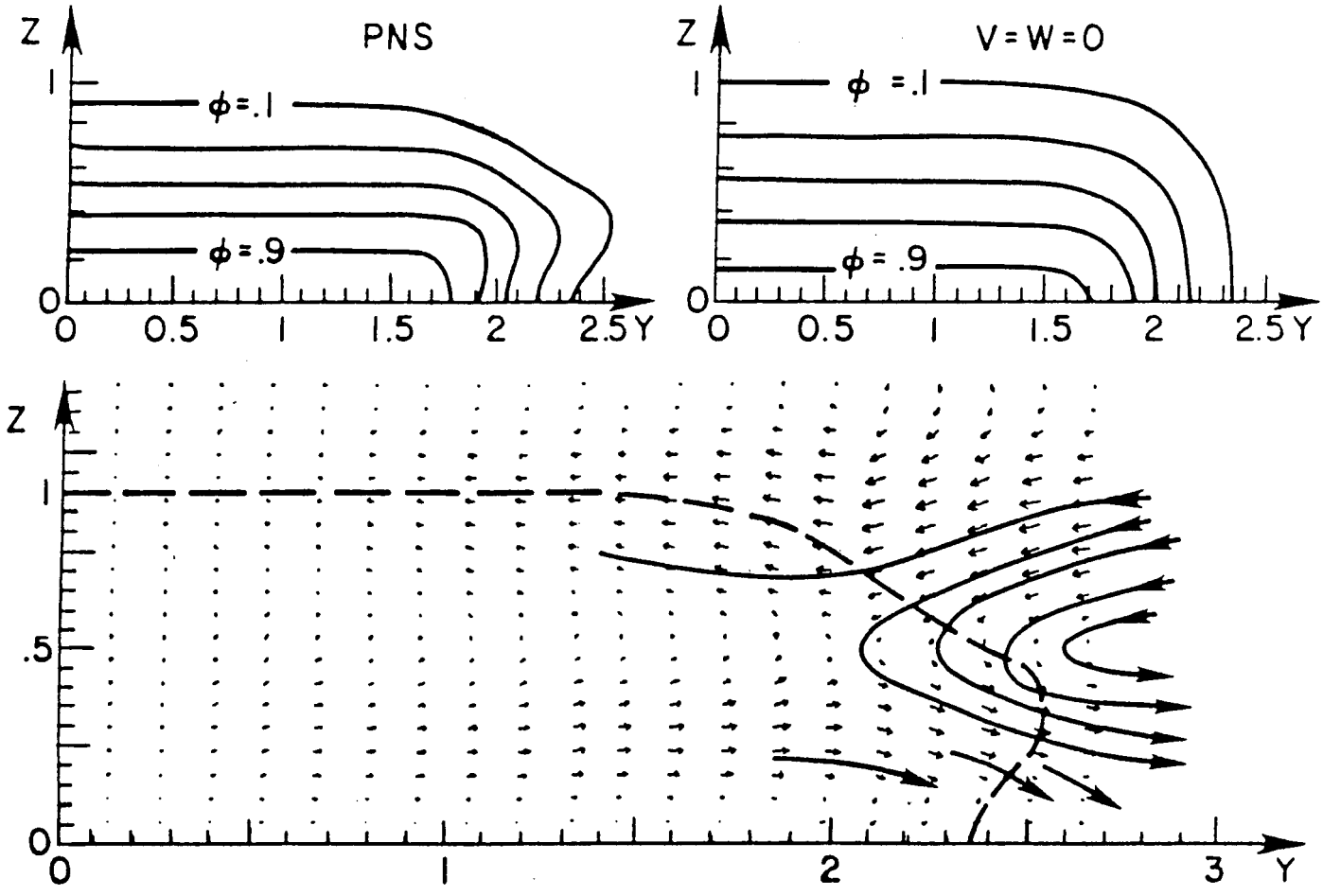

FIGURE 55. Rectangular Subsonic Jet Calculation, Contours At x = 20.

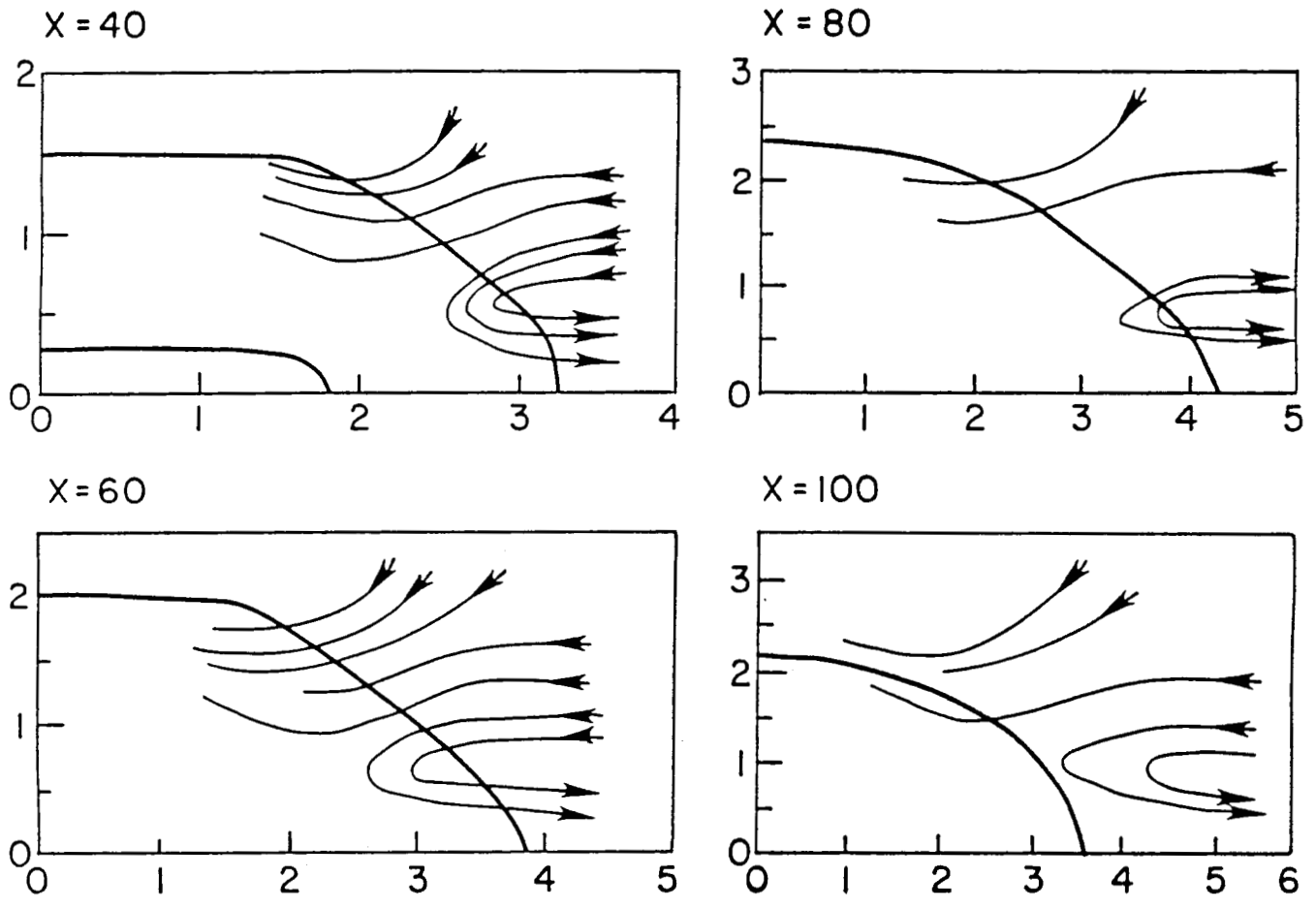

FIGURE 56. Rectangular Subsonic Jet Calculation, Contours At x = 40, 60, 80 And 100.

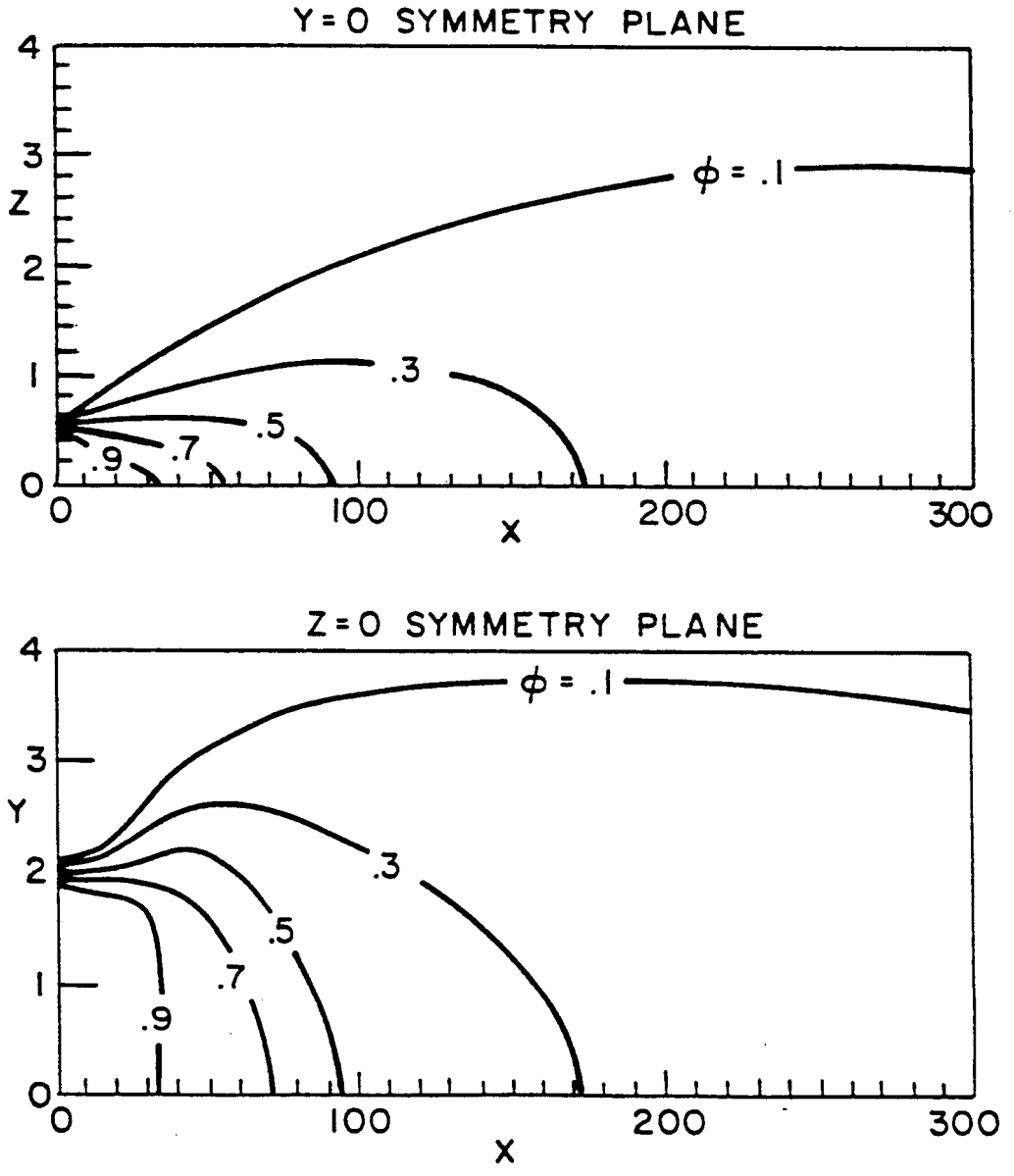

FIGURE 57. Rectangular Jet, ϕ Contours On y, z = 0 Symmetry Planes.

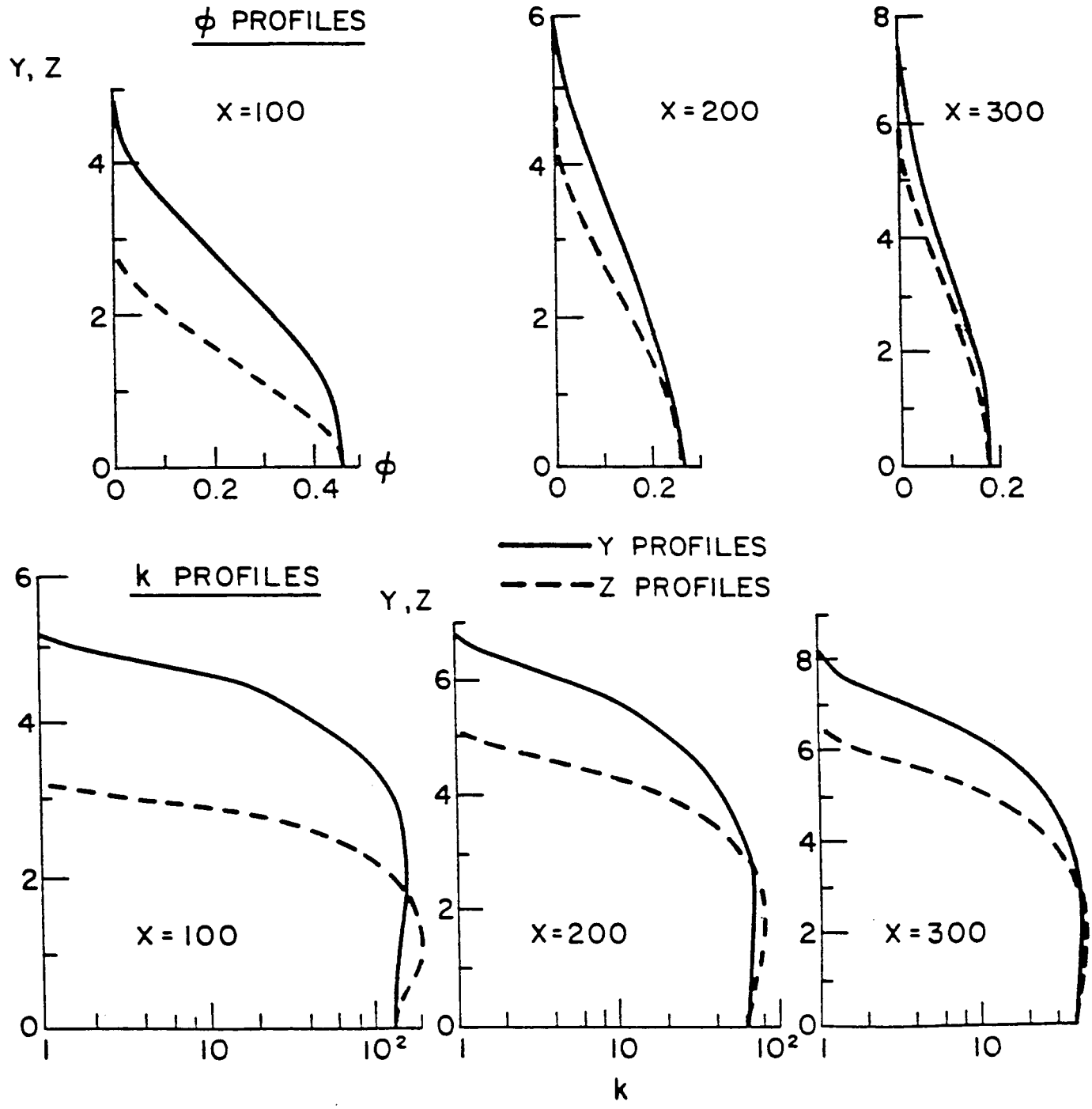

FIGURE 58. Subsonic Rectangular Jet, ϕ And k Profiles At x = 100, 200 And 300.

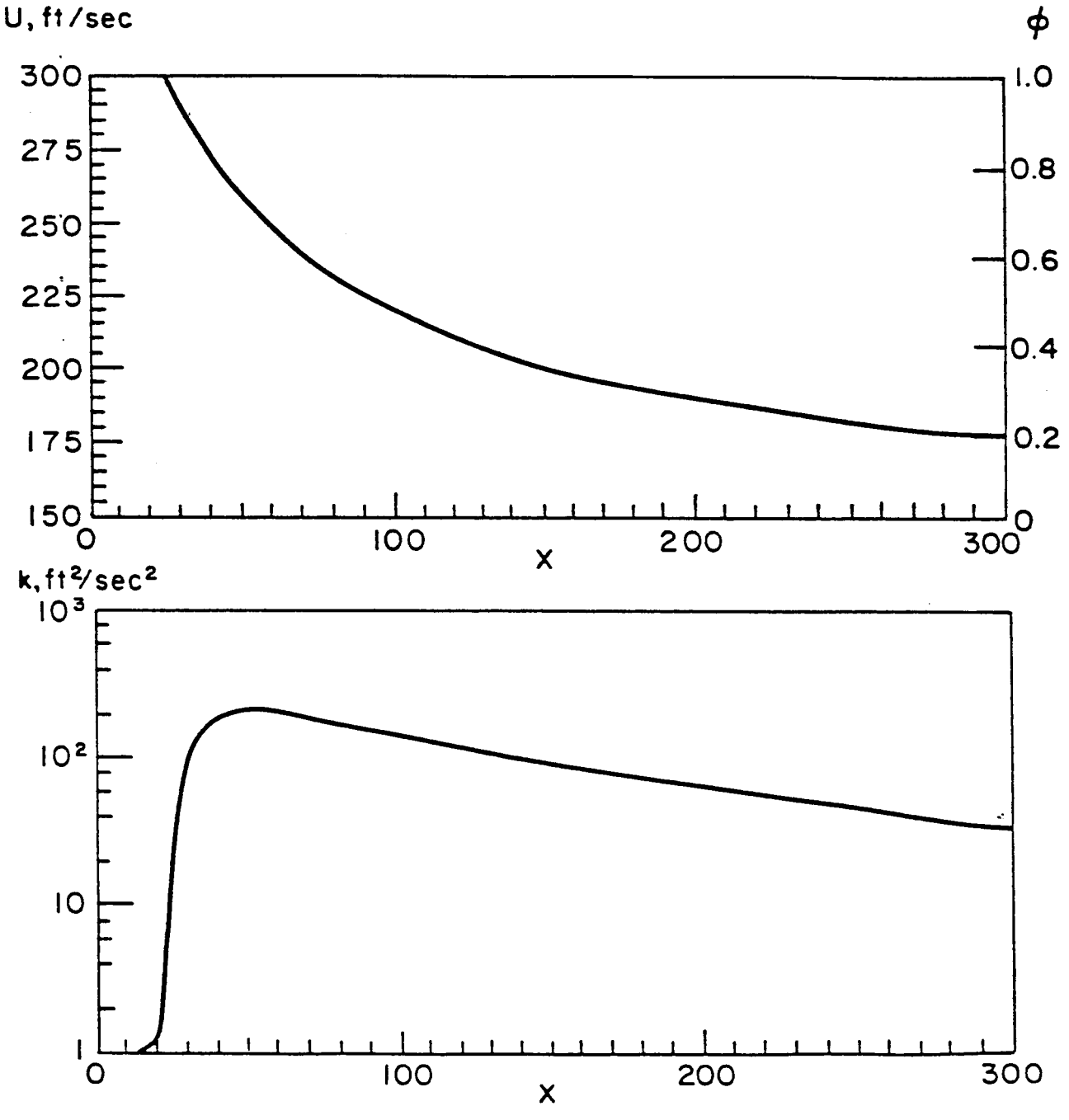

FIGURE 59. Subsonic Rectangular Jets, U And k-Axis Variations.

4.8 Parabolic Rectangular Jet Analysis in Adaptive Cylindrical Coordinates

The calculation described here utilized an adaptive cylindrical grid to analyze a 2/1 Aspect Ratio rectangular jet (M_J = 1, T_J = 800 °K) exhausting into a Mach .3 external stream (T_E = 278 °K). The cylindrical grid employed 21 points in the radial direction and 11 ϕ planes ($0 < \phi < \pi/2$). The calculation was performed using the simplified parabolic boundary layer run option described above. Figures 60 and 61 exhibit predicted ϕ and T contours in the y = 0 and z = 0 symmetry planes. Figures 62 and 63 exhibit predicted ϕ and T cross-flow contours at x = 5, 10, 20 and 30. ϕ and T cross-flow contours at x = 50 (Figure 64) show a nearly circular behavior.

4.9 Comparison of Parabolic and Supersonic PNS Predictions for 3/1 Aspect Ratio Rectangular Jet Using Hybrid Adaptive Grid

This calculation was performed for a hot Mach 3 exhaust stream (T_J = 2000 °K) exhausting into a colder Mach 3 external stream (T_E = 500 °K) to compare the simplified parabolic run option with a full supersonic PNS calculation. The calculations were performed using the rectangular/cylindrical hybrid adaptive grid with a moving origin. Figure 65 compares cross-flow ϕ contours for the two solutions at x = 20. Both exhibit the same 'kinked' behavior in the corner region. Figure 66 depicts the cross-flow velocity vector field at x = 20 for the parabolic solution - note that the cylindrical origin (here at y = 1) moves inward to maintain the same dimensions on the ϕ = 0 and $\phi = \pi/2$ planes. Figure 67 exhibits the evolution of the jet boundary contours from rectangular to circular.

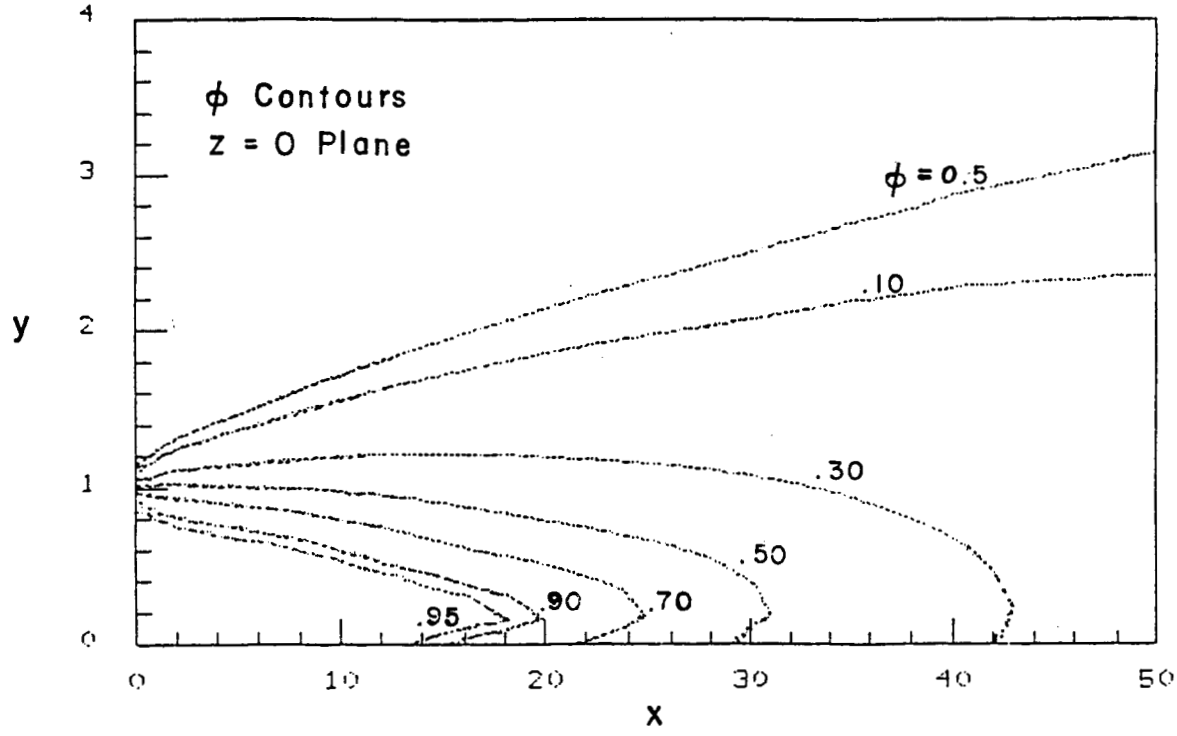

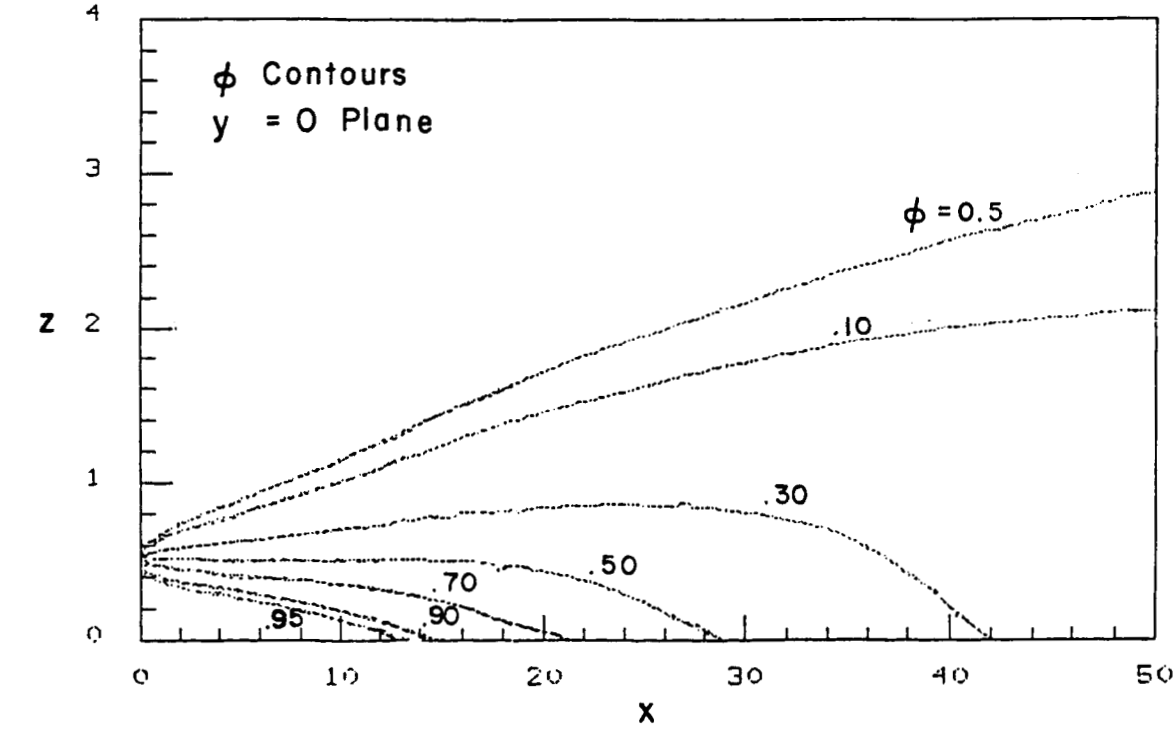

FIGURE 60. ϕ Contours For 2/1 Rectangular Jet, Parabolic Run Option.

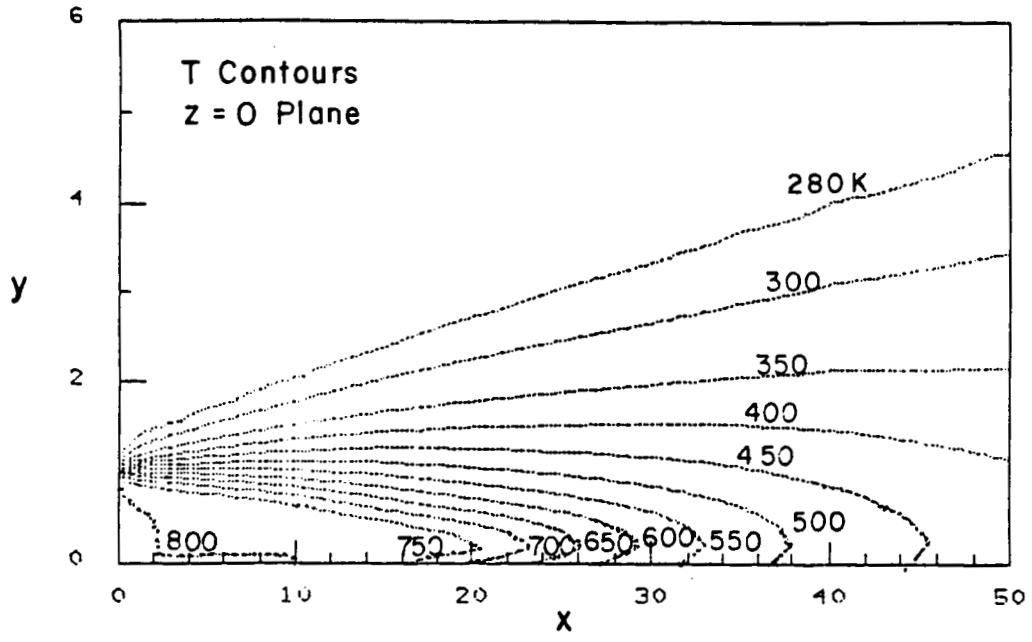

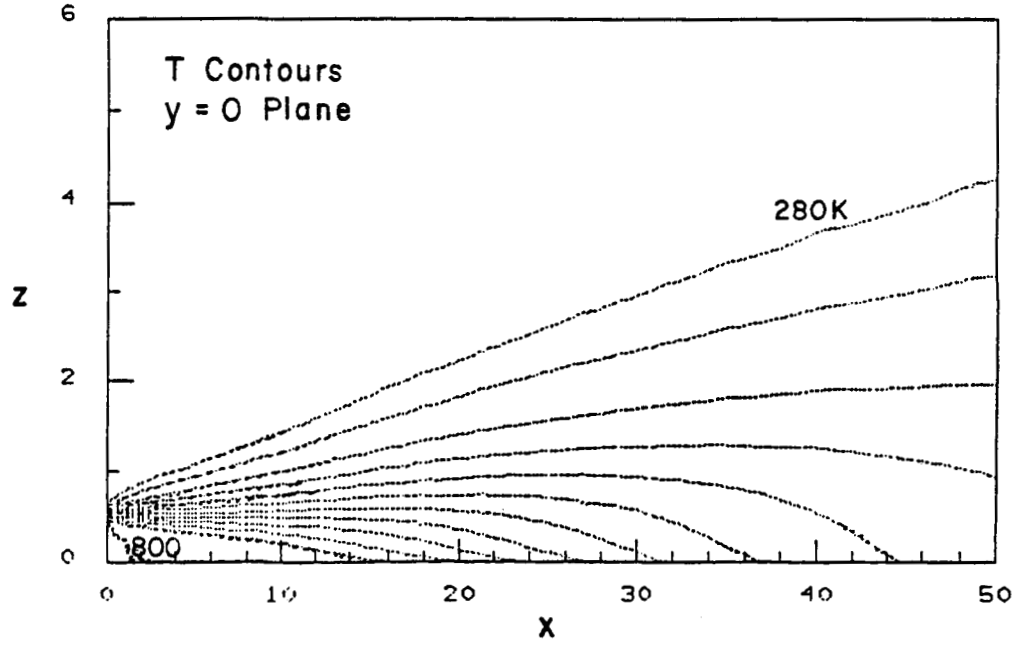

FIGURE 61. T Contours For 2/1 Rectangular Jet, Parabolic Run Option.

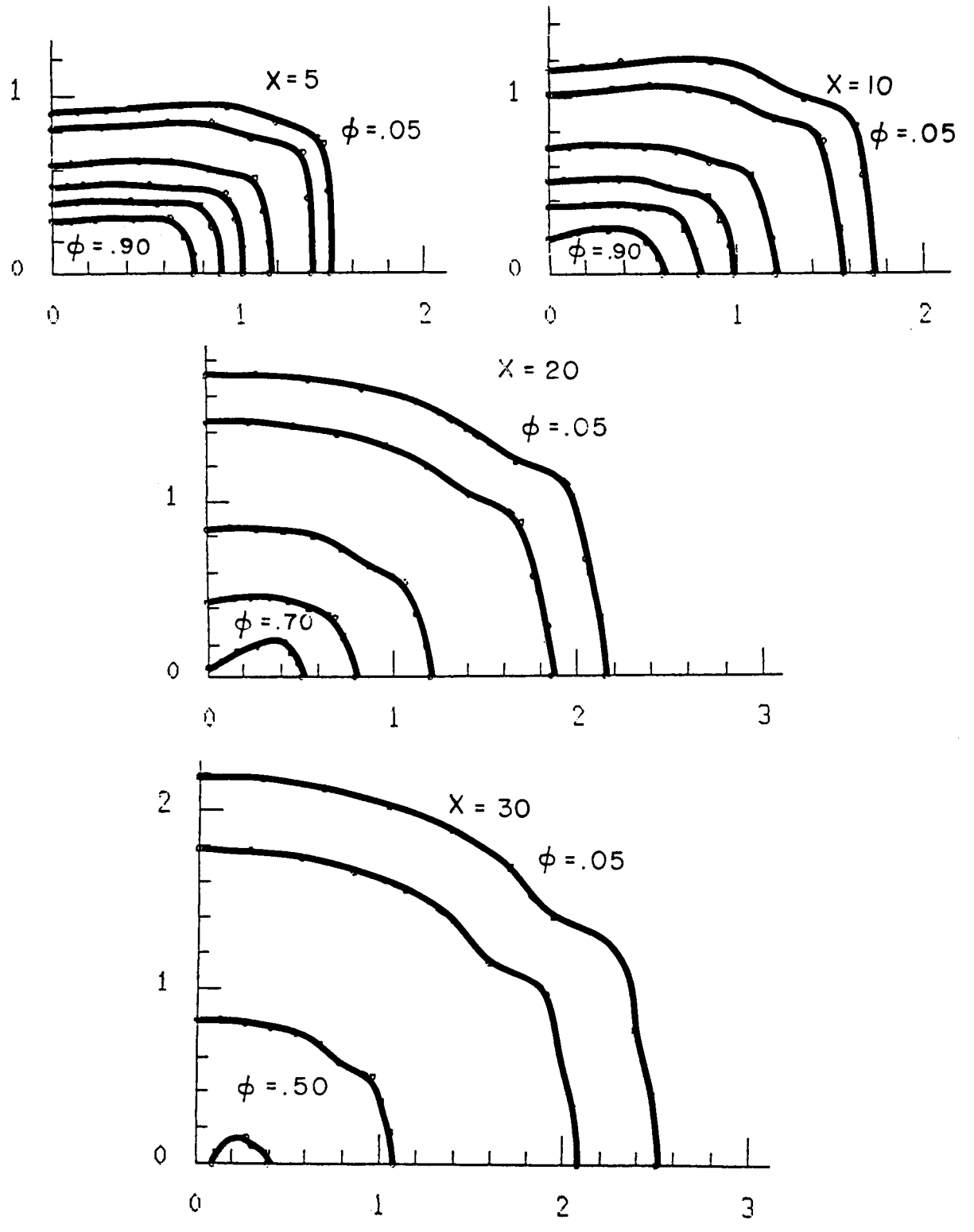

FIGURE 62. ϕ Cross-Flow Contours For 2/1 Rectangular Jet Problem.

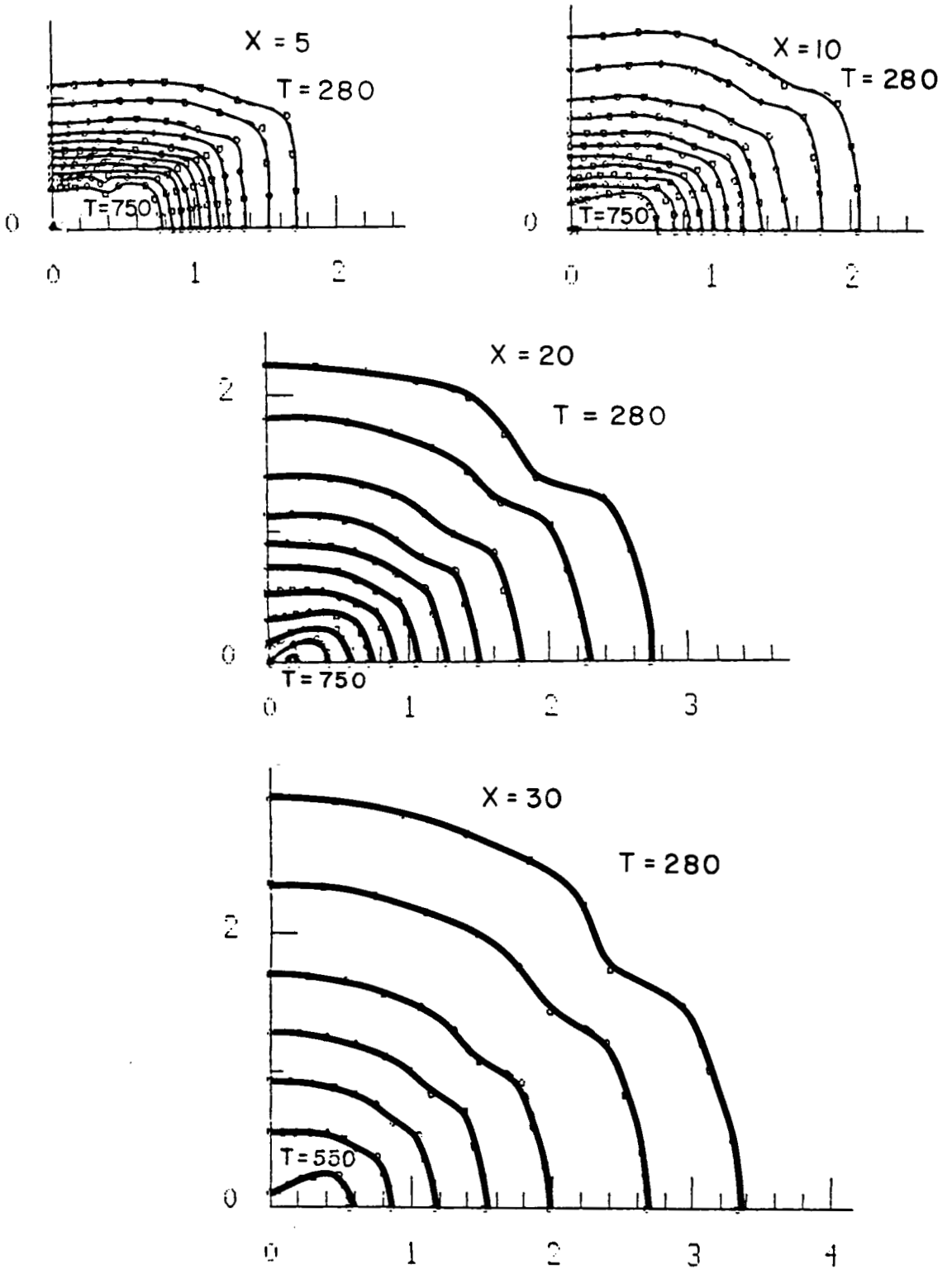

FIGURE 63. T Cross-Flow Contours For 2/1 Rectangular Jet Problem.

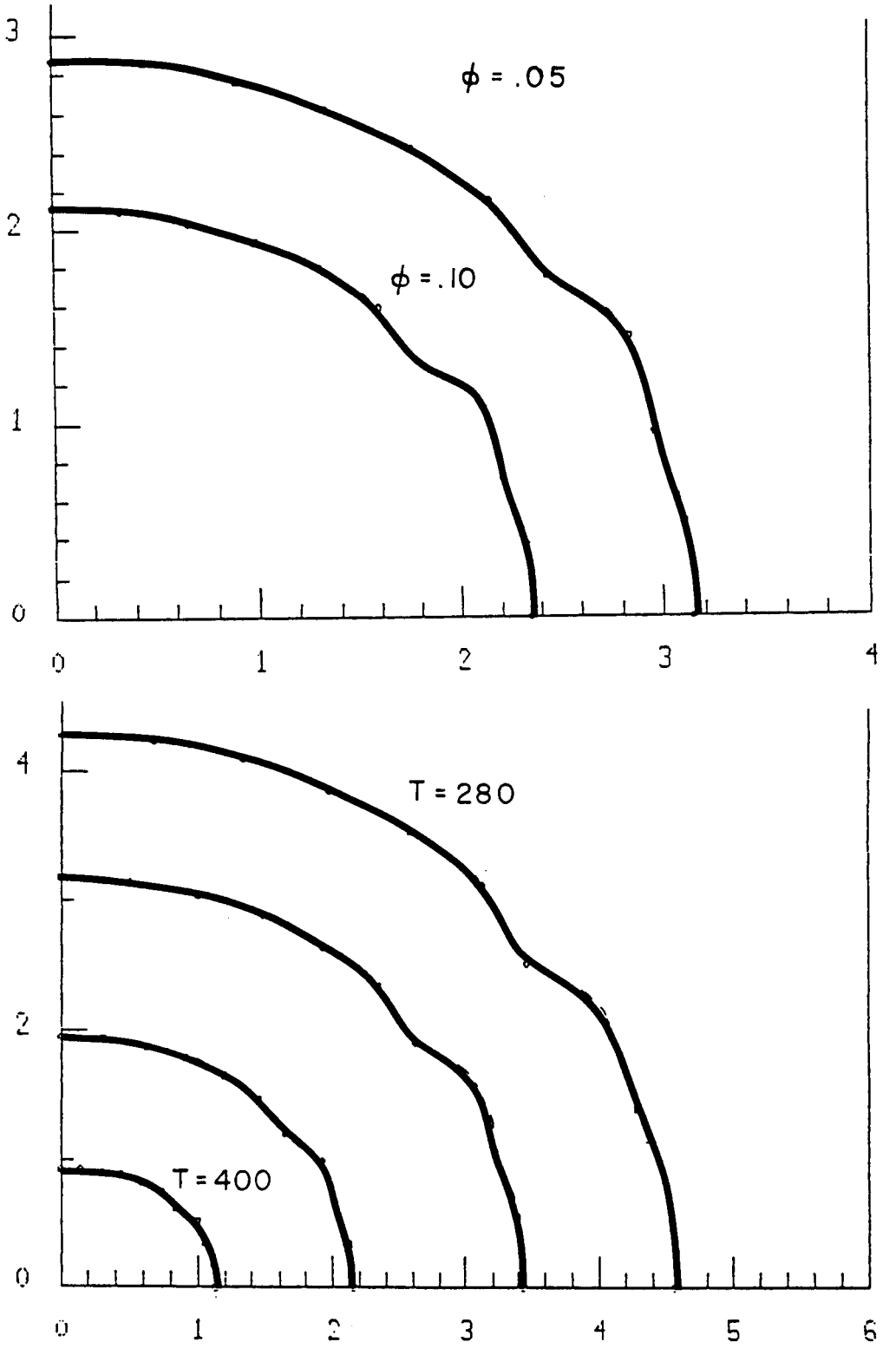

FIGURE 64. ϕ And T Cross-Flow Contours At x = 50 For 2/1 Rectangular Jet Problem.

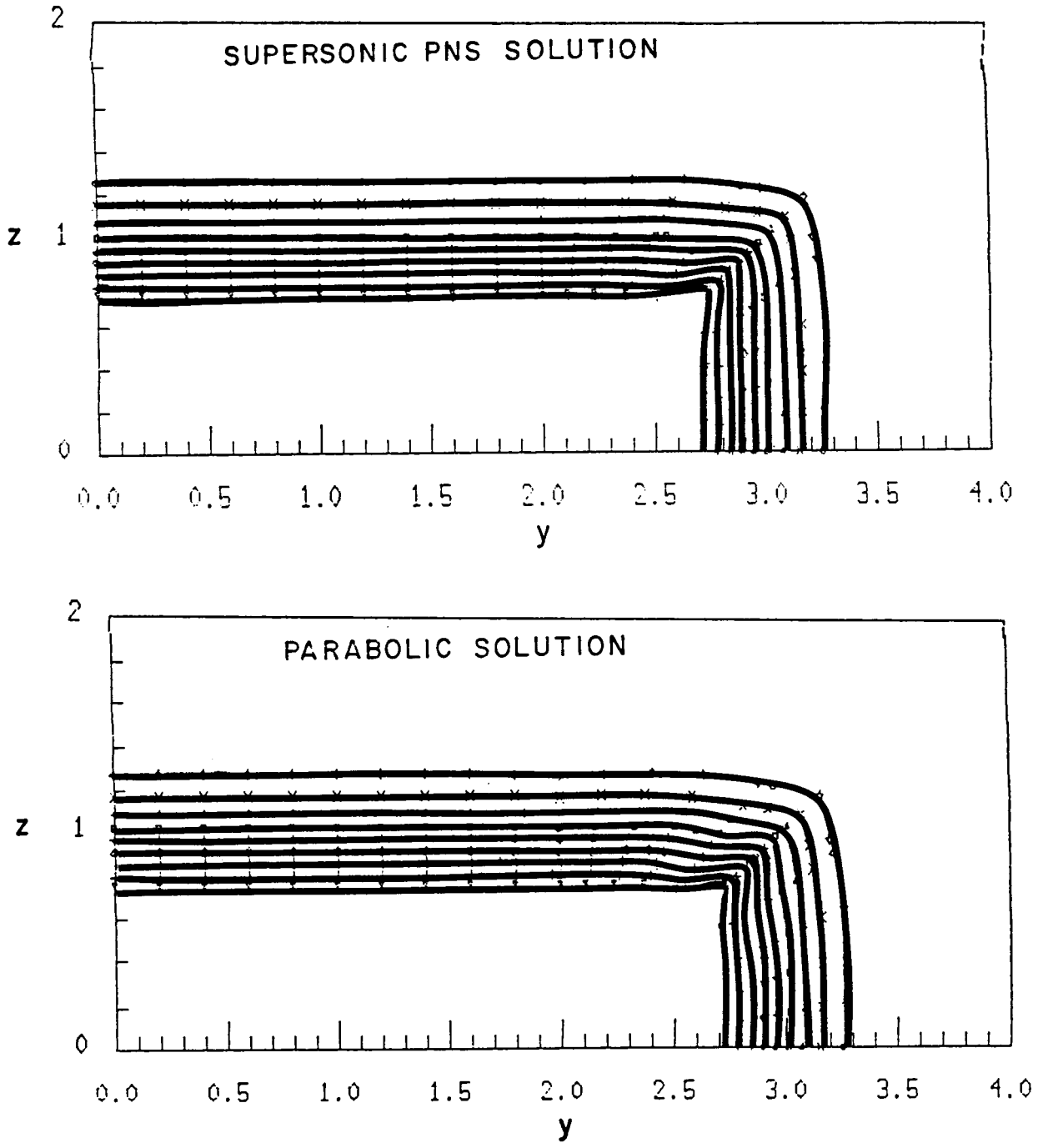

FIGURE 65. ϕ Cross-Flow Contours For 3/1 Rectangular Jet Problem, x = 20 Supersonic PNS vs. Parabolic Solutions.

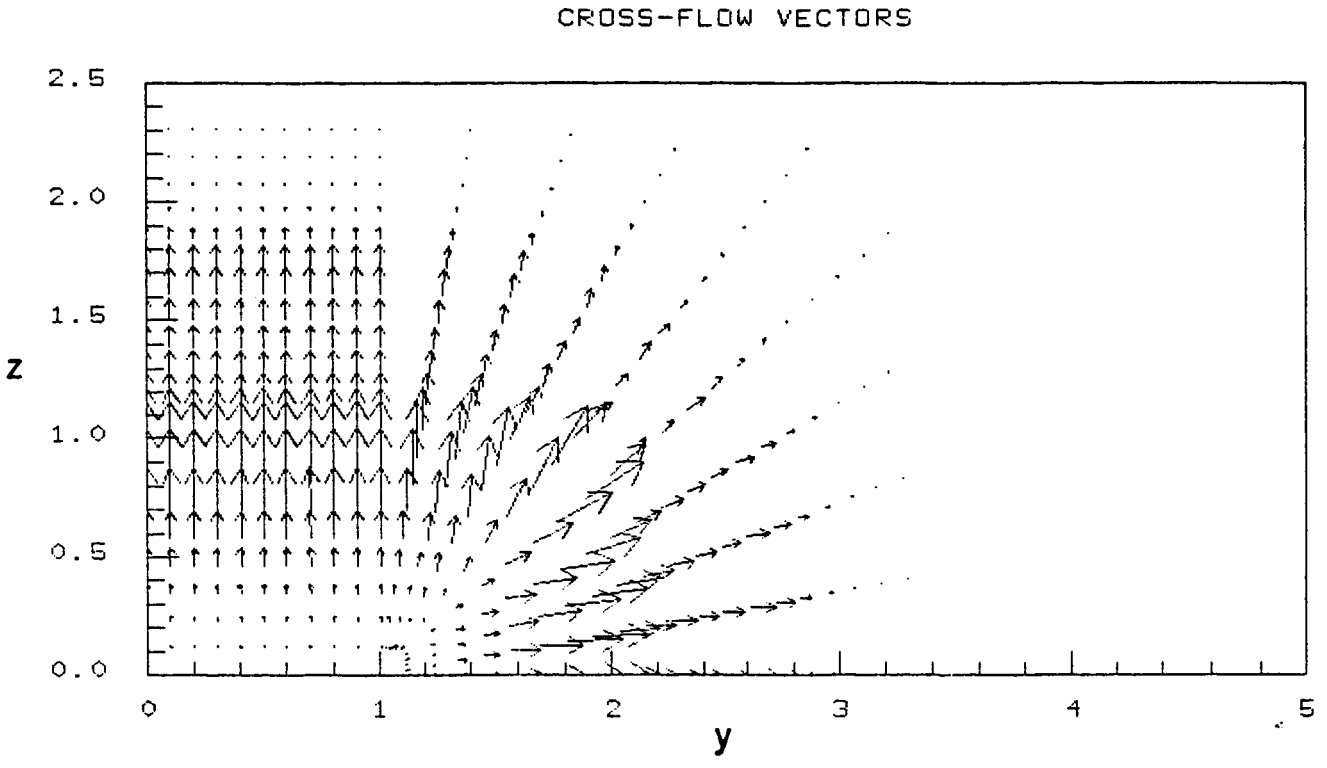

FIGURE 66. Cross-Flow Velocity Vector Field At x = 20 For 3/1 Rectangular Jet Problem, x = 20 Parabolic Run Option.

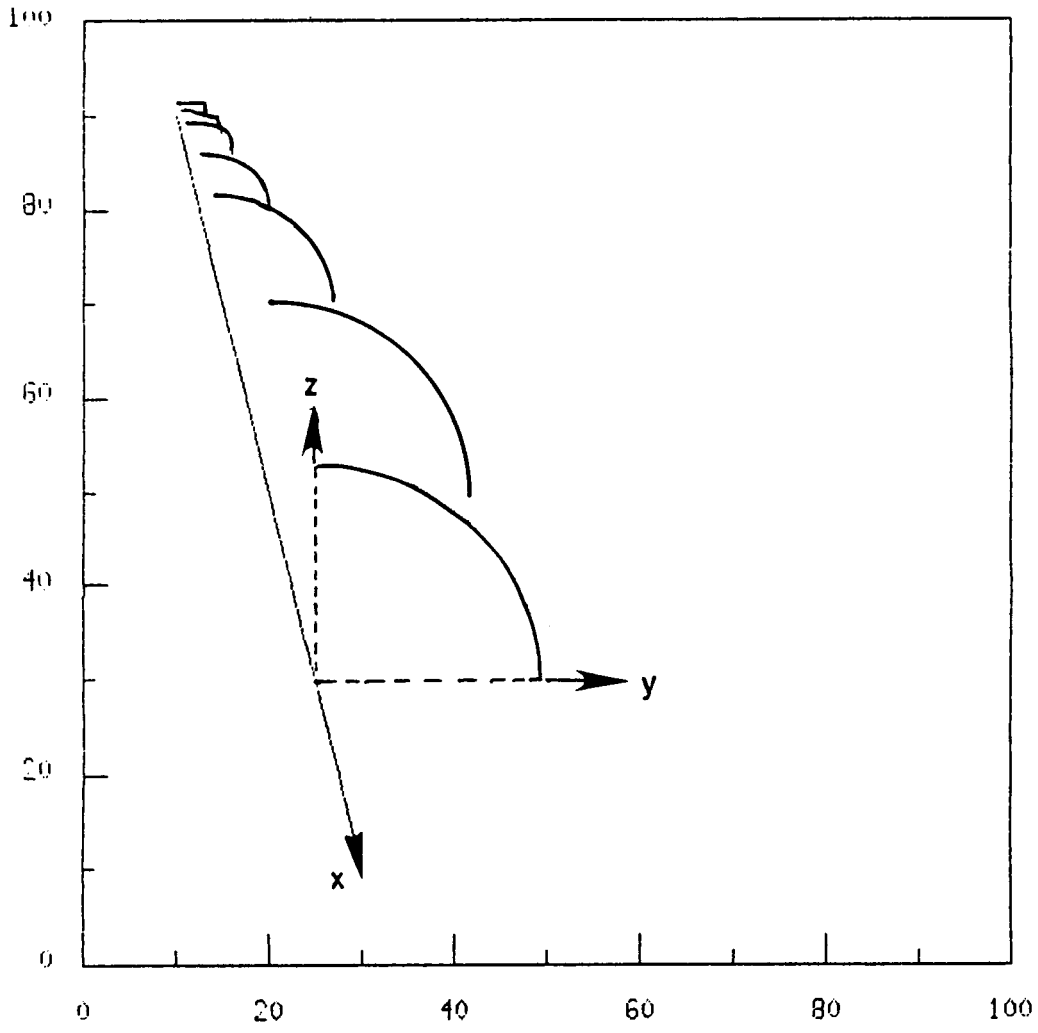

FIGURE 67. Evolution Of Jet Boundary Contours From Rectangular To Circular For 3/1 Rectangular Jet Problem.

5. NUMERICAL PROCEDURE FOR ANALYZING SUPERSONIC JETS EXHAUSTING INTO SUBSONIC EXTERNAL STREAMS AND NUMERICAL STUDIES

5.1 Review of 2D Numerics for Supersonic/Subsonic Jet Mixing Problem

The spatial marching PNS analysis of a supersonic jet exhausting into a subsonic external stream requires:

(1) switching the numerical algorithm from full PNS at supersonic jet grid points to parabolic or pressure-split PNS at subsonic jet grid points;

(2) matching the supersonic and subsonic PNS solutions at the jet sonic line; and,

(3) providing for a global pressure iterative methodology to account for the overall interaction of the jet and subsonic external flow.

At the 2D level, the above procedures have all been made operational. The analysis of the mixed supersonic/subsonic problem in the absence of global external flow interactions (e.g., the external pressure field is assumed to be constant) has been performed with the SCIPVIS model[1], and, numerous comparisons with the data of Seiner have been performed which demonstrate the viability of this approach (see refs. 2-5). A typical solution is exhibited in Figure 68 (from ref. 1) which shows the ability of SCIPVIS to accurately predict the complex jet pressure field. A key feature of SCIPVIS was the characteristic-based methodology developed to couple the supersonic and subsonic solutions at the jet sonic line as schematized in Figure 69. The coupling (at the grid point I*) is performed with the outer jet boundary pressure, $P_e(x)$, prescribed and a viscous-characteristic constraint just under the jet sonic line (along $\lambda+$) relating the supersonic pressure and flow angle. In SCIPVIS, the normal pressure variation across the subsonic outer layer is neglected and $P_e(x)$ is imposed at the sonic line yielding the flow angle there. Then, the variation in flow angle across the jet is obtained from the continuity equation yielding the entrainment (suction) velocity, $V_e(x)$, at the jet outer edge.

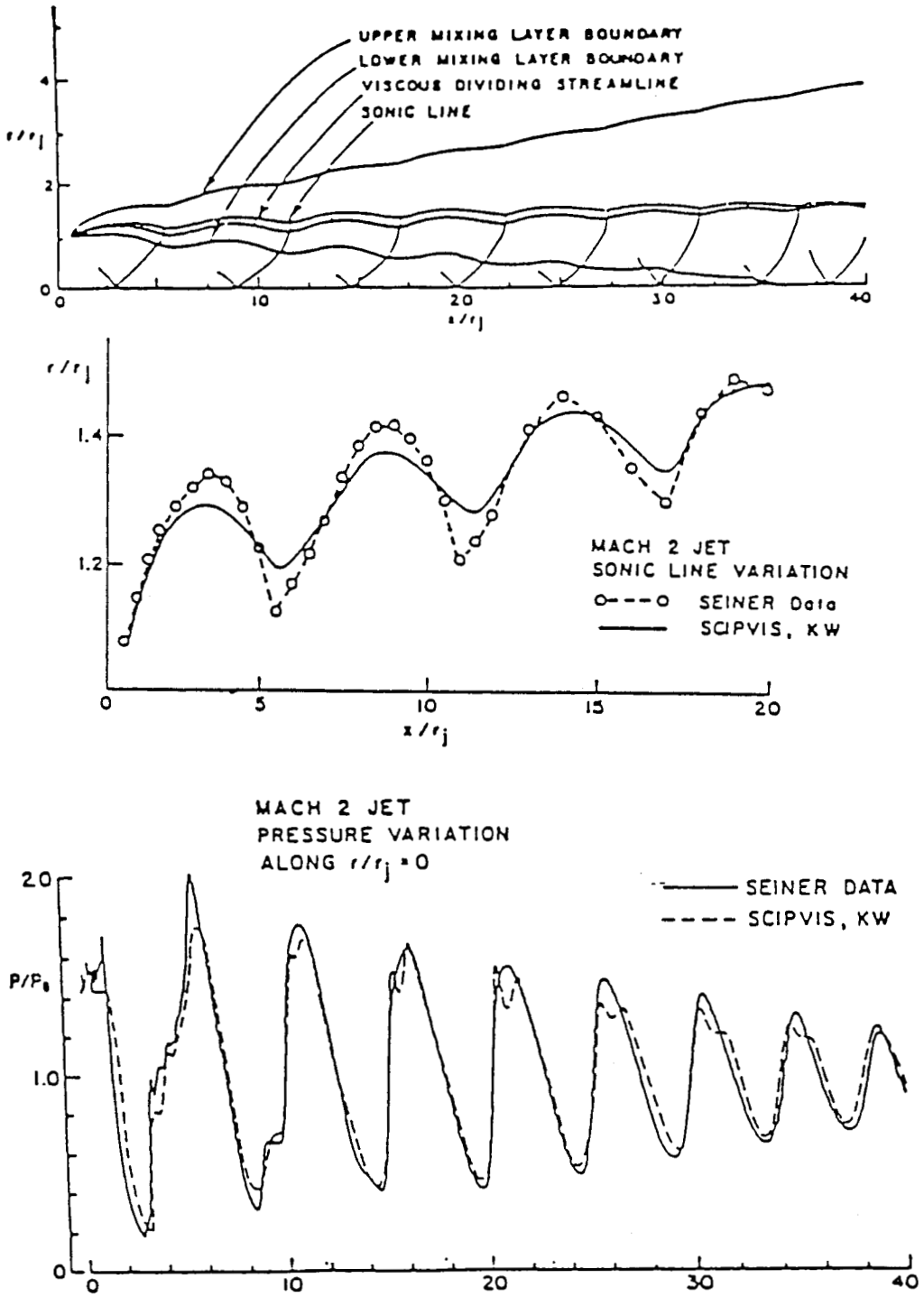

FIGURE 68. SCIPVIS Prediction Of Mach 2 Jet Into Still Air And Comparisons With Data Of Seiner (From Ref. 1).

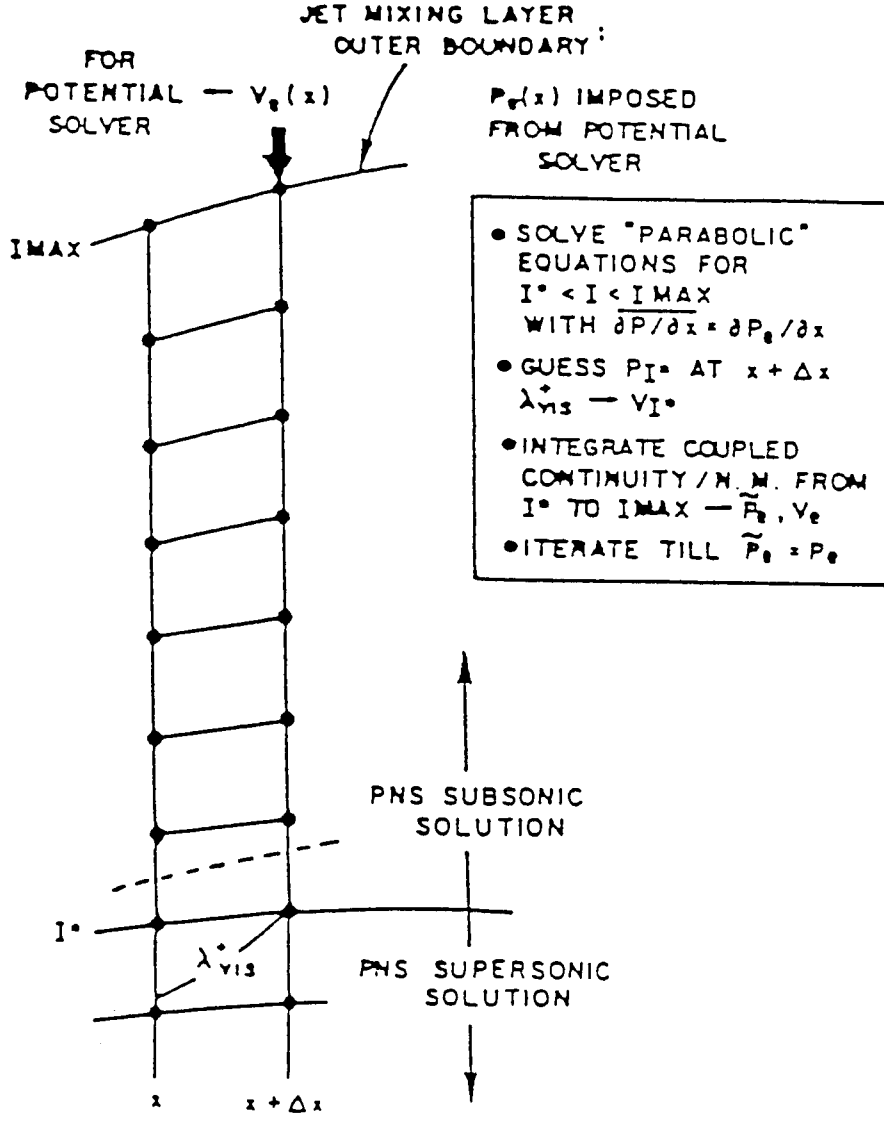

FIGURE 69. 2D Supersonic/Subsonic Coupling At Jet Sonic Line.

5.2 Nonadaptive Rectangular Matching Boundary Approach

For 3D jets, the coupling problem is complicated by the shape taken by the sonic line in the cross-flow plane, as well as by initial corner region vortical effects. In our initial work, mapped rectangular coordinates were employed and sonic line coupling was performed along the 'largest' embedded rectangle that could fit within the sonic line in the cross-flow plane (Fig. 70). The pressure along the matching boundary was lagged yielding V and W at all I* and J* matching points which served as inner boundary conditions for the subsonic coupled V-W cross-flow solution. The subsonic cross-flow solution was swept outward from the matching boundary to the outer boundary, with y and z sweeps independent of each other until the I*, J* matching point. The nested subsonic corner region (I > I*, J > J*) was treated using specialized coupled logic.

This approach was applied to the analysis of an underexpanded square jet exhausting into a subsonic stream. Reasonable results were obtained for the initial jet expansion (since the square grid coincided with the initial sonic line shape), but became quite poor when the reflected waves (which recompress the jet turning the stream surfaces inward) reached the now quasi-circular sonic line. The square representation of the sonic line artificially delayed the recompression waves from interacting with the corner region sonic line as shown in the sequence of cross-flow contours displayed in Figure 71. As exhibited, the initial expansion of the jet is well-predicted, but the recompression process (x > 4) leads to highly unrealistic cross-flow contours.

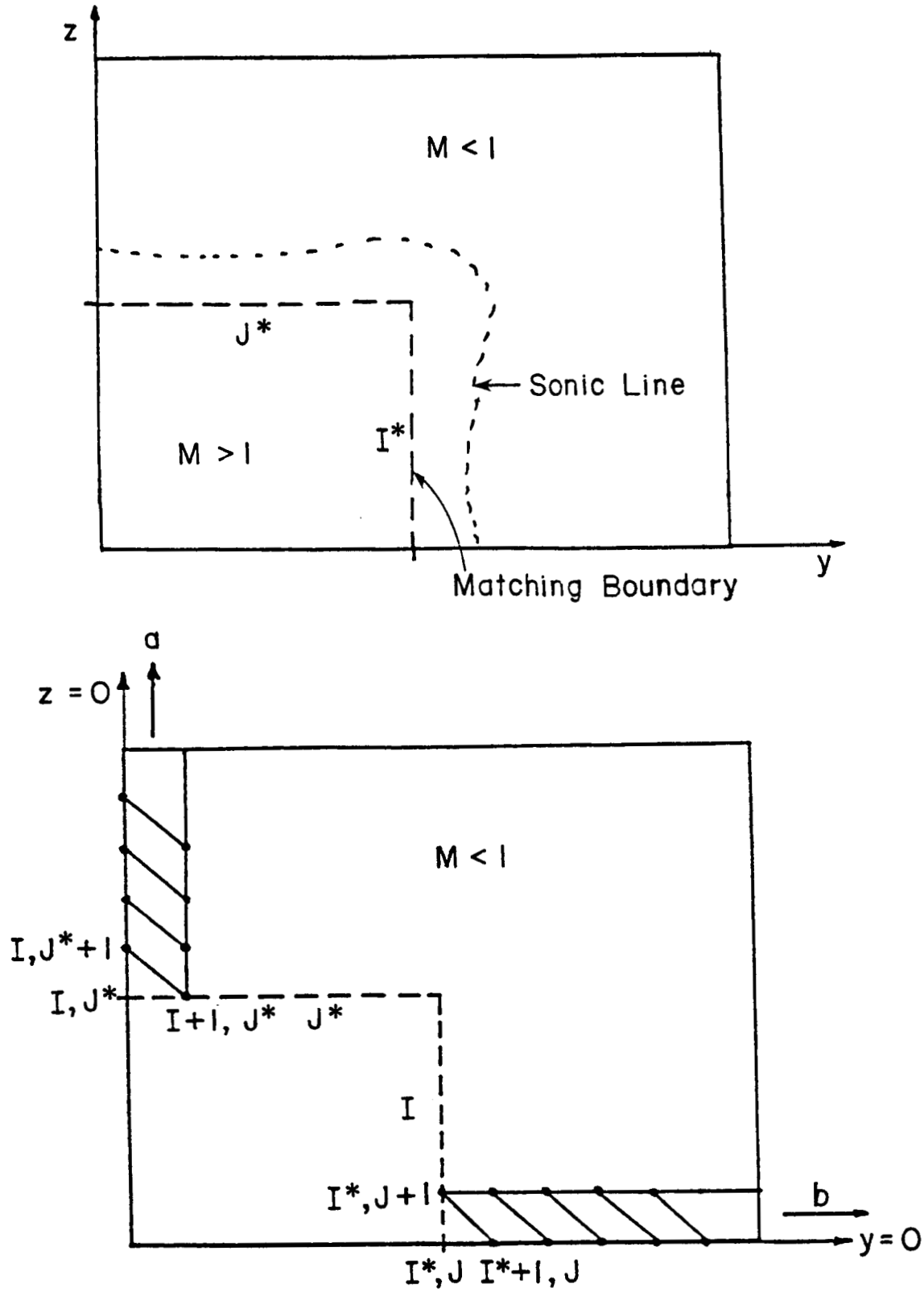

FIGURE 70. Rectangular Matching Boundary For Mixed Supersonic/Subsonic Problem.

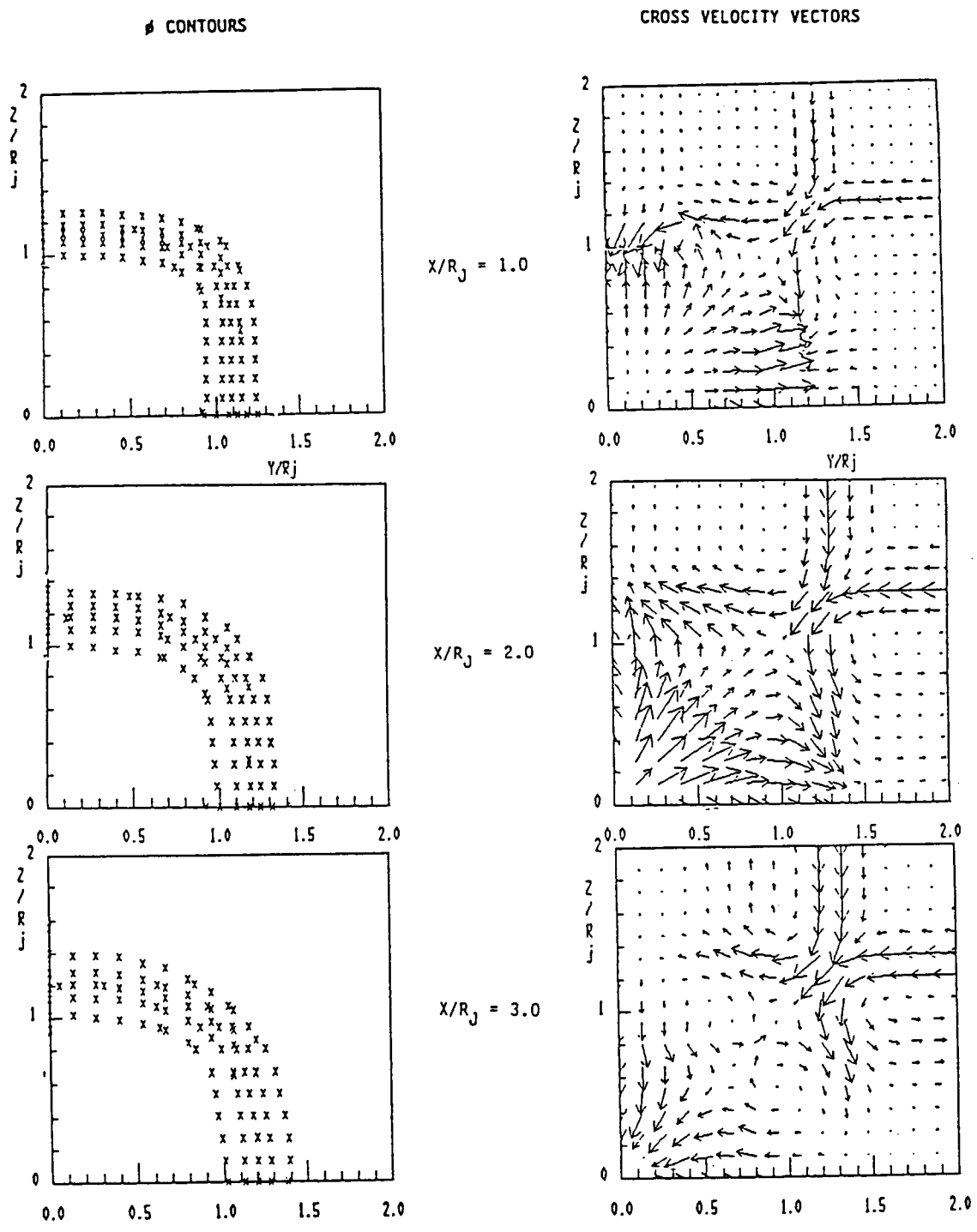

FIGURE 71. Species (ϕ) Contours And Cross-Flow Velocity Vectors For Underexpanded Square Jet Into Subsonic External Stream Using Version I Supersonic/Subsonic Coupling (Embedded Rectangle).

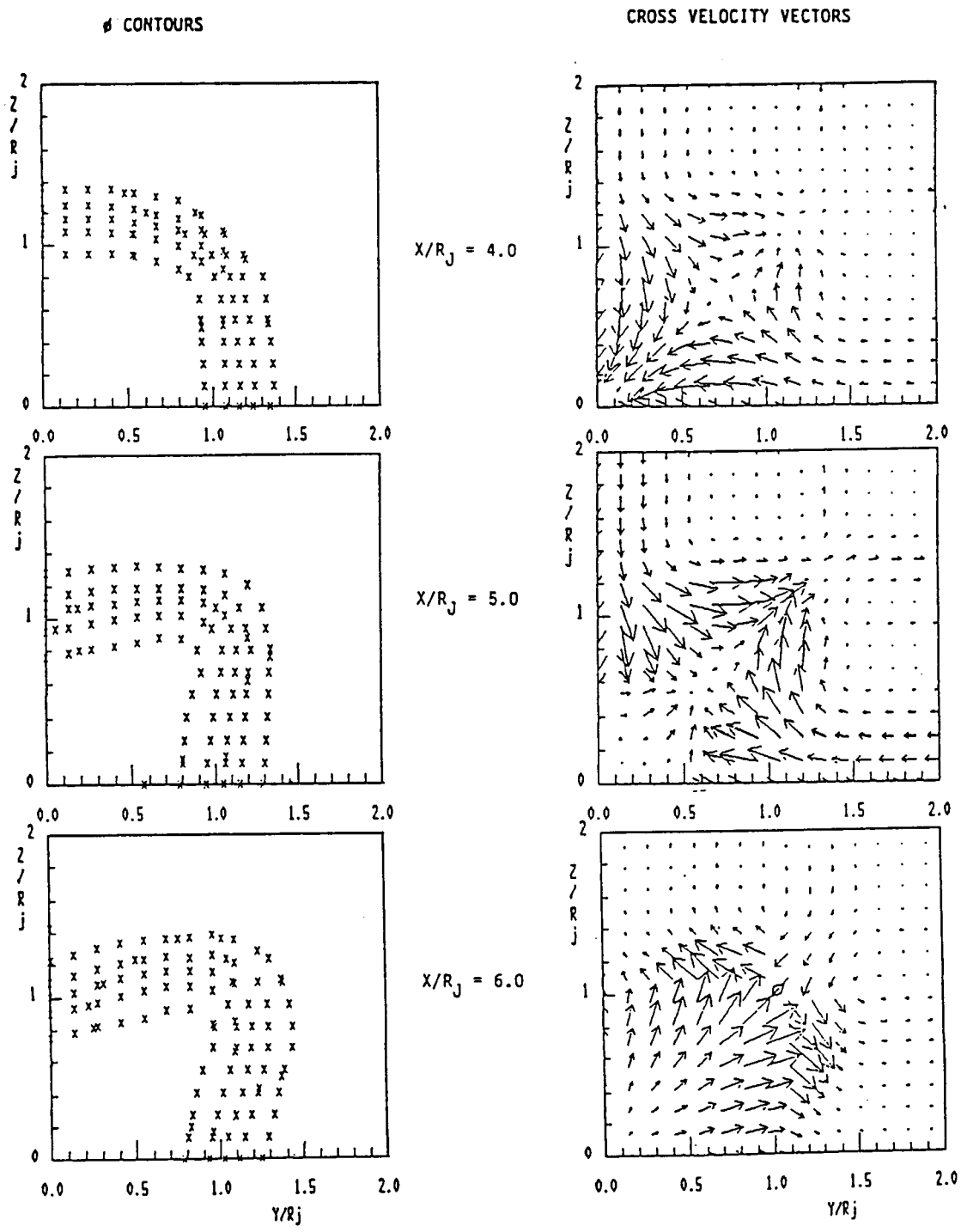

FIGURE 71 – CONT'D. Species (ø) Contours And Cross-Flow Velocity Vectors For Underexpanded Square Jet Into Subsonic External Stream Using Version I Supersonic/Subsonic Coupling (Embedded Rectangle).

5.3 Variable Rectangular Grid Matching Boundary Approach

To remedy this problem, a variable matching boundary which adapted itself to the sonic line cross-flow variation was implemented, still working in mapped rectangular coordinates (Figure 72). Using this approach, the matching logic at the sonic line is quite complex, and the solution of the coupled V-W subsonic cross-flow equations entails very cumbersome logic. Results using this adaptive approach are exhibited in Figure 73. The solution in the corner region ultimately goes unstable due to complexities in concurrently handling the initial subsonic corner-induced vortices and the reflected compression wave system.

5.4 Fully Adaptive Matching Boundary Approach

The current approach for dealing with this complex problem involves utilizing adaptive coordinates with the cross-flow directions aligned:

(1) along the jet entrainment (inflow/outflow) direction, essentially normal to the sonic line; and,

(2) normal to this direction and thus aligned with the sonic line and also normal to the plane/axis of symmetry.

In this approach, a parabolic procedure is employed for analyzing the subsonic region of the flow which neglects the momentum equation in the entrainment aligned direction. Results for an 8/1 velocity ratio balanced pressure square jet problem ($M_J = 2$, $T_3 = 2000$ °K; $M_E = 0.5$, $T_E = 500$ °K) performed with adaptive cylindrical coordinates are exhibited in the next several figures. The calculations were performed using a fully parabolic approach and the adaptive supersonic/subsonic PNS approach discussed here. Parabolic vs. PNS solution contours of ϕ and T in the jet symmetry plane are exhibited in Figures 74 and 75, respectively. Cross-flow contours of ϕ and T at x = 25 are compared in Figures 76 and 77. The 'crude' computational grid employed to perform this calculation is exhibited at x = 25 in Figure 78. Pressure contours at x = 25 are exhibited in Figure 79. Note the close similarity in ϕ contours showing that mixing processes are nearly identical, but, variations in T contours indicating the influence of the variable pressure field in the PNS case.

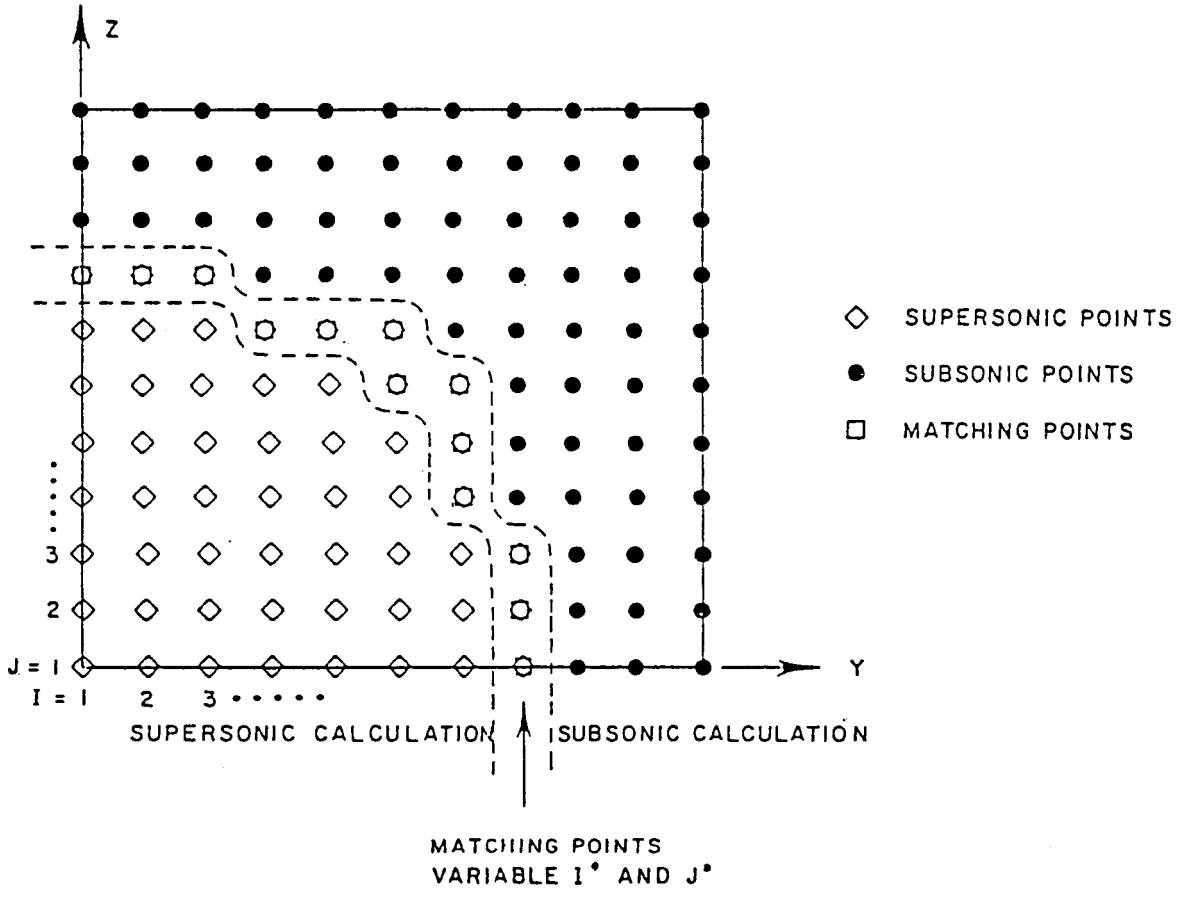

FIGURE 72. Variable Rectangular Grid Matching Boundary.

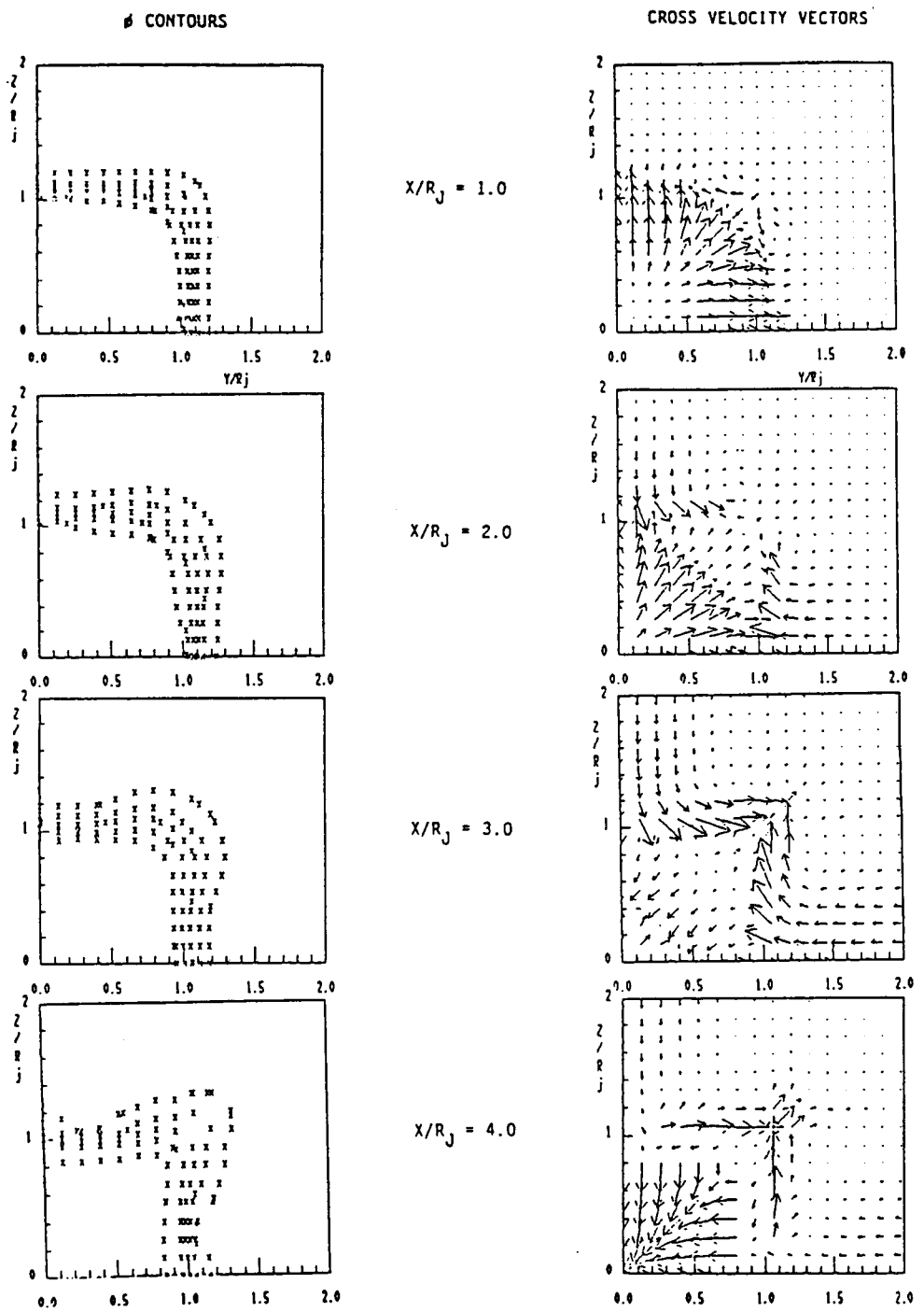

FIGURE 73. Species (ϕ) Contours And Cross-Flow Velocity Vectors For Underexpanded Square Jet Into Subsonic External Stream Using Version II Supersonic/Subsonic Coupling (Variable Grid Point).

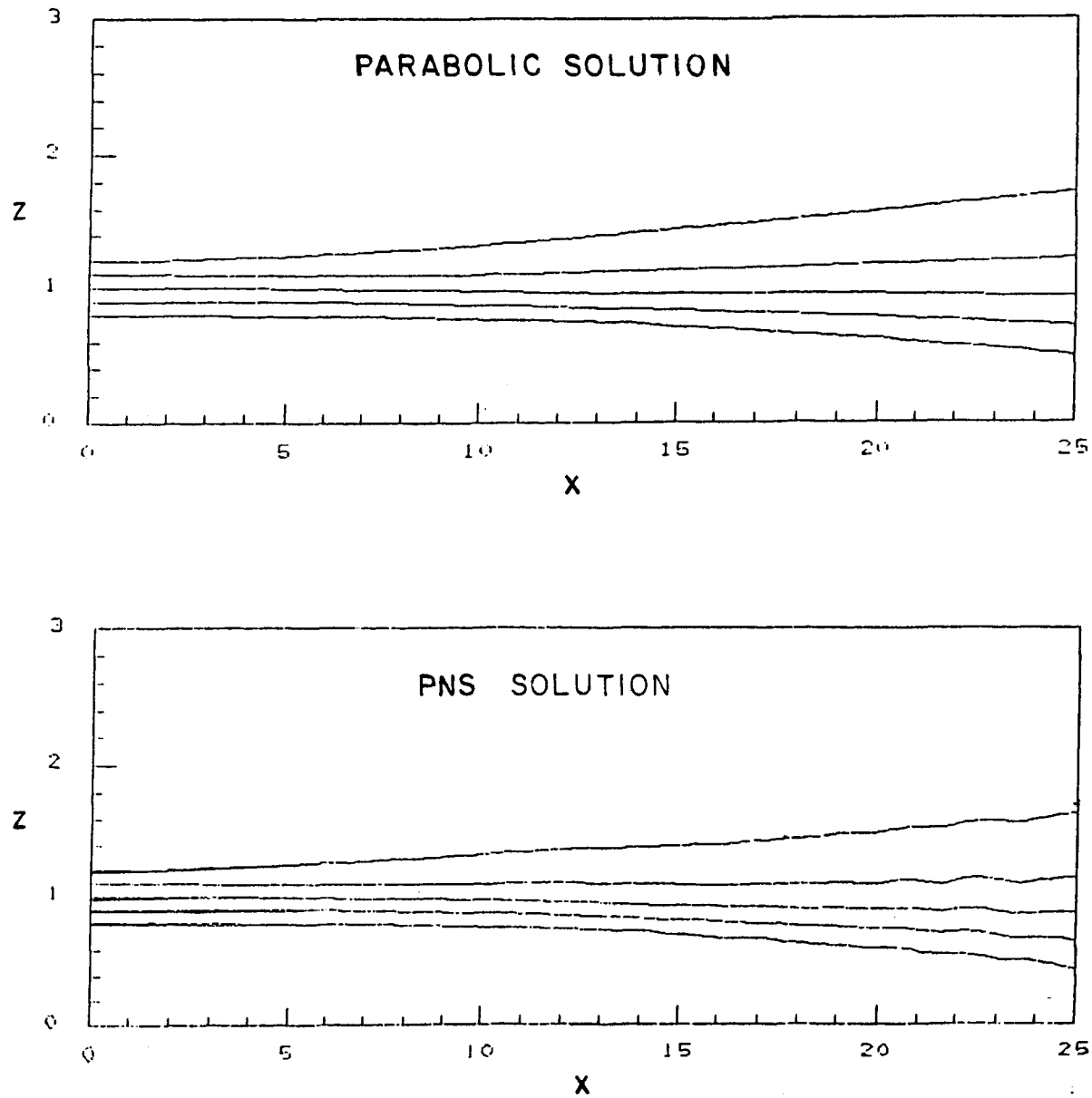

FIGURE 74. ϕ Contours In Symmetry Plane For Balanced Pressure Subsonic/ Supersonic Square Jet Problem.

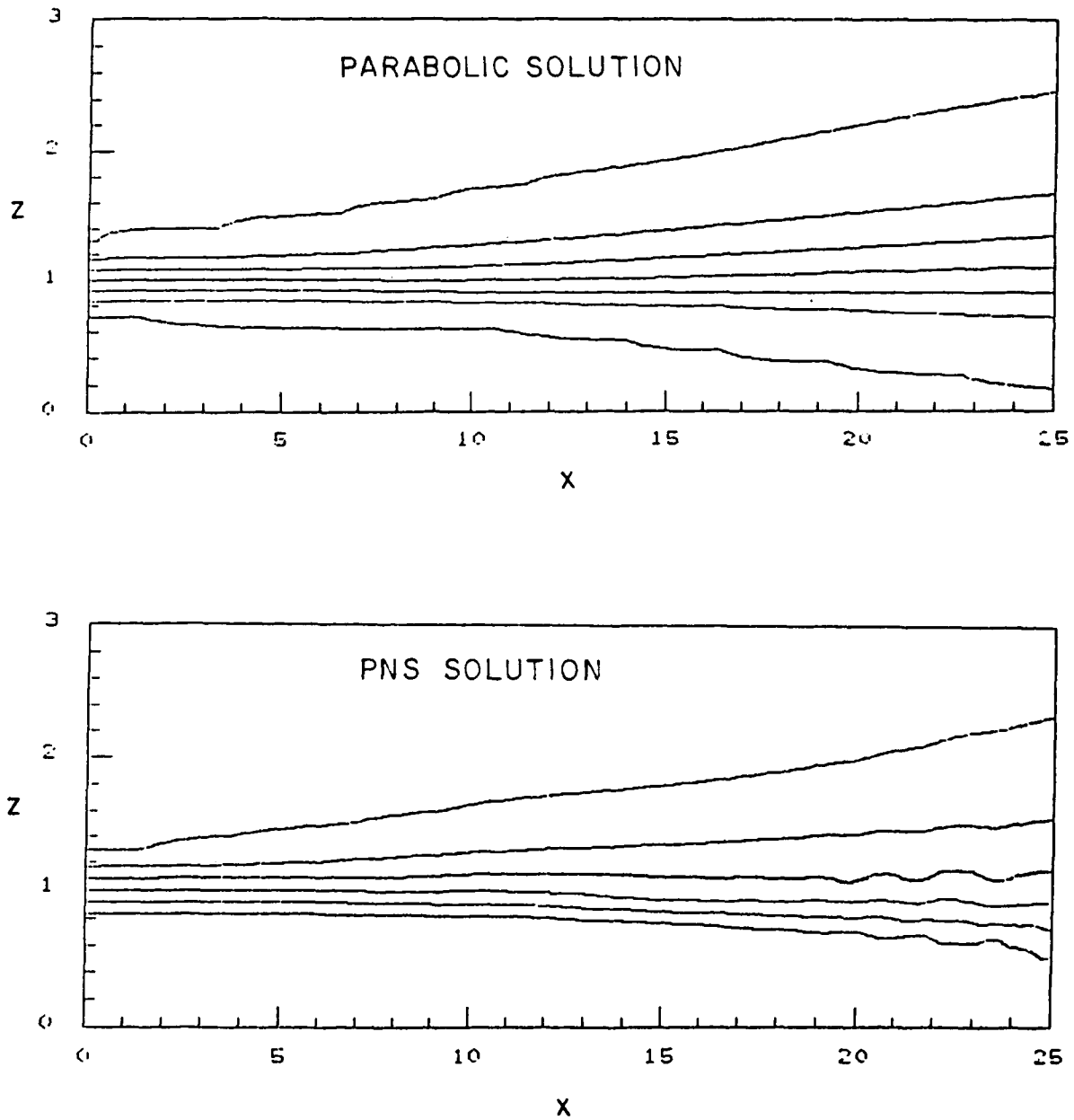

FIGURE 75. T Contours In Symmetry Plane For Balanced Pressure Subsonic/ Supersonic Square Jet Problem.

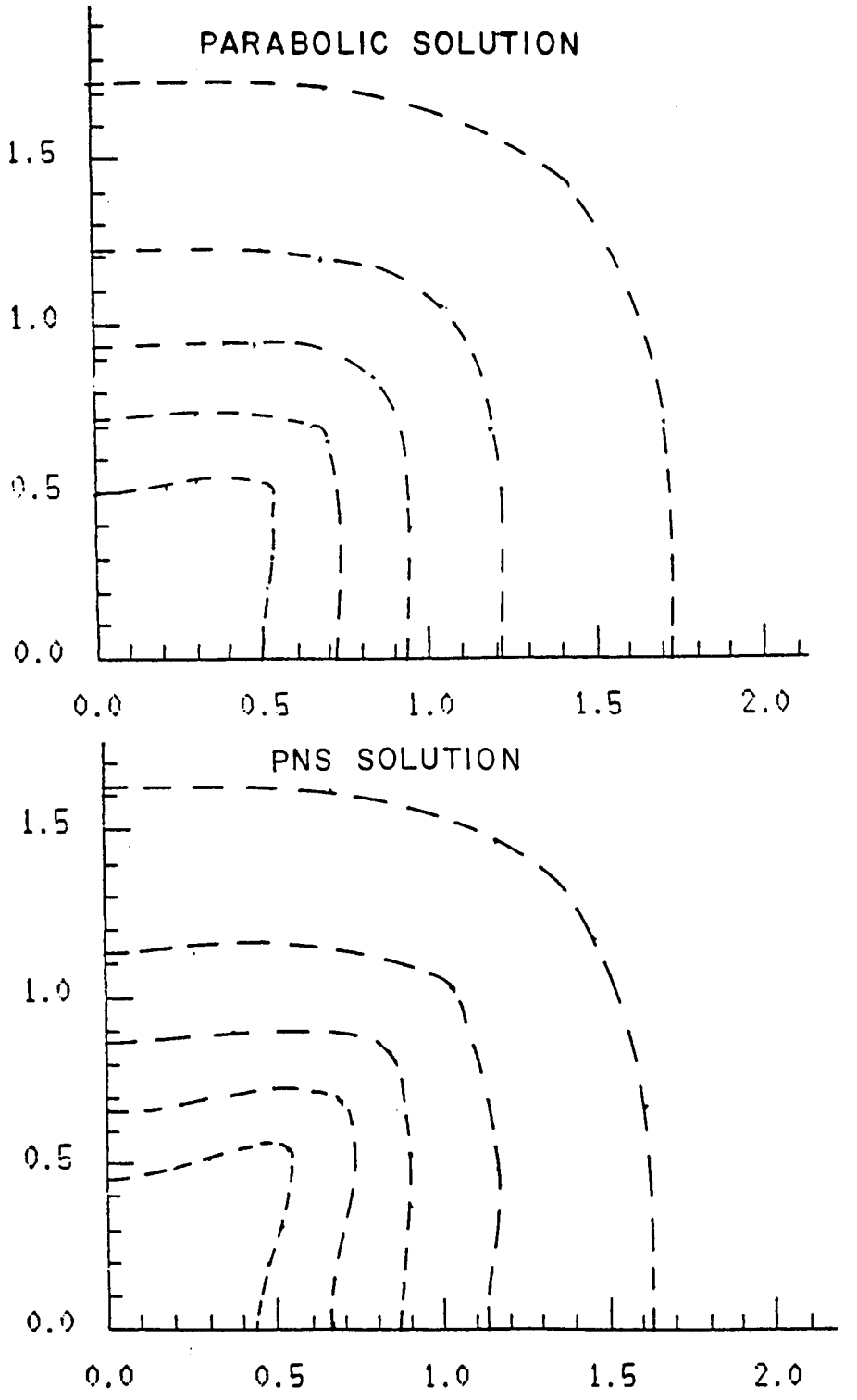

FIGURE 76. ϕ Contours At x = 25 For Balanced Pressure Subsonic/ Supersonic Square Jet Problem.

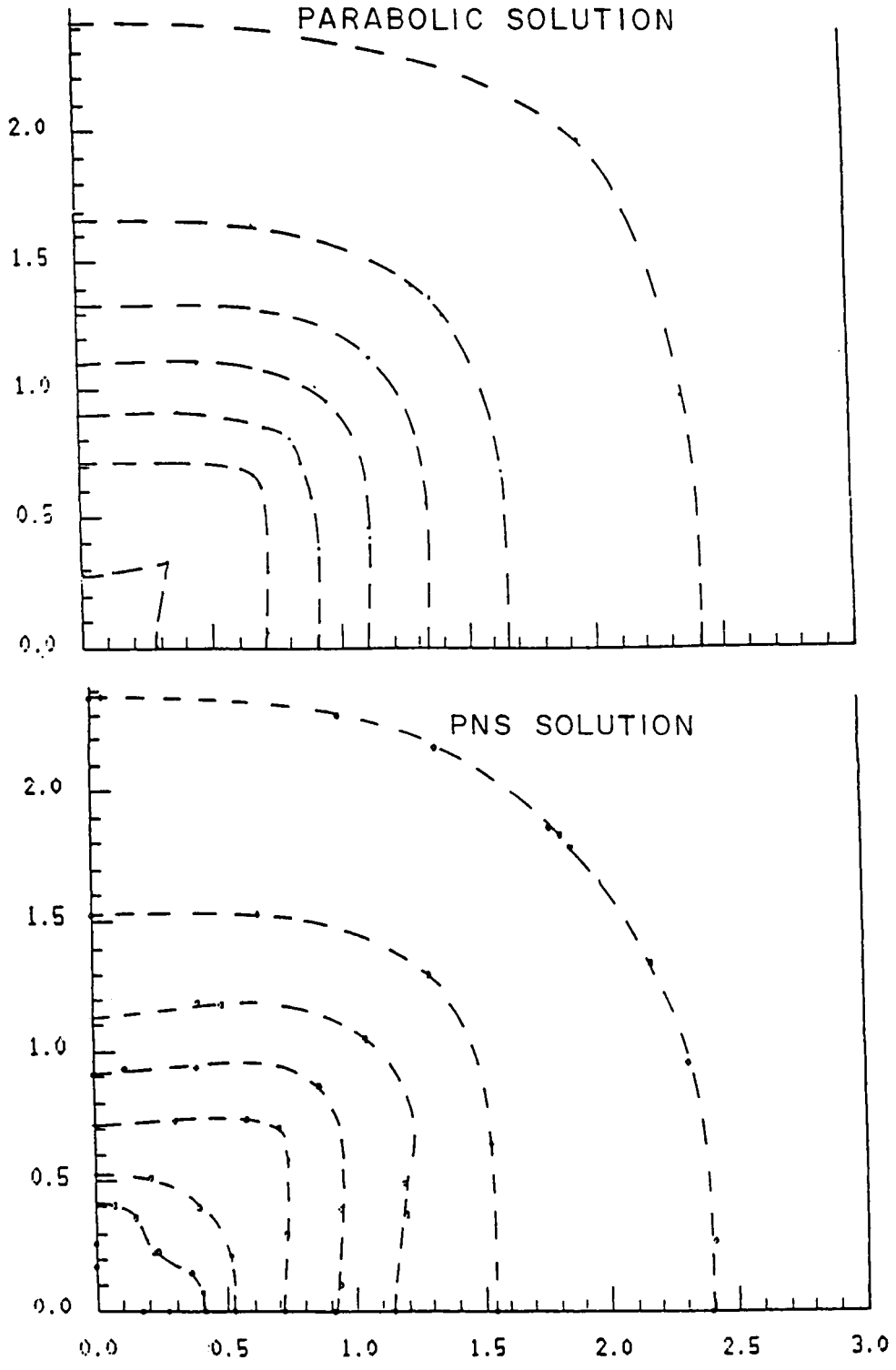

FIGURE 77. T Contours At x = 25 For Balanced Pressure Subsonic/ Supersonic Square Jet Problem.

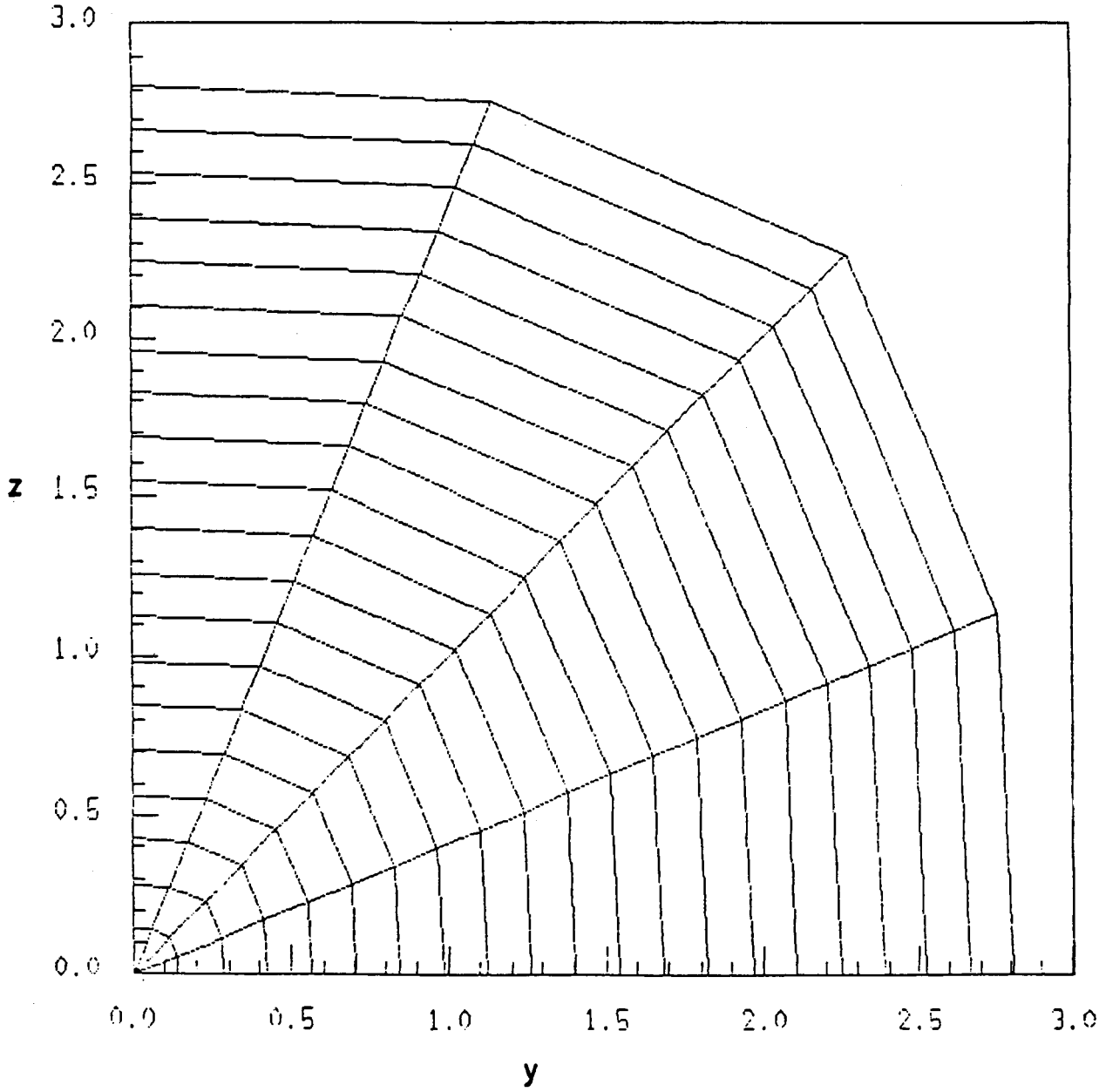

FIGURE 78. Adaptive Cylindrical Grid In Cross-Flow Plane At x = 25 For Balanced Pressure Square Jet Problem.

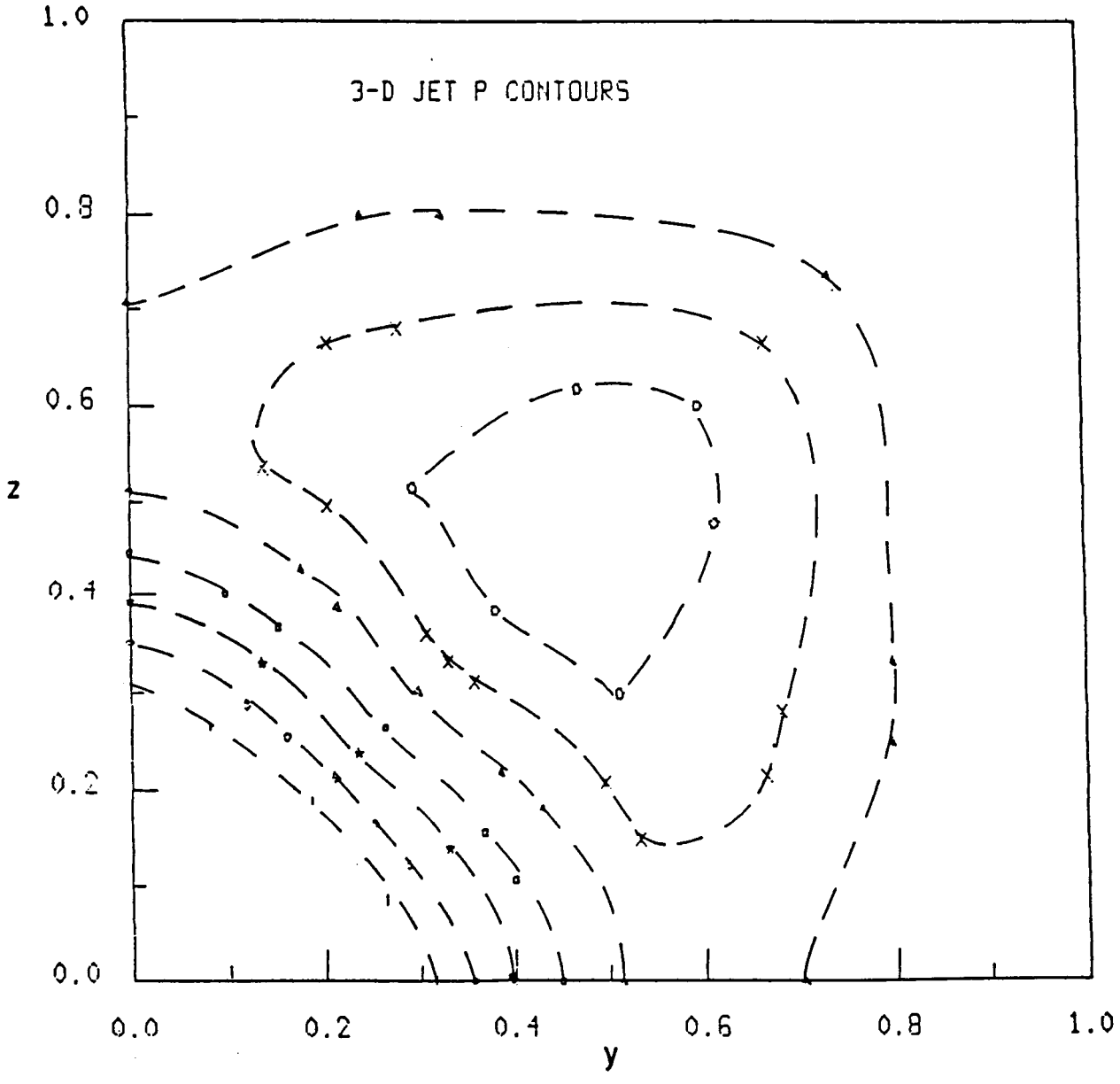

FIGURE 79. Perturbation Pressure Contours In Cross-Flow Plane At x = 25 For Balanced Pressure, Square Jet Problem.

Preliminary results for an underexpanded subsonic/supersonic square jet problem with conditions comparable to those of the Seiner case[1-5] (see Fig. 68) are exhibited in Figures 80 and 81. Figure 80 exhibits ϕ and P contours at x = 4. The predicted variation of pressure along the jet axis for the first shock cell is exhibited in Figure 81. To check out the code's performance, an attempt was made to analyze the above problem in the axisymmetric limit and compare it directly with SCIPVIS results. The 3D code utilized the same grid as SCIPVIS in each cross-flow plane, ϕ = constant. The 3D calculation was performed utilizing quarter plane symmetry employing five ϕ planes. Figure 82 compares SCIP3D predicted shear layer boundary contours (ϕ = 0.05 and 0.95) in the symmetry planes with corresponding SCIPVIS results. Figure 83 compares predicted centerline pressure variations. The comparisons indicate that further work is required to deal with near-axis effects in the 3D code to get the two solutions to agree more closely.

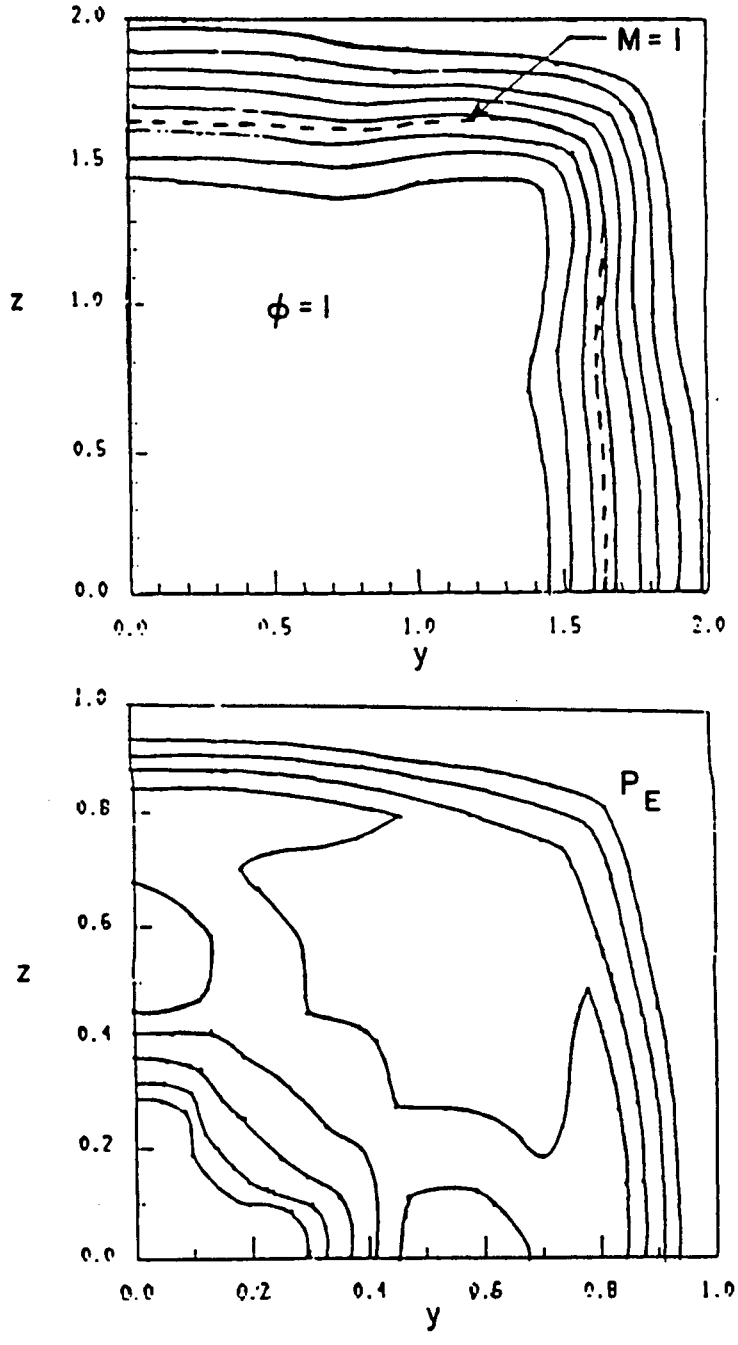

FIGURE 80. Contours Of ϕ And P For Underexpanded Subsonic/Supersonic Square Jet Problem.

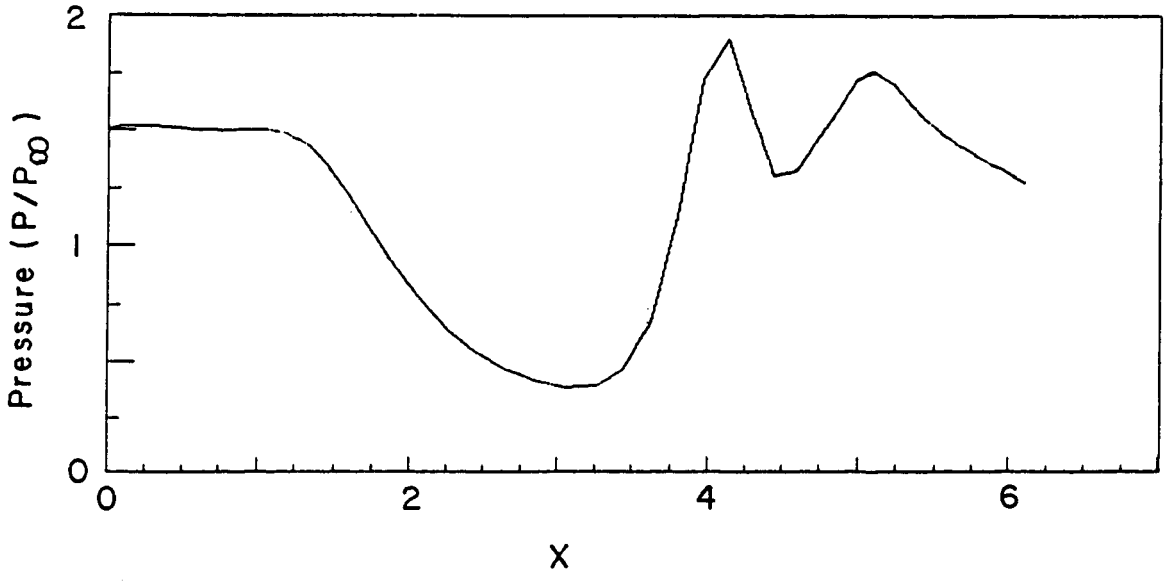

FIGURE 81. Pressure Variation Along Jet Axis For Underexpanded Subsonic/ Supersonic Square Jet Problem.

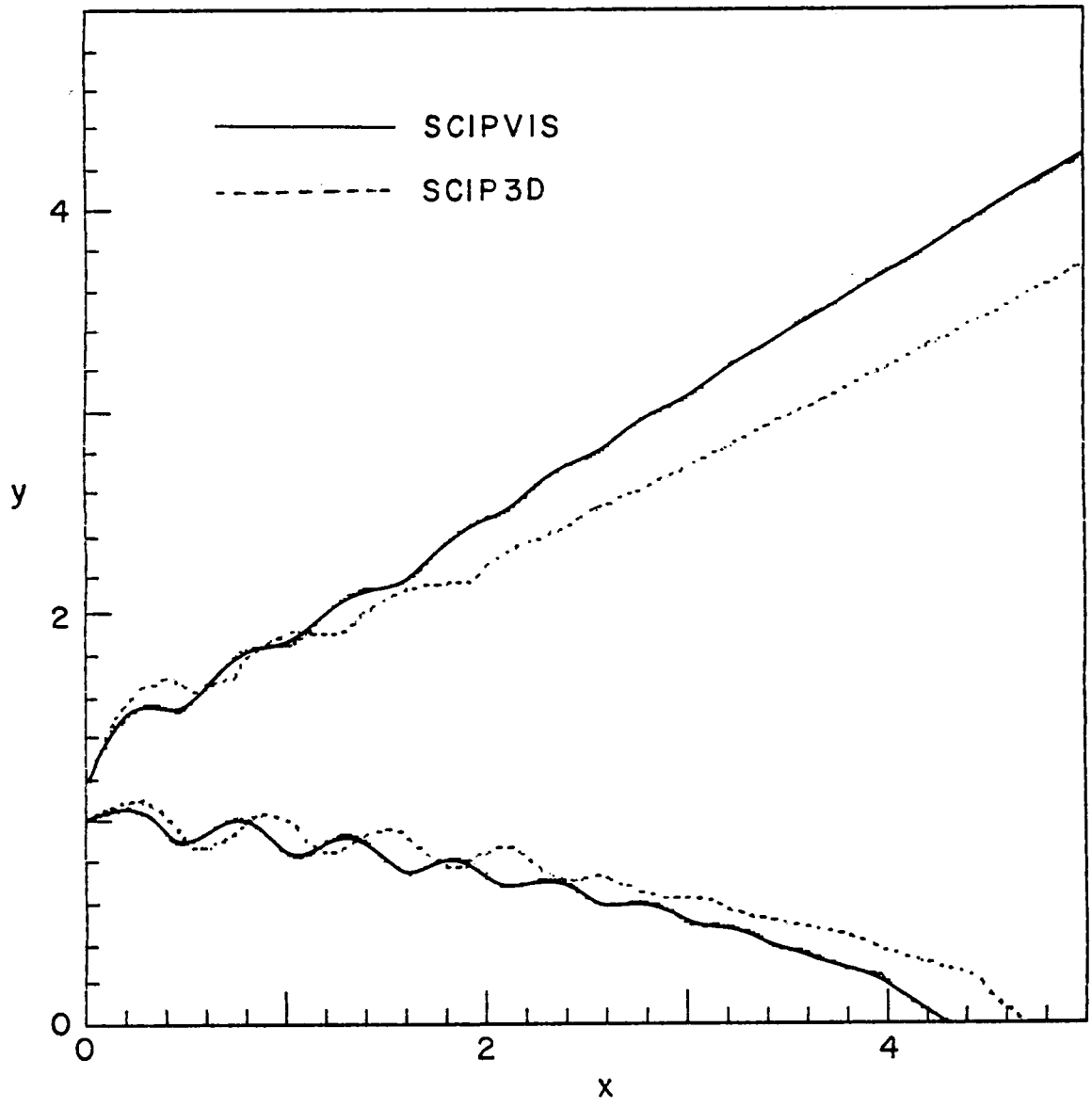

FIGURE 82. Comparison Of SCIP3D And SCIPVIS Predictions Of Shear Layer Boundaries For Underexpanded Axisymmetric Subsonic/Supersonic Jet Problem.

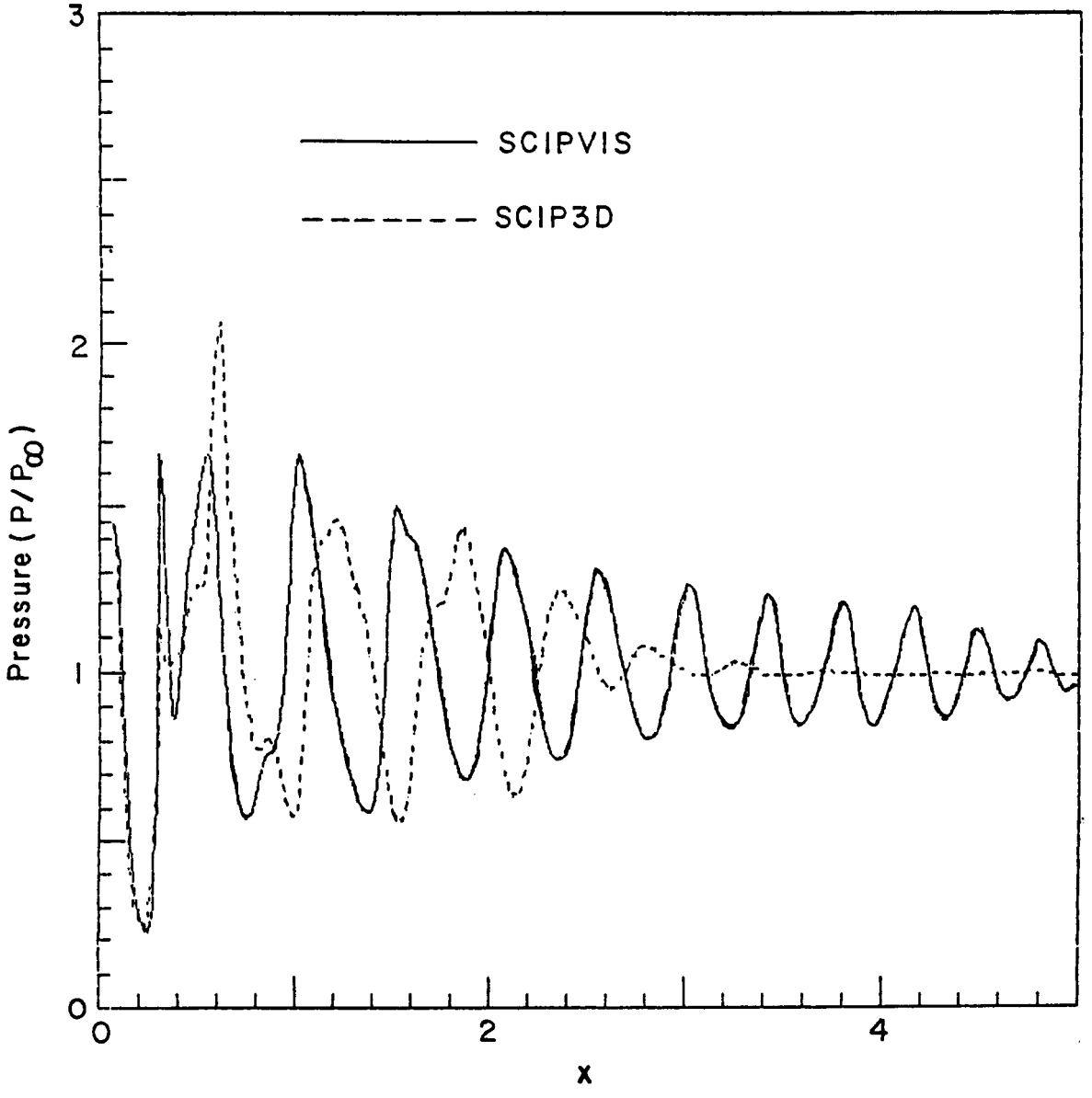

FIGURE 83. Comparison Of SCIP3D And SCIPVIS Predictions Of Jet Centerline Pressure Variations For Underexpanded Axisymmetric Subsonic/Supersonic Jet Problem.

6. SUMMARY

The SCIP3D 3D PNS jet mixing model and its application to a variety of rectangular jet mixing problems have been described in this report. For fully supersonic free jet problems (supersonic jet into supersonic external stream), the model has been demonstrated to predict plume flowfields for mildly underexpanded cases, and can be used to support plume related engineering studies at a research code level. The SCIP3D model also has current applicability to supersonic ducted problems (e.g., 3D nozzles/ diffusers and ducted jet mixing problems) but lacks the ability to resolve the near-wall boundary layer due to the explicit numerics utilized.

An extended version of SCIP3D (entitled SCHNOZ3D) has been developed for applications to scramjet propulsion problems. SCHNOZ3D contains generalized finite-rate chemistry capabilities and has been applied to scramjet combustor and nozzle/plume flowfields. Features and applications are to be reported in the Fourth National Aerospace Plan Tech Mat Symposium, Monterey, CA, February 1988 and the 17th JANNAF Plume Technology Symposium, NASA/LRC, Hampton, VA, April 1988. Exploratory work to extend this model to analyze the near-wall boundary layer is in progress utilizing a time-iterative procedure.

With regard to the analysis of supersonic jets exhausting into a subsonic external stream, the current noniterative methodology requires gridding which adapts to the sonic line shape in the cross-flow plane. Successful runs have only been performed by invoking simplifying assumptions for the cross-flow pressure variation in subsonic regions (e.g., $P = P(x)$ only). It appears that the noniterative methodology is quite cumbersome to deal with and that efforts should focus on time-iterative methodology on a plane to plane basis (e.g., in a spatial marching mode of operation with upstream influence effects suppressed). Other recommended upgrades to SCIP3D would include casting the equations in generalized coordinates and incorporating adaptive procedures to pack grid points into shear layer regions. Upgrading turbulence models from the two-equation level to the multi-scale or algebraic Reynolds stress level would also appear requisite to deal with vortical aspects of 3D mixing. This should be followed by a detailed validation study using the available rectangular jet mixing data base.

7. REFERENCES

1. Dash, S.M. and Wolf, D.E., 'Fully-Coupled Analysis of Jet Mixing Problems, Part I: Shock-Capturing Model, SCIPVIS', NASA CR-3761, January 1984.

2. Dash, S.M. and Wolf, D.E., 'Interactive Phenomena in Supersonic Jet Mixing Problems, Part I: Phenomenology and Numerical Modeling Techniques', AIAA Journal, Vol. 22, July 1984, pp. 905-913.

3. Dash, S.M. and Wolf, D.E., 'Interactive Phenomena in Supersonic Jet Mixing Problems, Part II: Numerical Studies', AIAA Journal, Vol. 22, October 1984, pp. 1395-1404.

4. Dash, S.M., Wolf, D.E. and Seiner, J.M., 'Analysis of Turbulent Under-Expanded Jets - Part I: Parabolized Navier-Stokes Model, SCIPVIS', AIAA Journal, Vol. 23, April 1985, pp. 505-514.

5. Seiner, J.M., Dash, S.M. and Wolf, D.E., 'Analysis of Turbulent Under-Expanded Jets - Part II: Shock Noise Features Using SCIPVIS', AIAA Journal, Vol. 23, May 1985, pp. 669-677.

6. Dash, S.M. and Beddini, R.A., 'Viscous/Inviscid Analysis of Curved Wall Jets: Part 2: Viscous Pressure Split Model (SPLITWJET)', Science Applications International Corporation, Princeton, NJ, SAIC/PR TR-7, November 1982.

7. Dash, S.M., Beddini, R.A., Wolf, D.E. and Sinha, N., 'Viscous/Inviscid Analysis of Curved Sub- or Supersonic Wall Jets', AIAA Journal, Vol. 23, January 1985, pp. 12-13.

8. Dash, S.M. and Sinha, N., 'Noniterative Cross-Flow Integration for the Pressure-Split Analysis of Subsonic Mixing Layer Problems', AIAA Journal, Vol. 23, January 1985, pp. 183-185.

9. Dash, S.M., Sinha, N. and York, B.J., 'Implicit/Explicit Analysis of Interactive Phenomena in Supersonic, Chemically-Reacting, Mixing and Boundary Layer Problems', AIAA Paper 85-1717, Cincinnati, OH, July 1985.

10. Dash, S.M., 'Exhaust Plumes and Their Interaction With Missile Airframes', Tactical Missile Aerodynamics, Vol. 104, Progress in Aeronautics ed. J.N. Nielson and M.J. Hemsch, AIAA, New York, 1986, Chapter XVII, pp. 778-851.

11. Dash, S.M., 'Recent Developments in the Modeling of High Speed Jets, Plumes and Wakes - Invited Survey Paper', AIAA Paper 85-1616, Cincinnati, OH, July 1985.

12. Dash, S.M., Wolf, D.E., Sinha, N., and Pergament, H.S., 'Hypersonic Re-Entry Wake Model,' Science Applications International Corporation, Princeton, NJ, SAIC/PR TR-28, March 1985.

13. Taylor, M.W., Coirier, W.J., Dash, S.M., Sinha, N. and Pergament, H.S., 'Thrusted Re-Entry Vehicle (TRV) Wake Model - Final Technical Report and Program Users Manual', Science Applications International Corporation, Princeton, NJ, SAIC/PR TR-62, June 1987.

14. Sinha, N. and Dash, S.M., 'Overlaid Approach for Missile Base Flow Analysis at Supersonic Velocities', AIAA Paper 85-1673, Cincinnati, OH, July 1985.

15. Dvorak, F.A., Strash, D.J., York, B.J. and Dash, S.M., 'Improved Algorithms for Circulation-Control Airfoils in Transonic Flow', AIAA Paper 87-0154, Reno, NV, January 1987.

16. Dash, S.M., York, B.J., Sinha, N. and Dvorak, F.A., 'Wall Jet Analysis for Circulation-Control Aerodynamics: Part I - Fundamental CFD and Turbulence Modeling Concepts,' Proceedings of Circulation Control Workshop, 1986, NASA CP 2432, 1987, pp. 23-70.

17. Dvorak, F.A. and Dash, S.M., 'Wall Jet Analysis for Circulation-Control Aerodynamics: Part II - Zonal Modeling Concepts for Wall Jet/Potential Flow Coupling', Proceedings of Circulation Control Workshop, 1986, NASA CP 2432, 1987, pp. 165-182.

18. Sinha, N. and Dash, S.M., 'Parabolized Navier-Stokes Analysis of Ducted Turbulent Mixing Problems with Finite-Rate Chemistry,' AIAA Paper 86-0004, Reno, NV, January 1986.

19. Sinha, N. and Dash, S.M., 'Analysis of Aerospace Vehicle Scramjet Propulsive Flowfields: 2D Combustor Code Development - Phase I', Science Applications International Corporation, Princeton, NJ, SAIC/PR TR-73, Feb. 1988.

20. Wolf, D.E., Lee, R.A. and Dash, S.M., 'Parabolized Navier-Stokes Analysis of Scramjet Hypersonic Nozzle Flowfields', AIAA Paper 87-1897, San Diego, CA, June - July 1987.

21. Wolf, D.E. and Lee, R.A., 'Preliminary User Manual For Hypersonic Scramjet Nozzle Code, SCHNOZ', Science Applications International Corporation, Princeton, NJ, SAIC/PR TR-44, March 1987.

22. Dash, S.M., Sinha, N., Wolf, D.E. and York, B.J., 'Computational Models for the Analysis/Design of Hypersonic Scramjet Components, Part I: Combustor and Nozzle Models', AIAA Paper 86-1595, Huntsville, AL, June 1986.

23. Krawczyk, W.J., Rajendran, N., Harris, T.B., York, B.J. and Dash, S.M., 'Computational Models for the Analysis/Design of Hypersonic Scramjet Components, Part II: Inlet and Ramp/Forebody Models', AIAA Paper 86-1596, Huntsville, AL, June 1986.

24. Dash, S.M., Wolf, D.E., and Sinha, N., 'Parabolized Navier-Stokes Analysis of Three-Dimensional Supersonic and Subsonic Jet Mixing Problems', AIAA Paper 84-1525, Snowmass, CO, June 1984.

25. Dash, S.M., Wolf, D.E., Sinha, N. and Lee, S.H., 'Progress in the Development of Parabolized Navier-Stokes Methodology for Analyzing Propulsive Jet Mixing Problems', AIAA Paper 86-1115, Atlanta, GA, May 1986.

26. Dash, S.M., Wolf, D.E., Sinha, N. and Lee, S.H., 'Parabolized Navier-Stokes Analysis of Three-Dimensional Plume Flowfields', JANNAF 15th Plume Technology Meeting, CPIA Pub. 426, May 1985, pp. 173-196.

27. Dash, S.M., Wolf, D.E. and Sinha, N., 'Parabolized Navier-Stokes Analysis of Three-Dimensional Supersonic and Subsonic Mixing Problems', AIAA J., Vol. 24, August 1986, pp. 1252-3.

28. Launder, B.E., Morse, A., Rodi, W., Spalding, D.B., 'Prediction of Free Shear Flows: A Comparison of Six Turbulence Models,' in Free Turbulent Shear Flows, NASA SP-321, Vol. I, July 1972, pp. 361-426.

29. Spalding, D.B., 'Concentration Fluctuations in a Round Turbulent Free Jet', Chemical Engineering Science, Vol. 26, 1971, pp. 95-107.

30. Dash, S.M. and DelGuidice, P.D., 'Analysis of Three-Dimensional Ducted and Exhaust Plume Flowfields', AIAA Journal, Vol. 16, Aug. 1978, pp. 823-830.

31. Dash, S.M. and Pergament, H.S., 'A Computational Model for the Prediction of Jet Entrainment in the Vicinity of Nozzle Boattails (The BOAT Code)', NASA CR-3075, December 1978.

32. Dash, S.M., Wilmoth, R.G. and Pergament, H.S., 'An Overlaid Viscous/Inviscid Model for the Prediction of Nearfield Jet Entrainment', AIAA Journal, Vol. 17, September 1979, pp. 950-958.

33. Abbett, M.J., 'Boundary Condition Calculation Procedures for Inviscid Supersonic Flowfields', Proc. AIAA Comp. Fluid Dynamic Conf., July 1973, pp. 153-172.

34. Dash, S.M. and DelGuidice, P.D., 'Numerical Methods for the Calculation of Three-Dimensional Nozzle Exhaust Flow Fields', Aerodynamic Analyses Requiring Advanced Computers, NASA SP-347, Part I, March 1975, pp. 659-701.

35. Dash, S.M. and DelGuidice, P.D., 'Computational Models for the Analysis of Three-Dimensional Internal and Exhaust Plume Flowfields', JANNAF 10th Plume Technology Meeting, CPIA Pub. 291, Vol. I, September 1977, pp. 293-342.

36. Chang, I.S., 'Three Dimensional Supersonic Internal Flows', AIAA Paper 76-423, July 1976.

37. Spradley, L.W., Anderson, P.G. and Pearson, M.L., 'Computation of Three-Dimensional Nozzle-Exhaust Flow Fields with the GIM Code', NASA CR-3042, Aug. 1978.

38. Patankar, S.V. and Spalding, D.B., 'A Calculational Procedure for Heat, Mass, and Momentum Transfer in Three-Dimensional Parabolic Flows', Int. J. Heat and Mass Transfer, Oct. 1972, pp. 1787-1806.

39. Carroll, G.W., 'Experimental and Theoretical Investigation of Three-Dimensional Turbulent Mixing in Jets and Ducts', Ph.D Thesis, Imperial College of Science and Technology, Mech. Eng. Dept., London, England, November 1980.

40. Mahgoub, H.E.H. and Bradshaw, P., 'Calculation of Turbulent-Inviscid Flow Interactions with Large Normal Pressure Gradients', AIAA Journal, October 1979, pp. 1025-1029.

41. Chen, Z.B. and Bradshaw, P., 'Calculation of Viscous Transonic Flow over Airfoils', AIAA J., February 1984, pp. 201-205 (also, AIAA Paper 82-0997, June 1982).

NASA National Aeronautics and Space Administration

Report Documentation Page

1. Report No.	2. Government Accession No.	3. Recipient's Catalog No.
NASA CR-4139		

4. Title and Subtitle	5. Report Date
Fully-Coupled Analysis of Jet Mixing Problems — Three-Dimensional PNS Model, SCIP3D	April 1988
	6. Performing Organization Code

7. Author(s)	8. Performing Organization Report No.
D. E. Wolf, N. Sinha, and S. M. Dash	SAIC/PR TR-67
	10. Work Unit No. 505-62-71-01
9. Performing Organization Name and Address Science Applications International Corporation Propulsion Gas Dynamics Division Research Park, 202 Wall Street Princeton, NJ 08540	11. Contract or Grant No. NAS1-16535
	13. Type of Report and Period Covered Contractor Report
12. Sponsoring Agency Name and Address NASA Langley Research Center Hampton, VA 23665-5225	14. Sponsoring Agency Code

15. Supplementary Notes

Langley Technical Monitor: Richard G. Wilmoth

Final Report

16. Abstract

This final technical report describes numerical procedures formulated for the analysis of three-dimensional (3D) jet mixing problems, as incorporated in the computer model, SCIP3D. The overall methodology closely parallels that developed in the earlier 2D/axisymmetric jet mixing model, SCIPVIS. SCIP3D integrates the 3D parabolized Navier-Stokes (PNS) jet mixing equations, cast in mapped cartesian or cylindrical coordinates, employing the explicit MacCormack Algorithm. A pressure-split variant of this algorithm is employed in subsonic regions with a sublayer approximation utilized for treating the streamwise pressure component. SCIP3D contains both the ks and kW turbulence models, and employs a two-component mixture approach to treat jet exhausts of arbitrary composition. Specialized grid procedures are used to adjust the grid growth in accordance with the growth of the jet, including a hybrid cartesian/cylindrical grid procedure for rectangular jets which moves the hybrid coordinate origin towards the flow origin as the jet transitions from a rectangular to circular shape. Numerous calculations are presented for rectangular mixing problems, as well as for a variety of basic unit problems exhibiting overall capabilities of SCIP3D.

17. Key Words (Suggested by Author(s))	18. Distribution Statement
Propulsion Integration Jet Plume Jet Mixing	Unclassified - Unlimited Subject Category 02

19. Security Classif. (of this report)	20. Security Classif. (of this page)	21. No. of pages	22. Price
Unclassified	Unclassified	144	A07

NASA FORM 1626 OCT 86

NASA-Langley, 1988

For sale by the National Technical Information Service, Springfield, Virginia 22161-2171